KU LEUVEN

FACULTEIT BIO-INGENIEURSWETENSCHAPPEN

Atomic Force Microscopy: a tool to study zeolite growth and transformation

Studie van zeolietgroei en -transformatie door middel van Atomic Force Microscopy

Promotoren:
Prof. Christine Kirschhock
Prof. Francis Taulelle
Departement Microbiële en Moleculaire Systemen
Centrum voor Oppervlaktechemie en Katalyse

Masterproef voorgedragen
tot het behalen van het diploma van
Master of science in de bio-ingenieurswetenschappen:
katalytische technologie

Maarten Houlleberghs

juni 2016

KU LEUVEN

FACULTEIT BIO-INGENIEURSWETENSCHAPPEN

Atomic Force Microscopy: a tool to study zeolite growth and transformation

Studie van zeolietgroei en -transformatie door middel van Atomic Force Microscopy

Promotoren:
Prof. Christine Kirschhock
Prof. Francis Taulelle
Departement Microbiële en Moleculaire Systemen
Centrum voor Oppervlaktechemie en Katalyse

Masterproef voorgedragen
tot het behalen van het diploma van
Master of science in de bio-ingenieurswetenschappen:
katalytische technologie

Maarten Houlleberghs

juni 2016

Preface

First and foremost, I would like to thank Prof. Christine Kirschhock and Prof. Mike Anderson for providing me with the necessary support and the unique opportunity of investigating zeolite growth with AFM at the Centre for Nanoporous Materials (CNM) of the University of Manchester. My gratitude also goes to Dr Martin Attfield, who gave me essential directions on how to proceed with my work. Ik zou ook alle medewerkers van het 'Centrum voor Oppervlaktechemie en Katalyse' willen bedanken die mij geholpen hebben bij het tot stand brengen van deze thesis en dan vooral Michiel, Elke, Loes en Rita. In het bijzonder wil ik ook mijn dagelijkse begeleidster Sara Lieben ontzettend bedanken voor alles wat ze voor mij gedaan heeft. Bij haar kon ik altijd terecht voor raad en verbeteringen en geen enkele vraag bleef onbeantwoord. Zonder jou had deze thesis er ongetwijfeld anders uitgezien Sara. Bedankt! I would also like to extend my gratitude to Sree, who took numerous SEM images of the materials used in this work and without whom the long nights in the lab during Easter break would have been a lot lonelier. Tot slot wil ik ook nog Prof. Steven de Feyter en Hans Van Gorp van het Molecular Imaging and Photonics department van de KU Leuven bedanken voor de kans om enkele stalen te analyseren met hun AFM-apparatuur. Bedankt allemaal!

Je voudrais aussi remercier Prof. Francis Taulelle, qui m'a aidé à mieux comprendre la croissance des zéolithes et qui m'a introduit au monde de la RMN et au sujet de la solubilité des zéolithes. Je tiens aussi a témoigner ma reconnaissance à Dr Mohamed Haouas pour m'envoyer des échantillons de MER et pour toute l'aide qu'il m'apporté pendant mon court séjour au groupe de recherche RMN Tectospin. Grâce à lui, l'analyse des résultaux RMN ont été accompli à temps. Merci beaucoup!

I would also like to thank Vaiva, Adam, Sarah, Mélodie, Matthieu, Shiu, Farida, Matthew, Lewis, Martyn, Stephen, Wisit, Raghidah, Andinet, Mark, Natasha, Flávia and Eduardo for making me feel at home in Manchester and more importantly in 'office 2.057'. All our adventures are forever engraved in my memory. My stay in Manchester would never have been the same without you guys. You are awesome! Special thanks go to my daily supervisors Adam, Farida and Raghidah, who taught me how to use AFM and interpret the data and who I could always turn to with all my questions. Thank you!

Verder wil ik ook nog mijn ouders bedanken, zowel voor hun financiële als morele steun. Zonder jullie zou ik nooit de mogelijkheid gehad hebben om een tweede opleiding aan te vatten en zou ik niet de persoon zijn die ik nu ben. Bedankt paps en mams. Tenslotte wil ik ook mijn vriendin Janne bedanken, de liefde van mijn leven met wie ik al 9 jaar lief en leed deel. Zij sloeg er steeds in om mij op te peppen en mij aan het lachten te brengen, zelfs wanneer MS Word voor de 6de keer crashte op 3 minuten tijd en wanneer ik het “écht niet meer zag zitten”. Obrigado meu bem, eu te amo!

Table of Contents

Part II: Materials and methods

Part III: Results and Discussion

Abstract

Zeolites represent a substantial part of the detergent and catalyst markets. In 2015, global zeolite production was estimated at 1 850 kilotons and future projections even indicate a progressive rise in demand. Despite their extensive use, little is known about the actual growth of these highly porous, crystalline solids. In this work, the surface of several zeolite structures (MER, UTL, -COK-14 and IWW) was investigated with **'contact-mode' atomic force microscopy (AFM)**. Identification and quantification of distinct features on the crystal surface allowed to formulate a growth mechanism hypothesis. For **MER** synthesis at 90 °C, growth was observed to occur through a **'birth and spread'** growth mechanism. Synthesis of MER from the same mixture but at 170 °C however, yielded crystalline particles which developed by **'spiral growth'** and demonstrated an average terrace step height of 0.6 ± 0.1 nm. Variations in supersaturation were qualitatively determined by means of liquid state NMR of the supernatant solution after 2, 4, 8, 16, 32 and 48 hours of synthesis at different temperatures (90, 150 and 175 °C) and indicated an increase in supersaturation conditions with decreasing temperature. As-synthesized (AS) **UTL** was also observed to develop through **'birth and spread'** growth, with terrace step heights averaging at 1.5 ± 0.1 nm. Transformation of UTL to -COK-14 resulted in an average step height decrease of 0.30 nm. AFM characterization of **IWW** crystals revealed a very rough, layered surface covered with spherical 'lumps', which is indicative of an **'adhesive type'** growth mechanism. Detailed insight in these prevailing growth mechanisms and the synthesis conditions which govern their occurrence is essential to allow the tailor-made synthesis of zeolites with specific crystal size, morphology and improved functionality. In addition, mechanical post-treatment was carried out on AS UTL and -COK-14 in an attempt to increase the available surface area. Ball milling and manual treatment with a pestle were performed on AS UTL and succeeded in reducing the average particle size with limited loss of crystallinity. Moreover, the occurrence of holes and delamination of the layered structure further increased the available surface area of the treated crystals. Ball milling of -COK-14 with ZrO_2 grinding balls of different sizes (2 and 5 mm) indicated the combination of short milling times (1 hour) and smaller grinding balls (2 mm) favored the formation of larger particles with respect to longer treatments (24 hours) and larger milling balls (5 mm).

Samenvatting

Zeolieten maken een aanzienlijk deel uit van de detergenten- en katalysatorenmarkt. In 2015 werd de globale zeolietproductie geschat op 1 850 kiloton en verwacht wordt dat de vraag zal blijven toenemen in de toekomst. Ondanks hun veelzijdig gebruik, is slechts weinig bekend over de eigenlijke groeimechanismen van deze poreuze, kristallijne vaste stoffen. In dit onderzoek werd het oppervlak van verschillende zeolietstructuren (MER, UTL, -COK-14 en IWW) nader onderzocht door middel van '**contact-mode' atoomkrachtmicroscopie (AFM)**. Aan de hand van typerende structuren op het kristaloppervlak kan een hypothese opgesteld worden betreffende de groei van de kristallijne fase. De groei van **MER** bij 90 °C verliep via een **'genese en proliferatie'** groeimechanisme. MER synthese vanuit eenzelfde precursormengsel maar bij een andere temperatuur, resulteerde in kristallijne partikels die gevormd werden door **'spiraalgroei'**. De gemiddelde hoogte van de trap-structuren op het oppervlak bedroeg 0.6 ± 0.1 nm. Variaties in supersaturatie werden kwalitatief bepaald door NMR-analyse van de vloeistoffase uit te voeren op het supernatant dat bekomen werd na synthese gedurende 2, 4, 6, 8, 16, 32 en 48 uur bij verschillende temperaturen (90, 150, 175 °C). Uit deze resultaten werd geconcludeerd dat supersaturatie toeneemt bij een dalende temperatuur. De ontwikkeling van **UTL** verliep ook door middel van '**genese en proliferatie'** groei, waarbij terras-achtige oppervlaktestructuren gevormd werden met een gemiddelde hoogte van 1.5 ± 0.1 nm. Transformatie van UTL naar -COK-14 ging gepaard met een 0.3 nm afname van deze hoogte. AFM karakterisering van **IWW** kristallen wees op een uiterst ruw, gelaagd oppervlak met talrijke sferische 'knobbels'. Deze oppervlaktestructuren zijn kenmerkend voor een **'adhesie-type'** groeimechanisme. Inzicht in zowel het groeimechanisme als de synthesecondities die dit mechanisme teweegbrengen, is essentieel om de synthese van zeolieten met een specifieke grootte, morfologie en functionaliteit mogelijk te maken. Enkele stalen werden daarnaast onderworpen aan een mechanische behandeling met als doel het beschikbare oppervlak te vergroten. UTL werd in een eerste experiment met behulp van kogels vermaald en in een tweede manueel behandeld met een vijzel. Deze procedures resulteerden beiden in een afname van de kristalgrootte met slechts een beperkt verlies aan kristalliniteit. Het ontstaan van gaten in het oppervlak en delaminering van de behandelde stalen zorgden voor een verdere toename van het beschikbare oppervlak. Door het malen van -COK-14 met zirconia kogels van verschillende grootte (2 en 5 mm), werd vastgesteld dat een kortere behandeling (1 uur) met kleinere kogels (2 mm) resulteert in de vorming van grotere partikels dan wanneer grotere kogels (5 mm) en langere behandelingen (24 uur) aangewend worden.

List of figures and tables

List of abbreviations and symbols

8-, 10-, 12-, 14MR	Pore windows consisting of 8, 10, 12 and 14 T-atoms
AFM	Atomic Force Microscopy
AS	As-synthesized
BM	Ball milled
CHA	Framework structure of chabazite
Cm-AFM	Contact-mode Atomic Force Microscopy
COK	Centre for Surface Chemistry and Catalysis
-COK-14	Zeolite with interrupted OKO framework structure
d_{hkl}	Spacing between diffracting (hkl) planes
D4R, D6R and D8R	Secondary building units composed of two rings of 4, 6 and 8 tetrahedrally coordinated atoms
HSIL	Hydrated silicate ionic liquid
IWW	Framework structure of ITQ-22
MER	Framework structure of merlinoite
MT	Manually treated
Nc-AFM	Non-contact mode Atomic Force Microscopy
S4R	Secondary building unit composed of a single ring of 4 T-atoms
SBU	Secondary building unit
SDA	Structure directing agent
SEM	Scanning electron microscopy
UTL	Framework structure of ITQ-15 and IM-12
XRD	X-ray diffraction

Context and objectives of the research

Ever since their first synthesis in the mid-twentieth century, zeolites have had a great impact on the development and evolution of industrial practices and processes. In the refining industry for instance, the use of zeolites as catalysts has resulted in a 30% increase in gasoline yield, rendering the petroleum feedstock utilization more efficient.[1] The introduction of zeolites as heterogeneous catalysts or supports also propelled the chemical industry towards the (re)design of chemical processes resulting in a more economical synthesis of chemicals. In addition, zeolites are extensively used as desiccants and adsorbents as well as in more day-to-day products such as detergents. Improvement and development of zeolitic materials are essential in order to continue progress and innovation in their numerous application areas. More important is tailoring them to the various applications they are used for. One way to take on this task is by investigating the characteristic surface features. The (outer) surface does not only play an important role in the reactivity of zeolites, a more detailed investigation of its properties can also reveal information about the way crystals grow and how this process is terminated. An important tool for studying these surface features is *Atomic Force Microscopy* (AFM). AFM analysis yields images in the nm to µm range with clearly observable surface characteristics. The objective of this work focuses on the use of AFM to characterize the surface features of several zeolite structures (MER, UTL, -COK-14 and IWW). Based on the measured step heights, a hypothesis about the corresponding crystal growth mechanism is formulated. Understanding the growth process will enable the identification of those steps that control the emergence of crystal lattice defects during synthesis. This will in turn allow the formulation of precautionary measures and modifications to the synthesis conditions to ultimately obtain a material with specific crystal size, morphology and improved functionality. In addition, UTL and -COK-14 samples were subjected to mechanical post-treatment procedures in an attempt to increase the available surface area. The surface characteristics of the treated samples were also imaged by AFM. This research project has resulted from a collaboration between the Centre for Surface Chemistry and Catalysis (COK) of the KU Leuven, the Centre for Nanoporous Materials (CNM) of the University of Manchester, the Molecular Imaging and Photonics department of the KU Leuven and the TectoSpin NMR research group of the Institut Lavoisier de Versailles.

Part I:

Literature review

Chapter 1: Zeolites

1.1 Introduction

The term zeolite was first introduced by Swedish mineralogist Axel F. Cronstedt who observed steam being released from the natural mineral stilbite upon rapidly heating it, causing the evaporation of adsorbed water molecules. From the Greek words ζέω (*zéō*), meaning 'to boil' and λίθος (*líthos*), meaning 'stone', the term *zeolite* was born.[2] In the strict sense, zeolites are highly porous crystalline inorganic solids based on silica and alumina corner-sharing tetrahedra ($[SiO_4]$ and $[AlO_4]^-$), with silicon (Si) and aluminum (Al) as central T-atoms. The tetrahedrally coordinated T-atoms can also be replaced by heteroatoms such as phosphorus (P), boron (B) and germanium (Ge). Even though these materials do not meet the strict definition of a zeolite, they are still considered *zeolitic materials*.[3] Ultimately, the linkage of these tetrahedra results in the formation of a three dimensional framework structure with a porous network of channels and/or cages up to 15 *Å* in diameter which is sufficiently large to contain exchangeable extra-framework charge balancing cations and solvent molecules like water. Each of these unique frameworks is assigned a three-letter code by the Structure Commission of the International Zeolite Association (IZA).[4]

A pure silicate framework, with only $[SiO_4]$ tetrahedra, bears no charge in the absence of defects. The incorporation of aluminum as T-atom (Al^{3+}) introduces one negative charge into the framework that has to be compensated for by a cation. Similarly, incorporation of magnesium (Mg^{2+}) as T-atom introduces two negative charges. This mechanism of introducing charges into a zeolitic framework by replacement of T-atoms is known as *isomorphous substitution*.[5] It can be effectuated both during synthesis and afterwards. As the charge balancing cations can be exchanged for other positively charged species, this mechanism gives rise to the ion exchange features associated with zeolites.[5]

Owing to their unique structural and sieve-like characteristics, related to the network of channels described above, zeolites are among the most widely used adsorbents, ion exchange materials (detergents) and catalysts in the world. Moreover, (natural) zeolites have been used in the building industry, agriculture, soil remediation and for energy applications.[6],[7],[8] An overview of the global zeolite market by application and its future projections are provided in figure 1.[9]

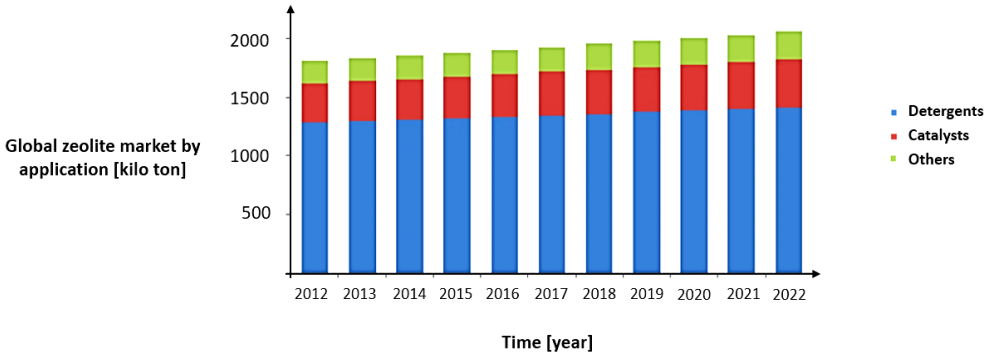

Figure 1. *Global zeolite market by application, 2012-2022 (in kilo tons).*[9]

As can be observed in figure 1, the use of zeolites as detergents or ion exchange materials accounts for 70% of the global zeolite market.[10] NaA, LTA-type zeolites with sodium ions (Na^+) as charge balancing cations, are extensively used as domestic water softeners. Na^+ is hereby preferably exchanged by polyvalent metal cations present in water such as calcium (Ca^{2+}) and magnesium (Mg^{2+}) cations. This reduces the water hardness and can ultimately produce demineralized water.[11] In their acid form, with protons as charge balancing cations, zeolites are probably the most important heterogeneous acid catalysts. Moreover, they constitute a relatively cheap and convenient way of providing atomic H for a manifold of industrial applications.[3] The presence of well-defined pore structures with specific dimensions also allows for shape selective conversions. This selectivity is threefold: only those reagents that can diffuse into the pores will enter the framework, forming only those intermediates with appropriate shape and dimensions, ultimately resulting in the formation of only those reaction products that can diffuse out of the porous structure.[3] Ever since 1983 for instance, ZSM-5 zeolite (MFI framework, Figure 2)[12],[13] has been used as catalyst for the conversion of petroleum heavy gas oil to more valuable paraffins, olefins and naphtenes. This process is known as Fluid Catalytic Cracking (FCC) and relies on this shape selectivity phenomenon.[14]

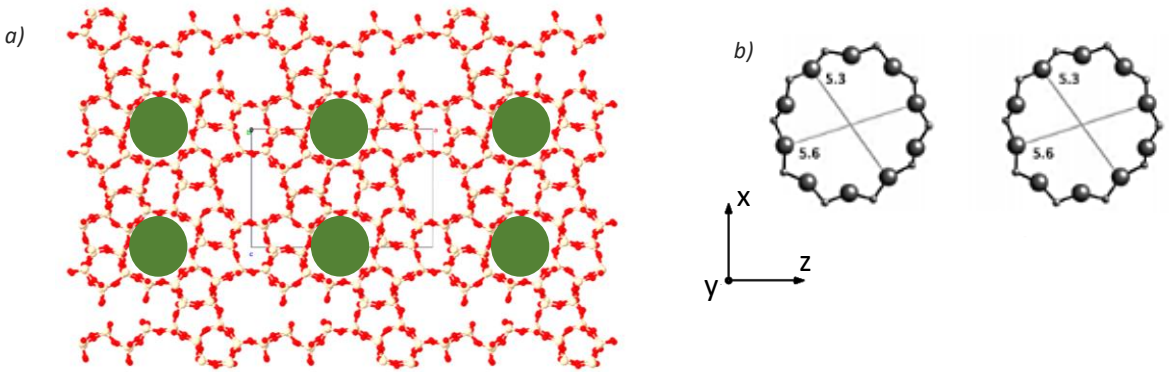

Figure 2. *a) Representation of MFI framework viewed along the [010] face.*[12] *The oxygen (O) atoms are represented in red, the tetrahedrally coordinated Al- and Si-atoms in white. The 10 membered ring (10MR) pore entrance, with 10 tetrahedrally coordinated T-atoms, is highlighted with green spheres. b) Enlarged view of 10MR pore-window along the [010] face with corresponding dimensions in Å. The [010] face is situated along the y-axis, in the xz-plane.*[13]

1.2 Framework building units

As already explained, zeolites are comprised of primary tetrahedral building units (TO_4), where the central T-atom can be either Si or Al or another heteroatom such as Ge, surrounded by four oxygen (O) atoms (Figure 3). For aluminosilicates, which only contain Si and Al as T-atoms, linkage of the tetrahedra obeys Löwenstein's rule. This rule dictates that no Al-O-Al linkages can occur. Consequently, the Si/Al-ratio of zeolites will always be larger or equal to unity. The resulting three-dimensional structures of zeolites are also referred to as topologies or frameworks, like the MFI framework of zeolite ZSM-5 presented in figure 2. Each framework is unique, but multiple zeolites can have the same framework. The main difference between these zeolites is the particular chemical composition of the framework.[3]

The interconnected 3D frameworks can further be described in terms of secondary building units (*SBUs*), which are specific arrangements of linked primary building units that are observed in several structures. The number of possible tetrahedral arrangements is almost infinite, resulting in an equally infinite number of possible *SBUs*. The most common *SBUs* are displayed in figure 4.[4] Figure 5 shows an example of the use of *SBUs* to describe the framework structure of the FAU topology.[12]

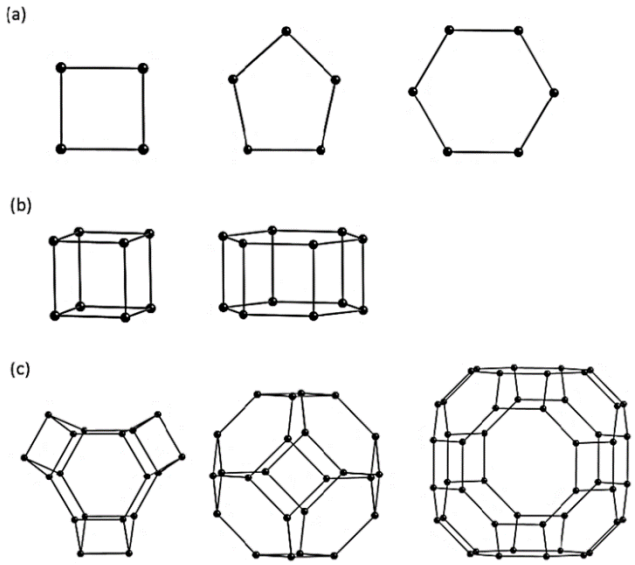

Figure 4. *Illustration of SBUs where the dots represent the T-atoms; the oxygens are located in the middle of the lines joining each T-atom, but were omitted for clarity. a) SBUs with rings of different number of tetrahedrally coordinated atoms (from left to right: 4MR, 5MR and 6MR). b) Left: double 4-membered ring (D4R), with two rings of 4 tetrahedrally coordinated atoms, and right: double 6-membered ring (D6R). c) Polyhedra. Left to right: cancrinite cage, sodalite cage and α-cage.*[4]

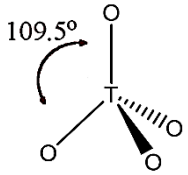

Figure 3. *Schematic representation of the tetrahedral primary building unit. Atoms labeled with 'O' are oxygen atoms in this case and 'T' the central T-atom (Si, Al, Ge, …). The bond angle between the different constituents amounts to 109.5°.*

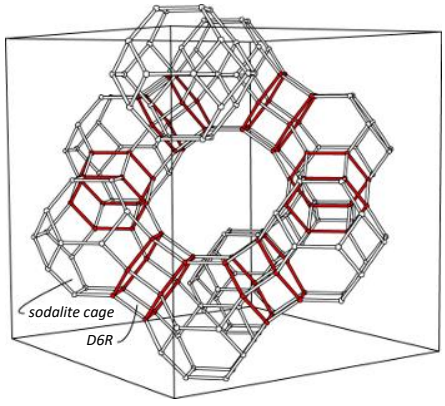

Figure 5. *Unit cell of FAU framework. The entire framework can be described with only D6Rs and sodalite cages.*[12]

Figure 5 also depicts the smallest possible building unit whose repetition in space produces the FAU framework. This particular building unit is called the *unit cell*. As can be observed, the entire framework can be described in terms of interconnected D6Rs and sodalite cages. The same reasoning can be applied to other topologies, although the amount of *SBUs* can be larger and their shape more intricate.

1.3 Synthesis

Natural zeolites are formed when volcanic rocks and ash layers crystallize upon contact and subsequent reaction with alkaline/saline waters.[15] Synthetic zeolites on the other hand are conventionally prepared via a hydrothermal synthesis method. For aluminosilicates for instance, Si- and Al-sources are mixed under high temperature and pressure in the presence of an aqueous, basic medium with or without (an)organic template molecules. Si-sources include tetraethyl-orthosilicate (TEOS) or sodium silicate ($NaSiO_3$), whereas the Al-sources vary from aluminum hydroxide ($Al(OH)_3$) to aluminum ethoxide ($Al(OCH_2CH_3)_3$). The aforementioned template molecules are also termed Structure Directing Agents (SDAs), as they ultimately direct the synthesis towards the formation of a specific zeolite with corresponding topology. Other important parameters which influence the properties of the final zeolitic material are the composition of the reaction mixture, pH, temperature, pressure and time scale of the synthesis procedure.[2]

An alternative route to hydrothermal synthesis was developed in 2004 by E. R. Cooper *et al.* (2004) and was termed ionothermal synthesis.[16] This new synthesis methodology is based on non-aqueous solvents such as ionic liquids which act both as solvent and SDA.[17] Ionic liquids are defined as salts in the liquid state because they consist only of cations and anions. They demonstrate high thermal stability, excellent solvating properties and very little measurable vapor pressure, increasing the overall safety of the synthesis procedure.[18] Moreover, the amount of possible cation and anion combinations is, in theory, infinite and the specific composition of ionic solutions can be tailored for each application. These unique features have resulted in a growing interest in and application of ionic liquids for zeolite synthesis. Recent successful syntheses include the formation of aluminophosphates (or AlPOs, with tetrahedrally coordinated Al and P atoms) and gallium phosphates (or GaPOs, with Ga and P corner-sharing tetrahedra). [19],[20]

Ever since the preparation of the first synthetic zeolites in the mid twentieth century by R. M. Barrer[21] and R. M. Milton[22], the progress in the field of zeolite synthesis has been impressive. New zeolites and topologies have been developed, ranging from high silicate content materials to novel zeolitic materials with heteroatoms in the tetrahedral framework structure.[23] An overview of the progress made throughout the past decades is illustrated in table 1.[23] As a result, 229 unique zeolite frameworks and more than 40 naturally occurring zeolite frameworks have been identified as of July 2015 and more and more frameworks are bound to be discovered in the future.[12],[24]

Table 1. *Evolution of zeolite structures and their composition.*[23]

Time of initial discovery	Composition
Late 1940s to early 1950s	Low Si/Al ratio zeolites
Mid-1950s to late 1960s	High Si/Al ratio zeolites
Early 1970s	SiO_2 molecular sieves
Late 1970s	$AlPO_4$ molecular sieves
Late 1970s to early 1980s	SAPO and MeAPO molecular sieves
Late 1970s	Metallo-silicates, aluminosilicates
Early to mid-1980s	$AlPO_4$-based molecular sieves
Early to mid-1990s	Metallophosphates
	Mesoporous molecular sieves
	Octahedral–tetrahedral frameworks
Late 1990s	Metal organic frameworks
2000s	UZM aluminosilicate zeolites, Si/Al = 2–30
	Germanosilicate zeolites
	SiO_2 molecular sieves in fluoride media

1.4 MER

Merlinoite, a natural aluminosilicate, was discovered in 1977 in the cracks of a kalsilite-melitite mineral deposit in Cupaello near Rieti, Italy.[25] Surprisingly, its synthetic counterpart zeolite W had already been synthesized by D.W. Breck in 1953, almost 25 years earlier! Both materials were assigned the zeolite structure code MER.[26] Over the next decades, other zeolitic materials with the same structure have been prepared such as synthetic merlinoite, cobalt (Co) substituted AlPOs and Ga substituted aluminosilicates.[13] A representation of the MER framework structure is provided in figure 6.[12] The D8R and pau *SBUs* which describe the framework are illustrated in figure 7.[13]

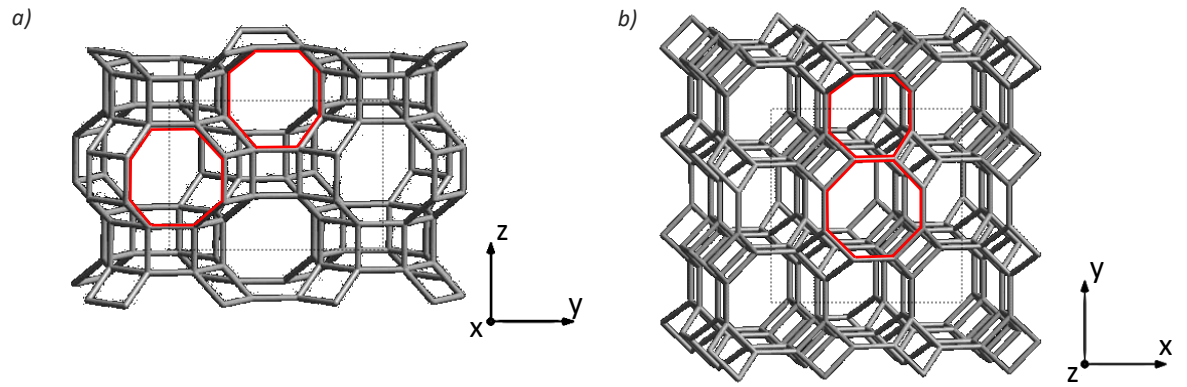

Figure 6. *Representation of MER framework structure along the a) [100] and b) [001] face.*[12] *The 8 membered ring (8MR) channels are highlighted in red. The unit cell is represented by the dotted line.*

The MER structure is characterized by unidirectional, non-interconnected 8MR channels along the three axes (Figure 6). The actual dimensions of the pore-window vary depending on their orientation. An overview of the various possible channel orientations and corresponding dimensions is illustrated in figure 8. As can be observed, the largest pores are oriented along the [001] face, with maximum dimensions of 5.1 x 3.4 Å.[13] However, zeolites with only 8MR channels are catalytically rather irrelevant because of diffusion issues and the inability to perform reactions with large, bulky molecules due to their limited pore diameters. Frameworks with 10MR and 12MR channels or ultra-large pores are far more interesting in this regard.[27]

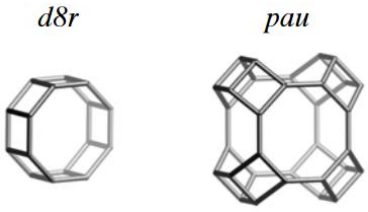

Figure 7. *SBUs of the MER framework type.*[13]

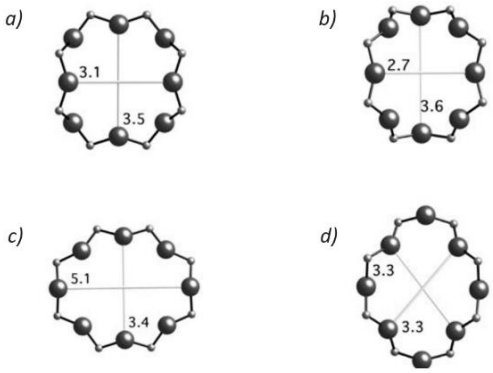

Figure 8. *8MR channel dimensions in Å along the a) [100], b) [010] and c)-d) [001] face.*[13]

Conventional preparation of zeolites with MER topology, such as synthetic merlinoite, often involve hydrothermal synthesis.[28] M. Haouas *et al.* (2014) however have reported a new procedure for the synthesis of merlinoite based on hydrated silicate ionic liquids (HSILs).[29] The proposed method consists of a two-step preparation of the silicate and aluminate precursors. Firstly, the highly concentrated silicate liquid is prepared by hydrolyzing TEOS in an alkaline, aqueous solution based on KOH. This step results in the formation of a biphasic water-ethanol system which can easily be

separated by decantation. The isolated alkaline layer contains high concentrations of the desired silicate species. A similar methodology is applied in the second step with aluminum triisopropoxide ($Al\{OCH(CH_3)_2\}_3$) or $Al(OH)_3$ as aluminum source to obtain the desired aluminate species. Upon mixing the two precursors, a homogeneous liquid is formed which crystallizes into MER crystals after heating at 170 °C for two days. Varying the water and aluminate content of the final synthesis mixture, yielded single MER crystals of different sizes. M. Haouas *et al.* (2014) concluded that higher SiO_2/Al_2O_3 molar ratios, equivalent to less aluminate in the synthesis mixture, and lower water content yield larger crystals. This conclusion is summarized in the SEM images presented in figure 9.[29]

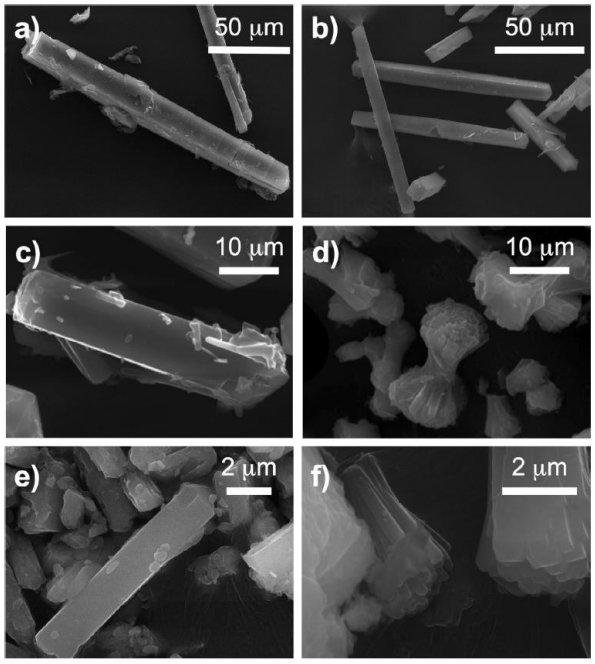

Figure 9. *SEM images of zeolite MER crystallized from the system 0.5 SiO2 : 1 KOH : x H2O : y Al2O3. a) (x,y) = (8, 0.006), b) (x,y) = (12, 0.006), c) (x,y) = (8, 0.013), d) (x,y) = (12, 0.013), e) (x,y) = (8, 0.020), f) (x,y) = (12, 0.020). Aluminum source is* $Al(OH)_3$.[29]

1.5 UTL and -COK-14

ITQ-15 and IM-12 were the first zeolites ever synthesized with the UTL framework.[27],[30] UTL zeolites are typically germanosilicates, with Si and Ge corner sharing tetrahedra as primary building units. The framework consists of two-dimensional, individual silica layers connected by D4Rs.[31] Figure 10 shows a visual representation of this particular layered framework structure along with the constituting *SBUs*.[12],[13] The bidirectional, extra-large porous network is characterized by an intersecting 14- and 12MR spherical channel system with dimensions of 8.6 x 7.6 Å and 8.2 x 5.7 Å respectively.[31]

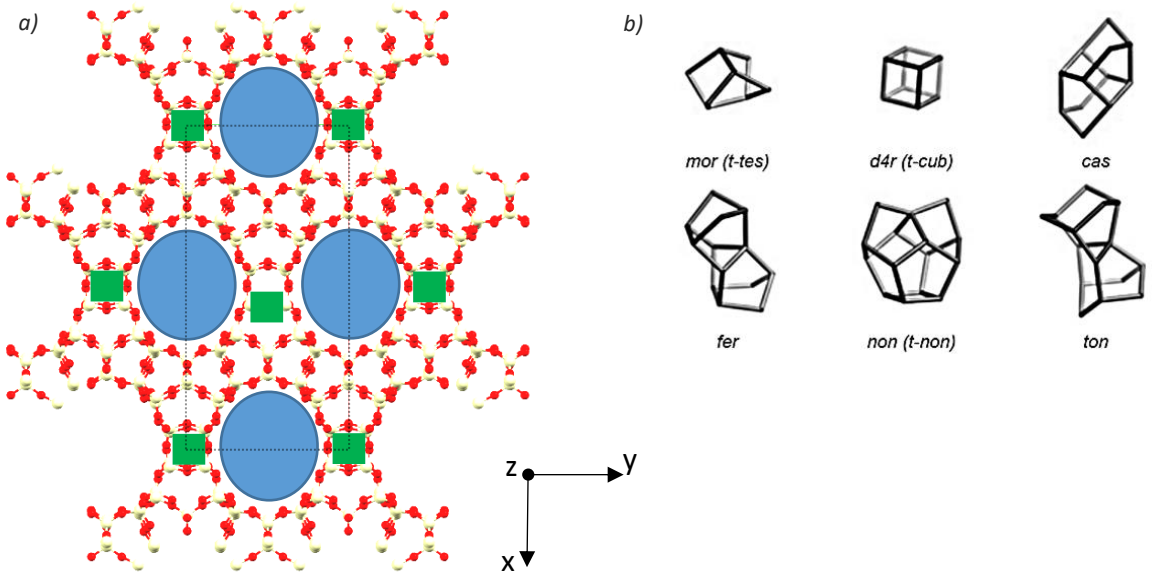

Figure 10. *a) Representation of UTL framework structure along the [001] face. The O-atoms are represented in red, the tetrahedrally coordinated Si- and Ge-atoms in white. The unit cell is represented by a dotted line. The 14MR pore-windows are highlighted with blue spheres, the connecting D4Rs with green squares. The 12MR channels run along the y-axis, intersecting the 14MR channels perpendicularly. b) Overview of SBUs describing the UTL topology.*[12],[13]

Due to its large channels and bidirectional connectivity, UTL-type zeolites are interesting from a catalytic point of view.[32] N. Kasian *et al.* (2011) successfully converted a UTL germanosilicate into a bifunctional catalyst with both Ge-OH Brønsted acid sites and active platinum (Pt) species. Such a catalyst is capable of selectively converting n-decane into its skeletal isomers and into smaller paraffins by hydroconversion, a process during which cracking and hydrogenation occur simultaneously.[33] Alternatively, the acidity and hence catalytic activity of UTL-type zeolites can be enhanced by introducing heteroatoms into the framework structure either by direct synthesis or post-synthesis modification through isomorphous substitution. The latter involves substitution of framework T-atoms by appropriate 3-valent heteroatoms such as Al, Ga and iron (Fe), or 4-valent heteroatoms like titanium (Ti) or zirconium (Zr).[32]

A key role in the formation of this layered/lamellar UTL structure, and of all germanosilicates in general, is reserved for the structure directing properties of Ge in the synthesis mixture. It has been demonstrated that Ge preferentially occupies the T-atom positions within the D4Rs.[34] For UTL in particular, it has been observed that Ge-atoms form single four-ring germanate units connecting the D4Rs to the individual silicate layers (Figure 11, p. 14).[35] In addition, Ge exhibits an exceptional coordination flexibility, with affinity for octahedral next to tetrahedral coordination.[36] This higher coordination flexibility results in a much wider range of bond angles and consequently allows the release of strain in a tetrahedrally coordinated network. Ultimately, the presence of Ge in the

framework structure effectuates the formation of zeolites with low framework density and large pore systems with high pore volumes.[37] This particular feature of Ge has led to the discovery of new zeolites with unprecedented channel systems such as ITQ-33 with interconnecting 18-, 10- and 10MR channels and ITQ-37, a zeolite with a special interrupted framework type (-ITV) and large 30MR channels.[32],[38] The three-letter code of interrupted framework structures is always preceded by a hyphen (-), in agreement with the specifications of IZA.[13]

The use of Ge in zeolitic framework structures unfortunately also has an important drawback. Because of the coordination flexibility, germanosilicates exhibit reduced stability in hydrothermal conditions and are more sensitive to moisture. This effect is more pronounced with increasing Ge-content of the zeolitic framework. Consequently, structural degradation by hydrolysis of weak germanate links in the D4Rs may occur even in the presence of ambient humidity. This instability towards moisture is however only observed for calcined samples.[37] Calcination entails the removal of organic SDAs by heat treatment, thereby emptying the pores and leaving them 'unsupported'. This stability issue poses a major obstacle in the practical use of germanosilicates.[33],[37] On the other hand it creates new possibilities as the silicate layers (named IPC-1P) can be isolated.[37] Selective hydrolysis of the weak germanate linkages and subsequent reassembly can give rise to new framework structures. This methodology was successfully applied for the first time by E. Verheyen *et al.* (2012) and was termed 'inverse sigma transformation'.[35] By treating UTL parent material (IM-12) with a 12 M hydrochloric acid (HCl) solution at 95 °C, they managed to dislodge the germanate single four-rings (Ge-S4Rs) by selectively hydrolyzing the weak germanate bond between the silicate IPC-1P layers and the D4Rs. This step resulted in a contraction of the framework by shifting the Ge-S4Rs into the channels and gave rise to an interrupted framework zeolite denoted as Ge-COK-14. Upon further washing and calcination, the Ge guest atoms were successfully removed and the individual IPC-1P layers reassembled through condensation of opposing silanol groups (Si-OH). Ultimately, this process resulted in the formation of COK-14, an almost pure-silica zeolite with OKO framework topology and a porous network comprised of intersecting 12- and 10MR channels.[35] An overview of the different steps discussed in the transition of IM-12 to COK-14 along with the corresponding framework structures is presented in figure 11.[35] The reassembly of the IPC-1P silicate layers is a reversible process. The siloxane bridges (Si-O-Si bonds) in the newly formed, interconnecting S4Rs are easily rehydrated in the presence of moisture. This rehydration process results in the formation of the interrupted framework zeolite -COK-14, in which the individual IPC-1P layers are held together by strong hydrogen bridges between opposing Si-OH groups.[35]

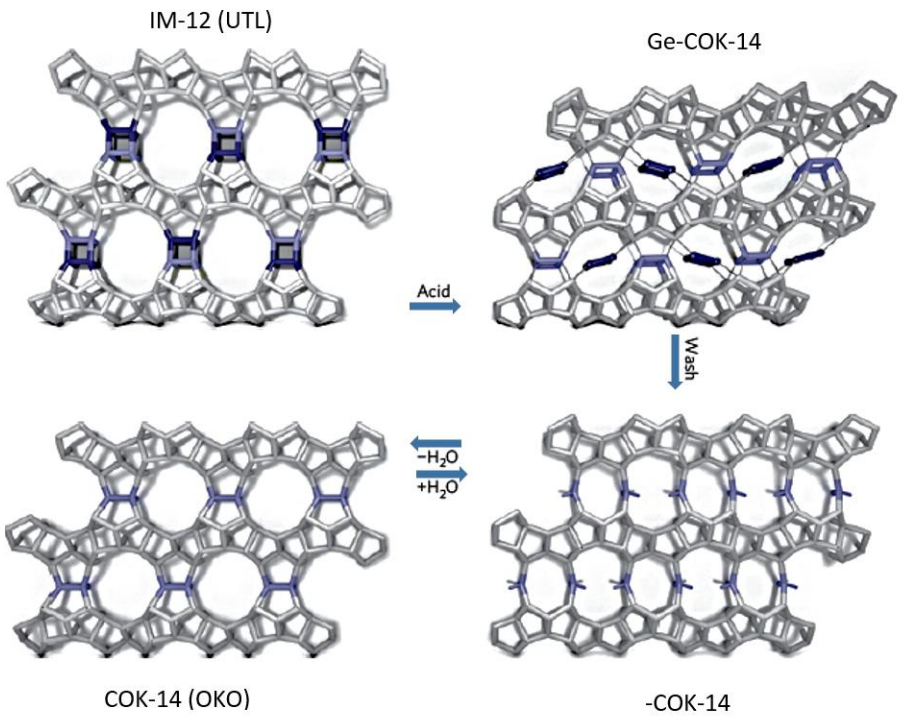

Figure 11. *Acid leaching of IM-12 zeolite dislodges Ge-S4Rs (dark blue), resulting in a framework contraction whereby the Ge-S4Rs are shifted into the channels of Ge-COK-14. Subsequent washing eliminates the Ge-atoms from the framework, resulting in the pure-silica -COK-14 with an interrupted framework, which is then calcined at 550 °C. Through condensation of opposing silanol groups accompanied by the release of water (dehydration), the indivual IPC-1P silicate layers are linked together, closing the structure and forming zeolite COK-14 with fully connected OKO framework stucture. Silicate tetrahedra in the IPC-1P layers are depicted in grey, whereas Si T-atoms in the Si-S4Rs are presented in light blue.*[35]

These findings were further substantiated by W. J. Roth *et al.* (2013) and M. Mazur *et al.* (2014).[31],[37] These researchers obtained comparable results by applying a similar procedure to a UTL starting material. This new methodology, which they termed ADOR (Assembly-Disassembly-Organization-Reassembly), makes use of different linker molecules which are intercalated between the IPC-1P layers and subsequently removed by calcination. Calcination occurs at elevated temperatures and promotes condensation between the silanol and/or amine groups, removing the remaining organic material. The use of diethoxydimethylsilane (DEDMS) as linker molecule resulted in the formation of IPC-2, a zeolite with the same framework structure as COK-14. Utilization of octylamine on the other hand, resulted in the synthesis of IPC-4, a zeolite with PCR framework structure and orthogonal 10 x 8 channel system.[31],[37] It is clear that germanosilicates, and in particular those with a unique layered structure like UTL, will play an important role in the development of zeolites with unique features and extra-large pore systems in the years to come.

1.6 IWW

A. Corma *et al.* (2003) were the first to synthesize zeolite ITQ-22, a germanosilicate with IWW framework structure.[39] The channel system consists of fully interconnected 8-, 10- and 12MR channels with dimensions amounting to 4.6 x 3.3 Å, 4.9 x 4.9 Å and 6.7 x 6.0 Å respectively.[13] A more intuitive representation of this 3D porous network is shown in figure 12, together with an overview of the IWW framework structure and its constituting *SBUs*.[12],[13],[39]

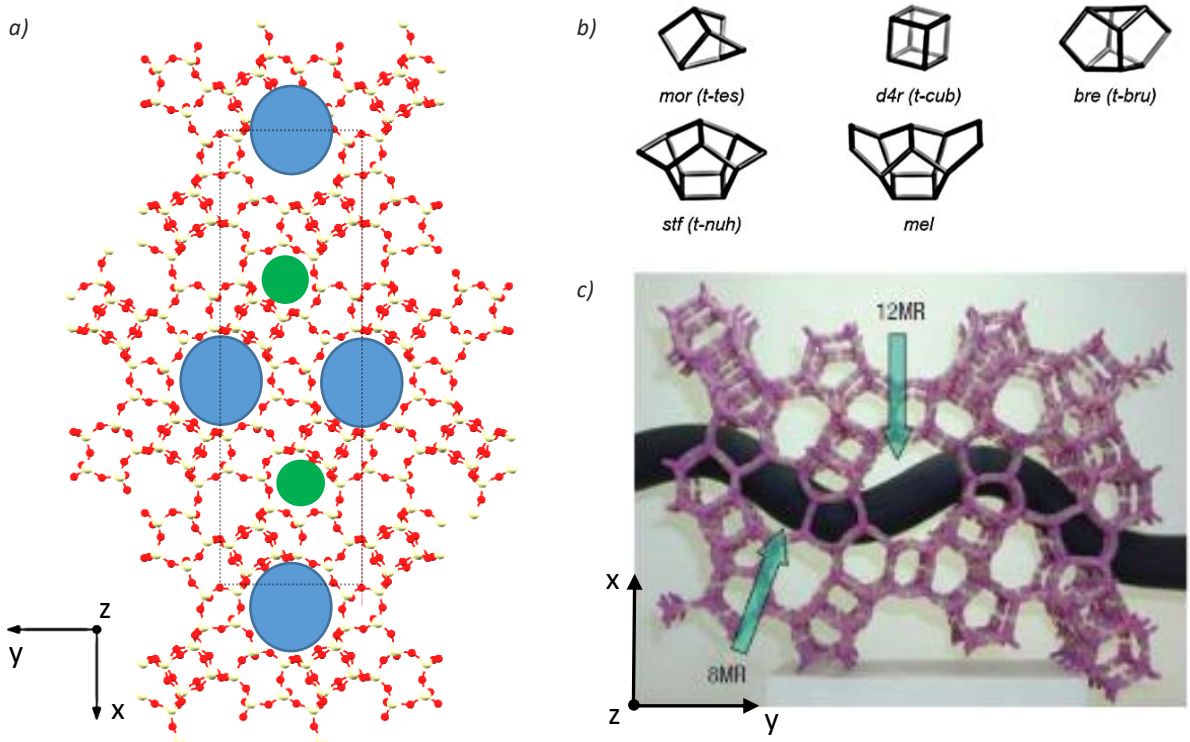

Figure 12. *a) Representation of IWW framework structure along the [001] face.*[12] *The O atoms are represented in red, the tetrahedrally coordinated Si- and Ge-atoms in white. The unit cell is represented by a dotted line. The 12MR pore-windows are highlighted with blue spheres, the 8MR pore-windows with green spheres. b) Overview of SBUs describing IWW topology.*[13] *c) 3D structure model of ITQ-22 showing the 8MR and 12MR pores that are intersected by the sinusoidal 10MR channels (black ribbon).*[39]

Being a member of the germanosilicate family, most of the considerations discussed earlier for UTL-type zeolites also apply to zeolites with IWW topology. IWW-type zeolites possess a layered framework structure similar to UTL with Ge-atoms located in the interconnecting D4Rs, which makes them suitable for inverse sigma transformation or ADOR post treatment.[40] These two framework structures mainly differ in the fact that the original IWW structure, unlike UTL, is preserved upon calcination and removal of the template. Because of this particular property, IWW-type zeolites are more stable than zeolites with UTL framework structures.[40]

P. Chlubná-Eliásová *et al.* (2014) applied the ADOR methodology to an IWW type sample and obtained remarkable results.[41] The nature of the final zeolitic material strongly depended upon the Ge-content of the D4Rs in the IWW framework. Ge-rich samples (Si/Ge = 3.6) had 6 out of 8 possible T-atom positions in the D4Rs occupied by Ge-atoms. Upon hydrolyzing these IWW samples with 12 M HCl, Ge-atoms were successfully leached out of the structure. Subsequent calcination resulted in the formation of IPC-5P, a new lamellar phase with IWW structure of the layers. Intercallation of DEDMS between the individual silicate layers and subsequent calcination gave rise to the restoration of the parent IWW-type material, demonstrating the validity of the ADOR methodology for these particular framework structures.[41]

Ge-poor samples on the other hand (Si/Ge = 6.4) contained only 4 tetrahedrally coordinated Ge-atoms in the D4Rs. Hydrolysis of Ge-poor IWW-type zeolites in similar conditions as for their Ge-rich counterparts, did not result in the same lamellar phase. Even though leaching of the Ge-species was found to be successful, there were still connections present between the layers holding the 3D framework structure together. Consequently, the final zeolitic product was identified as a strongly defective IWW-like material.[41] L. Burel *et al.* (2014) carried out a similar experiment with a Ge-poor ITQ-22 zeolite and determined that these defects gave rise to the formation of mesopores in the framework structure.[40] Further analysis revealed that the framework was enriched in Si, implying that part of the dissolved Si species were reincorporated into the framework structure. This Si-enriched ITQ-22 zeolite was denoted [Si]-ITQ-22 and exhibited superior thermal stability as opposed to its Ge-containing precursor.[40] Subsequent incorporation of Al in the framework of [Si]-ITQ-22 was achieved by both P. Chlubná-Eliásová *et al.* (2014) and L. Burel *et al.* (2014) by dispersing the Si-enriched zeolite in an HCl solution (pH 2) of aluminum sulphate or aluminum trichloride.[40],[41] This treatment yielded a zeolitic material with both micro- and mesopores and acidic sites embedded in the framework structure. These features imply unique catalytical properties, which are yet to be tested.[40] A schematic overview of the different steps and materials discussed above is displayed in figure 13.[41]

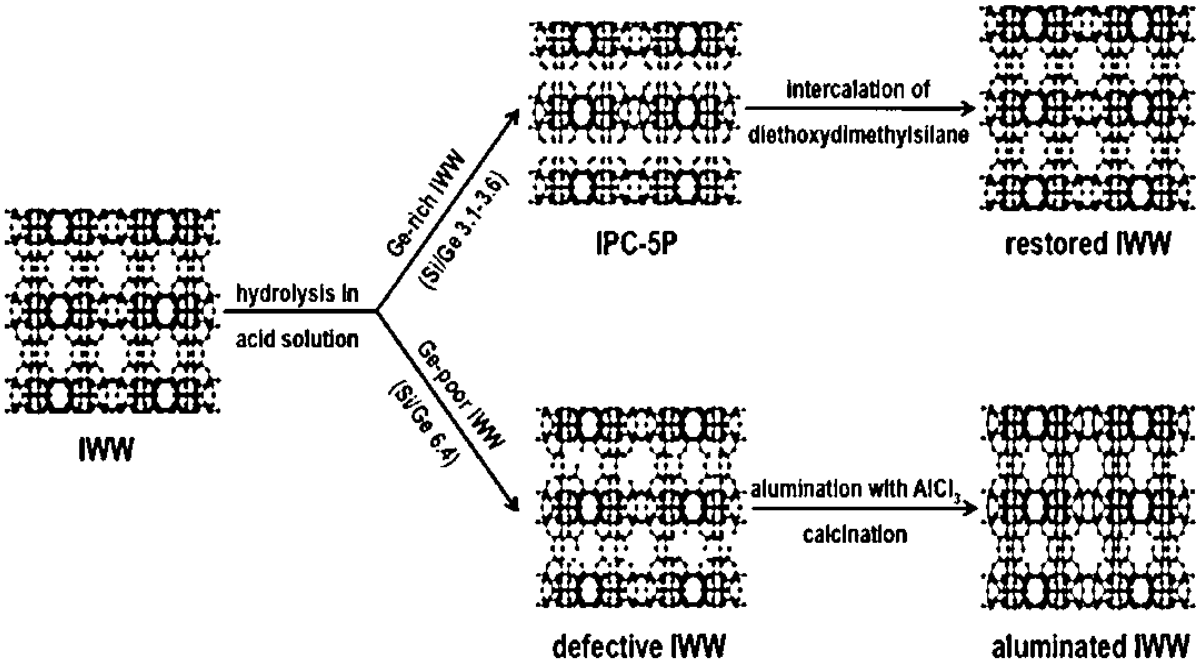

Figure 13. *Hydrolysis of IWW-type zeolite with variable Ge-content and post-synthesis treatments, resulting in either 'restored' or defective, aluminated IWW frameworks.*[41]

Chapter 2: Crystal growth

Crystal growth of solid-state materials affects all properties and functionalities which render them so interesting for industrial applications. For zeolites for example, crystal growth determines the dimensions and the connectivity of the porous network. The presence of intrinsic defects, defined as aperiodic interruptions in a periodic crystal structure, can also be attributed to phenomena occurring during crystal growth. These defective traits can strongly influence the stability of the crystal structure and potentially affect its catalytic activity. By understanding the corresponding growth mechanism, it will be possible to isolate those steps that control the emergence of these defects. This will in turn allow the formulation of precautionary measures and modifications to the synthesis conditions to ultimately obtain a material with specific size, crystal morphology and improved functionality.[42] Different crystal growth models have already been proposed in this regard and continue to be refined as more data become available.

2.1 Nucleation and growth

The first step in the formation of a new crystalline material from solution (or gel) involves the rearrangement of a small number of dissolved ions, atoms or molecules into a cluster of the crystalline product. Once this cluster has reached a critical radius, a stable nucleus is formed. This initial process is called *nucleation*. A distinction is made between primary and secondary nucleation processes. Primary nucleation occurs either heterogeneously or homogeneously. In the former, the surface of a foreign particle in solution such as a dust particle acts as the nucleation center. In the latter, nucleation is spontaneous and occurs in the absence of these particles. Secondary nucleation on the other hand is observed when the process is induced by the presence of crystals of the same material.[42]

The nucleation process is followed by a complex growth stage in which the stable crystalline nucleus grows by addition of new building units in a prearranged system. This system is determined by the framework structure of the zeolite being formed, with the unit cell as basic motif. Properties of the final zeolite crystals, such as morphology and crystal size distribution, depend on a large number of parameters. These parameters include the crystallization conditions, such as temperature and tumbling rate, as well as synthesis conditions, such as pH and composition of the synthesis mixture.[42]

The thermodynamic driving force behind both nucleation and crystal growth processes is referred to as *supersaturation*. In general, supersaturation is defined as the chemical potential difference between a molecule in solution (μ_v) and in the bulk of the growing crystal (μ_c).[42] For crystallization processes in suspensions however, this definition can also be formulated as the difference between the actual concentration *C* of a solute and the equilibrium concentration or solubility C_0 of this solute at a given temperature. The degree of supersaturation σ can subsequently be expressed by: $\sigma = \frac{C-C_0}{C_0}$. Thermodynamics dictates that the change of Gibbs free energy ΔG must be less than zero for any given process to occur spontaneously. For crystallization processes, this entails that the change of Gibbs free energy per unit volume of the solid phase, ΔG_v, must be less than zero. The degree of supersaturation σ and ΔG_v are correlated by following expression:[43]

$$\Delta G_v = \frac{-k.T}{\Omega}.\ln(1 + \sigma)$$

where k is the Boltzmann constant equal to $1.38\ x\ 10^{-23}\ \frac{J}{K}$, T the temperature in kelvin (K) and Ω the atomic volume expressed in $\frac{m^3}{atom}$.

From this equation it is easily deduced that σ must be larger than zero for ΔG_v to be negative and crystallization to occur spontaneously. Without supersaturation (i.e. σ = 0), no nucleation will take place.[43] On the other hand, the probability of nucleation in a given system increases with rising supersaturation level. The effect of supersaturation on nucleation rate and crystal size is summarized in figure 14.[42] After a brief induction period, the nucleation rate rapidly escalates as supersaturation rises, but decreases again as crystal growth is initiated. The growth rate sets off exponentially, but becomes constant as supersaturation levels off and steady state is reached. Steady state growth is characterized by a linear increase in crystal size. As the concentration of framework-forming elements is exhausted and supersaturation decreases, the growth rate drops and finally becomes zero. At this point, the zeolite crystals have reached their final size.[42] Ultimately, the process described above results in the formation of zeolite crystals with different sizes. Nucleation and growth rate will vary locally as supersaturation levels differ throughout the solution, resulting in a range of crystal sizes. Rather than referring to the absolute size of these crystals, their dimensions are expressed in terms of a *crystal size distribution*. This parameter defines the mean size of the crystallites and establishes a range which encloses the dimensions of the other zeolite crystals.[44]

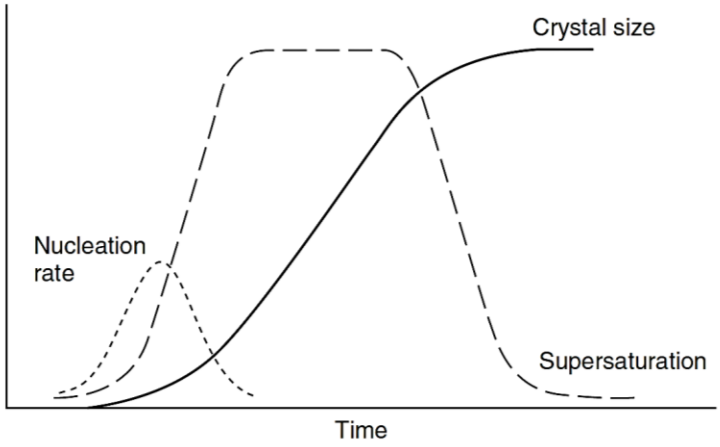

Figure 14. *Schematic representation of the zeolite synthesis process showing the evolution of nucleation, crystal size and supersaturation levels as a function of synthesis time.*[42]

It is clear that the size of zeolite crystals, a feature which influences both their efficiency as catalysts and selectivity towards specific reaction products, can be manipulated by controlling the crystallization conditions and supersaturation levels.[44] At low supersaturation, crystal growth prevails and crystals grow faster than they nucleate, resulting in the formation of larger crystals. At high supersaturation levels, nucleation dominates and crystals of smaller size are formed.[44]

2.2 Layer growth

Crystal growth models are based on specific features observed on the surface structure of crystals. Kossel (1934) has provided one of the most commonly used models, which is also referred to as the 'Terrace-Ledge-Kink' or TLK model.[45] According to this model, the surface of crystalline structures is composed of cubic growth units (ions, atoms or molecules), which form layers of monoatomic height. These layers are limited by steps or (l)edges which may contain one or more kinks and/or vacancies. The area between two steps is referred to as *terrace*. These terraces may contain single adsorbed growth units, clusters thereof and vacancies as well.[42] A schematic overview of the various possible surface features described above is displayed in figure 15 for a cubic lattice.[42]

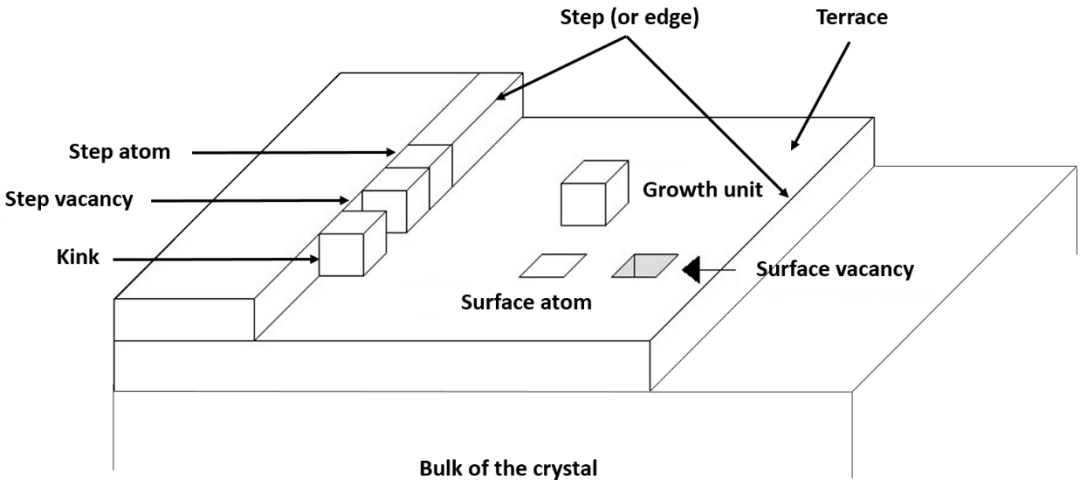

Figure 15. *Kossel model of crystal surface for a cubic lattice.*[42]

According to the method proposed by Kossel (1934), growth units adsorbed to the surface will form one bond.[45] Units which are attached to the steps will form two bonds and those attached to kink sites three bonds. Occupation of step vacancies results in the formation of four bonds, whereas five bonds are formed upon filling of surface vacancies. Lastly, six bonds are reserved for those growth units located in the bulk of the crystal. The most stable configuration, i.e. the one with the largest number of bonds formed, is offered by kink sites once all surface and step vacancies have been occupied. Consequently, crystal growth will occur by diffusion of growth units along the surface and attachment to kink sites, moving the kink along the step. By doing so, the step will advance until it ultimately reaches the edge of the crystal. A new step can then be created by nucleation of a cluster (or two-dimensional nucleus) on the crystal surface and the process is repeated.[42] This particular growth mechanism was termed **layer growth** or **single nucleation growth** and is illustrated in figures 16 and 17.[42],[46]

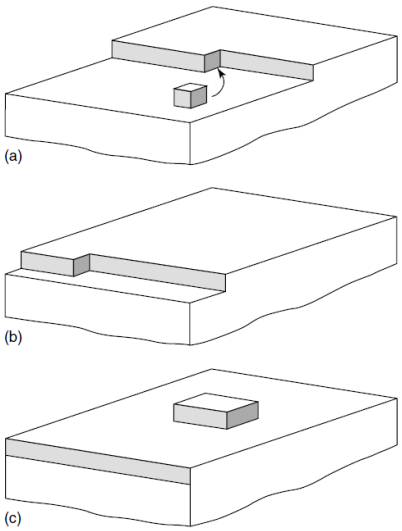

Figure 16. *Schematic representation of layer growth. (a) Attachment of growth unit to kink site, resulting in advancement of the step towards the crystal edge as illustrated in (b). (c) Formation of new two-dimensional nucleus.*[42]

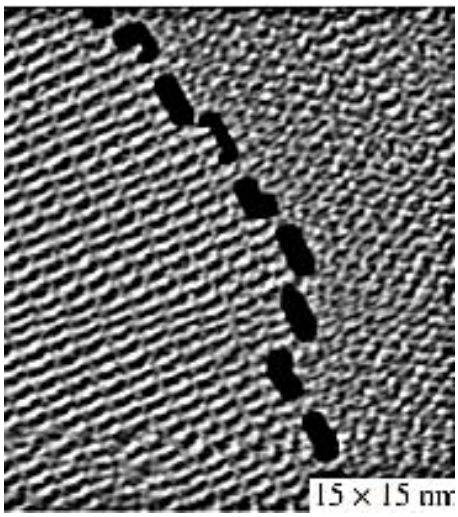

Figure 17. *In situ AFM image of a single step on the surface of the mineral calcite. The step as well as the kinks along this step are clearly visible.*[46]

When the nucleation rate is faster than the time it takes for the step to cover the entire crystal surface, a **multinucleation multilayer growth** or **'birth and spread'** mechanism is observed. This mechanism is a variation on layer growth where two-dimensional nuclei are formed all over the surface and even on top of each other. Spreading of these nuclei results in the formation of new, larger layers through coalescence of individual layers.[42] As the formation of 2D nuclei requires a lot of energy, both layer growth and 'birth and spread' mechanisms only take place at relatively high supersaturation levels.[42]

2.3 Spiral growth

At low supersaturation levels, **spiral growth** is more observed.[42] As opposed to layer growth, this mechanism does not occur through formation of 2D nuclei since the required energy barrier is too high. Instead, spiral growth is believed to initiate at screw dislocations as postulated by the Burton, Cabrera and Frank model or BCF model.[47] A screw dislocation is a line defect in the crystal that results in the formation of a step on the crystal surface (Figure 18a), hence obviating the necessity for 2D nucleation. Attachment of growth units to this step results in an upward growth of the step, normal to itself. The upward movement around the screw dislocation results in a spiral form superimposed on the crystal surface.[45] A schematic representation of the initiation and propagation of spiral growth is provided in figure 18.[42]

Growth units attach to the step induced by the screw dislocation. The attachment results in the advancement of this step and consequently generates a second step (Figure 18b). Propagation of this second step will create a third step (Figure 18c), which in turn will generate a fourth step and so on (Figure 18d). Since the step is immobile at the core of the screw dislocation, a spiral pattern is formed around the dislocation core.[42] This particular pattern is illustrated in figure 19.[48]

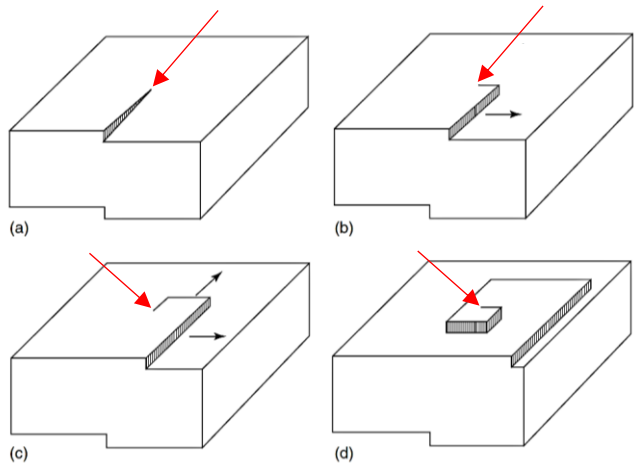

Figure 18. *Initiation and propagation of spiral growth around a screw dislocation.*[42] *The core of the screw dislocation is highlighted with a red arrow in each of the intermediate steps.*

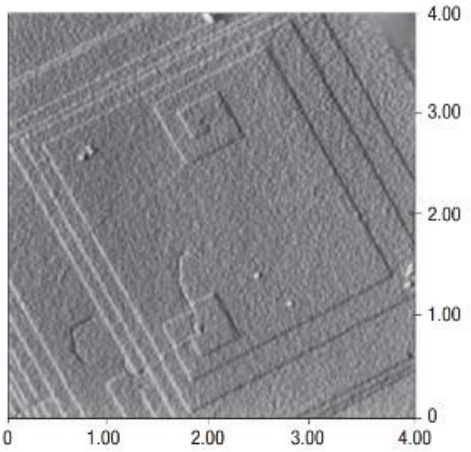

Figure 19. *AFM image of growth spirals on the [100] surface of synthetic zeolite A. The dimensions on the axes are expressed in µm.*[48]

2.4 Smooth and rough surfaces: growth mechanism and morphology

According to Sunagawa (1999), growth mechanisms can be subdivided into three types depending on the structure of the interface.[49] If the interface is rough, the predominant growth mechanism will be of the **adhesive type**. This particular growth mechanism takes place at high supersaturation levels and occurs by attachment of growth units in all possible directions, as the energetics associated with this type of crystal growth are the same regardless of the crystallographic direction. Ultimately, an adhesive-type growth mechanism gives rise to rounded surfaces covered with spherulitic, fractal and dendritic patterns.[42] On smooth interfaces on the other hand, growth will occur either by 'birth and spread' or spiral growth. The latter takes place at low supersaturation levels, as described earlier. As supersaturation levels increase and the critical concentration required for 2D nucleation is reached, the 'birth and spread' mechanism sets in and dominates growth. Both growth mechanisms finally result in the formation of a smooth crystal interface which is bound by flat surfaces with polyhedral morphologies for spiral growth and skeletal or hopper morphologies for 'birth and spread' growth.[42],[49] An overview of these growth mechanisms as a function of supersaturation is provided in figure 20.[49]

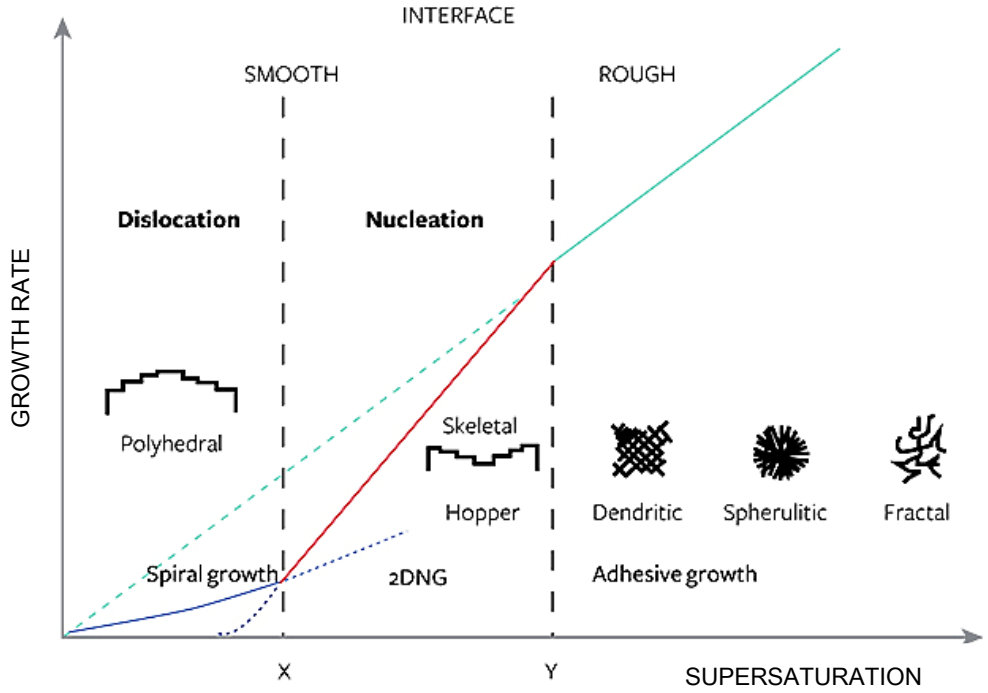

Figure 20. *Overview of crystal growth mechanisms as a function of supersaturation. Below point X (low supersaturation), spiral growth (blue curve) occurs with polyhedral morphologies covering the surface. Between points X and Y (intermediate supersaturation), two-dimensional nucleation growth (2DNG = layer and 'birth and spread' growth, red curve) takes place, resulting in skeletal or hopper surface morphologies. Beyond point Y (high supersaturation) adhesive growth (green curve) is the predominant growth mechanism, with dendritic, spherulitic and fractal patterns superimposed on the surface.*[49]

Chapter 3: Atomic Force Microscopy

Atomic Force Microscopy (AFM) is a surface-scanning technique invented by G. Binnig *et al.* in 1986 as an advancement of *Scanning Tunneling Microscope* (STM).[50] AFM and STM are both classified as *Scanning Probe Microscopy* (SPM) techniques as the two methods image surfaces using a physical probe that scans the specimen.[51] The main difference between these techniques lies in the fact that STM can only be applied to conductive samples, as it relies on the formation of a *tunneling current* between the tip of the probe and the surface of the sample in order to generate the image. AFM on the other hand monitors the effects of the interaction forces between the sharp tip and the surface of the sample to provide high-resolution images of the surface. It can therefore be applied to virtually any type of material without the need for sample treatment or vacuum.[42] The use of AFM for the study of crystalline materials has revolutionized the study of crystal growth, not only because of its high vertical resolution, but also because of its ability to scan and image surfaces which are submerged in fluids. These *in situ* AFM experiments make it possible to monitor crystal growth and dissolution/recrystallization of crystalline materials such as zeolites in real-time.[42]

3.1 Working principle

At the heart of the atomic force microscope is a sharp tip, which is mounted at the free end of a triangular or single-beam cantilever. This tip is brought into close contact with the sample. By monitoring the deflection of the cantilever in response to the interaction forces between the tip and the surface across the sample, an image of the surface is generated. Modern-day tip-cantilever systems are typically fabricated from silicon or silicon nitride. The geometry of the tip is mostly pyramidal or tetrahedral and the radius of curvature of the apex of the tip can vary from 3 nm up to 30 nm.[52] Generally, the resolution of an AFM image increases as the radius of curvature decreases and the sharpness of the tip increases.[51] Although the lateral resolution is rather low and limited by the tip radius, vertical resolution as high as 1 Å can be achieved.[42] A detailed image of a tip-cantilever system is displayed in figure 21.[53] Various types of cantilevers with distinct mechanical properties are used depending on the operating mode of the atomic force microscope.[52] The different operating modes are further discussed in section 3.2.

The tip is raster scanned across the sample (or the sample is moved under the probe) with extremely accurate positioning by mounting it on a piezoelectric scanner or *actuator*, which moves the tip (or the sample) in the x-, y- and z-direction. Piezoelectric components are materials which typically change their dimensions depending on the applied voltage.[52] As the tip moves across the sample, the cantilever is deflected as a result of interaction forces. These forces occur between the tip atoms and the atoms on the surface of the sample (Figure 22) and can be attractive or repulsive in nature, depending on the distance between these atoms.[54] At intermediate and long distances (> 1 nm) long-range Van der Waals interactions predominate. These forces are induced by temporary fluctuating dipoles and are attractive in nature, deflecting the cantilever towards the surface. As the tip gets

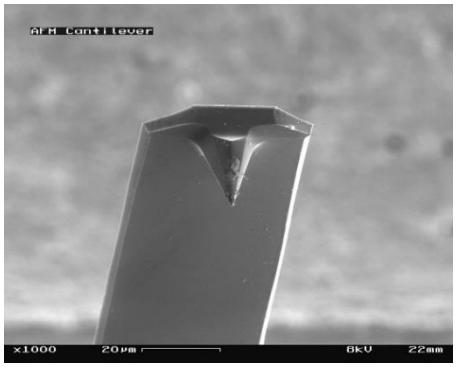

Figure 21. *SEM image of a single-beam cantilever with a sharp, pyramidal tip mounted on its free end.*[53]

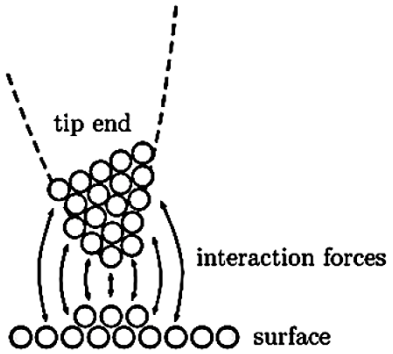

Figure 22. *Schematic representation of the interaction forces between tip and surface atoms.*[54]

gets closer to the sample, this attraction increases. At very short distances however (< 1 nm), repulsive coulombic forces become dominant and the cantilever is deflected upwards, away from the surface. These strong, short-range repulsive forces arise from the overlap of and the electrostatic repulsion between the electron clouds of tip and surface atoms and become stronger at shorter distances.[51],[54]

The deflection of the cantilever is monitored by focusing a laser beam onto the cantilever. The beam is reflected off the back of the cantilever and detected by a position-sensitive photodetector, which usually is a photodiode consisting of four sections (Figure 23).[51],[55] Initially, the reflected beam is centered at the intersection of the four quadrants of the photodetector. Upon displacement of the cantilever, the light intensity of the reflected beam is shifted and concentrated in one of the quadrants. By measuring the difference in light intensity between the upper and lower sectors, the vertical deflection of the cantilever can be determined. Analogously, the difference in light intensity between the left and right sectors of the photodetector will yield the lateral displacement of the cantilever. The output signal of the photodiode, which is proportional to the difference in light intensity, is then transmitted to a computer where the corresponding image is generated.[51]

In almost all operating modes, a feedback circuit is connected to the photodetector. The feedback system aims to keep a specific parameter constant at a pre-set value or *set point*.[51] This parameter may vary depending on the operating mode. In *constant force contact-mode* AFM for instance, a feedback loop is employed to keep the interaction force between tip and surface and hence the cantilever deflection at a fixed value as the tip scans across the sample and moves up and down following the surface morphology (Figure 23).[52],[55] This is achieved computationally by constantly comparing the output signal of the photodiode to the specified set point. If the measured deflection is different from the set point, the feedback amplifier applies a voltage to the piezoelectric scanner. The scanner then raises or lowers the cantilever relative to the sample (or the sample relative to the cantilever) in order to restore the desired value of the deflection.[56] A topographic image with calibrated height information of the sample surface is then obtained by storing the vertical control signals sent by the feedback system and converting these signals into a visual reproduction. Conversely, visual representation of the error signal, determined as the difference between set point and output signal of the photodiode, yields the corresponding deflection or amplitude images.[56] A schematic overview of a basic atomic force microscope set-up along with the imaging processes described above is presented in figure 23.[55]

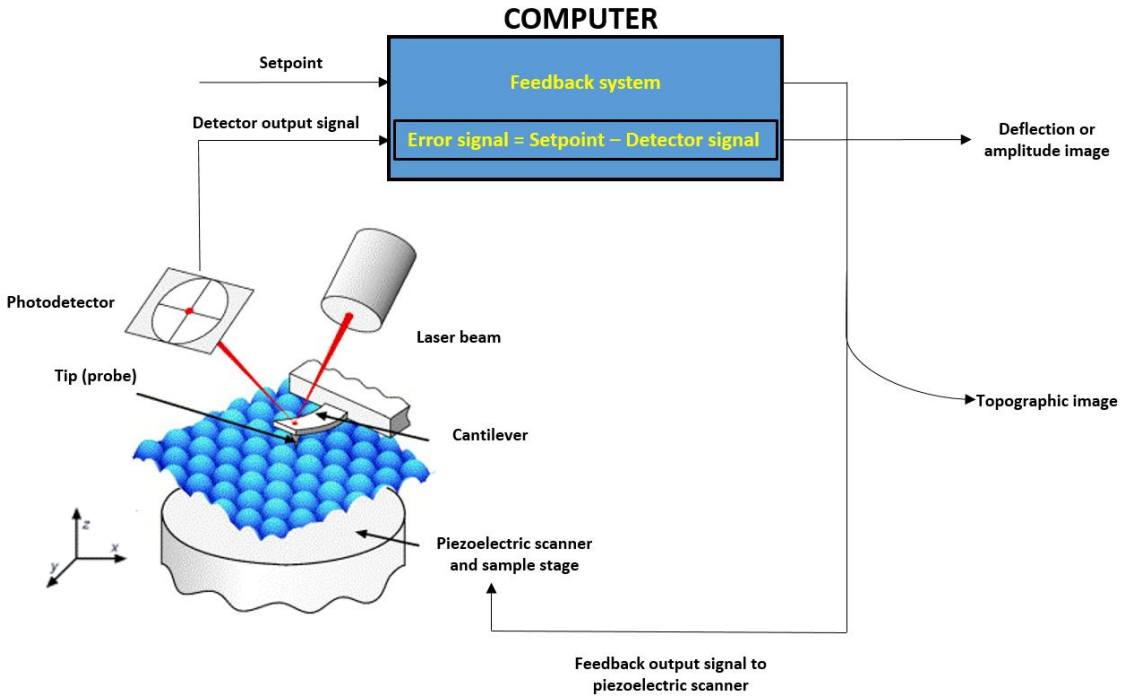

Figure 23. *Schematic overview of a basic AFM set-up. The piezoelectric scanner is incorporated in the sample stage, implying the sample will be moved relative to the tip during the scanning process. The imaging processes discussed above are also illustrated.*[55]

3.2 AFM operating modes

Two general modes of operation can be distinguished depending on whether the cantilever is kept static or oscillates while scanning the surface. The former case is usually referred to as DC mode because the static deflection of the cantilever is recorded during operation.[52] Contact-mode AFM is an example of a DC operating mode and has already been introduced earlier in section 3.1. The latter case is called dynamic or AC mode. This mode uses a feedback loop to keep the amplitude of the oscillation of the cantilever constant at a pre-set value rather than the cantilever deflection.[52] The instrumentation for AC mode AFM imaging is more complex than for its static counterpart as additional electronic components need to be integrated to induce the oscillations of the cantilever and to record the amplitude of these oscillations.[57]

Another distinction between the vast array of AFM operating modes can be made based on whether the interaction forces between tip and sample are attractive or repulsive in nature. Figure 24 provides an idealized plot of the forces acting between tip and sample surface and highlights the areas in which the main and most widely used imaging modes operate.[52] A more detailed description of these imaging modes will be provided in the following subsections.

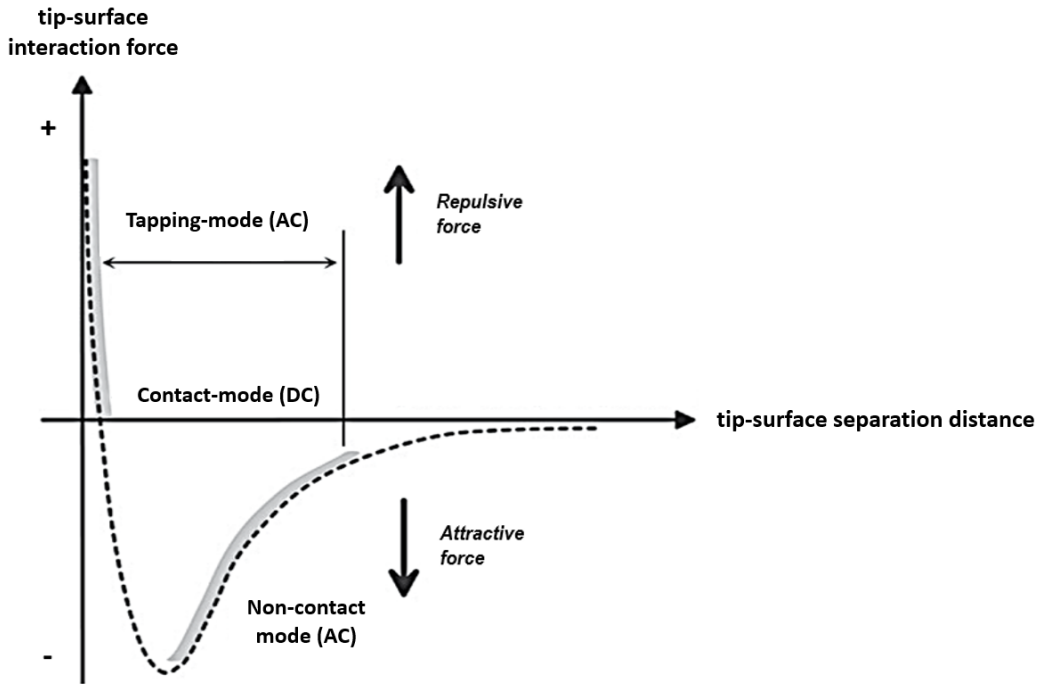

Figure 24. *Idealized plot of the interaction forces between tip and sample surface as a function of the separation distance. A positive force represents repulsion, its negative counterpart attraction. As already described in section 3.1, the attractive forces become greater with decreasing separation until a critical distance of 1 nm is reached. Further approach then results in an increasing repulsion between tip and surface. Non-contact mode (AC) AFM is conducted at lengths greater than 1 nm and only uses the attractive forces between tip and sample. Intermittent contact or tapping-mode (AC) AFM on the other hand operates around this critical separation distance and utilizes both repulsive and attractive forces. Lastly, contact-mode (DC) AFM is carried out by bringing the tip in contact with the sample. At such short distances, the predominant forces are repulsive in nature.*[52]

3.2.1 DC modes

Contact-mode (cm-AFM) is the first mode ever developed in AFM. It is also the main DC operating mode, with two distinct imaging methods: 'constant force' or 'constant height' cm- AFM.[58] The former is the most commonly used DC method where the tip is brought in mechanical contact with the sample and raster scanned over the surface (Figure 25).[52] The resulting force on the tip is repulsive at such short distances (Figure 24) and causes an upward deflection of the cantilever. A feedback system keeps the cantilever deflection and hence the tip-surface interaction force constant at a predefined set point value during scanning. 'Constant height' cm-AFM is an alternate but less common contact-mode set-up in which the cantilever is kept at a constant height above the surface during scanning. This method is used for small, high-speed atomic resolution images. The sample must be relatively flat however to prevent the tip from impinging on and damaging the surface.[58]

As mentioned earlier, the *resolution* of AFM images generally increases as the tip becomes sharper.[51] The *contrast* of contact-mode AFM images however is dependent on the cantilever deflection which is in turn proportional to the tip-surface interaction force.[52] This proportionality obeys Hooke's law or $F = -k.x$, where *F* is the force in newton (N) applied by the tip to the surface, *x* is a measure of the cantilever deflection in meter (m) and *k* the spring constant of the cantilever expressed in $\frac{N}{m}$.[51] Soft samples like biomolecules or living cells require softer cantilevers with lower spring constants. As these samples cannot tolerate large forces, a cantilever has to be used which deflects even at small forces in order to obtain sufficient contrast. In general, most cantilevers used for 'contact-mode' AFM have spring constants smaller than 0.1 $\frac{N}{m}$.[58]

One disadvantage of imaging samples in 'constant force' mode is the occurrence of strong shear forces. These lateral forces may damage the sample and originate from the fact that the tip is constantly in mechanical contact with the surface.[59] They can also provide valuable information about the (differences in) frictional properties of the surface however. By monitoring the lateral deflection of the cantilever, which results from the torsion caused by these shear forces, a relative measure of the roughness can be obtained and changes in the chemical composition of the surface can be detected. Areas of the surface with different structure or composition will influence the lateral deflection of the cantilever differently. This technique is referred to as 'Lateral Force Microscopy'.[52]

Another drawback of this particular imaging method is the presence of capillary forces that may arise in ambient conditions if the surface is covered with a thin water layer (Figure 26). Additional forces between tip and sample will considerably increase the total interaction force and possibly damage the sample as a result. This problem can easily be solved by imaging the sample in ultra-high vacuum (UHV) conditions or in a liquid environment. Immersion of both sample and cantilever will significantly reduce these capillary forces.[52]

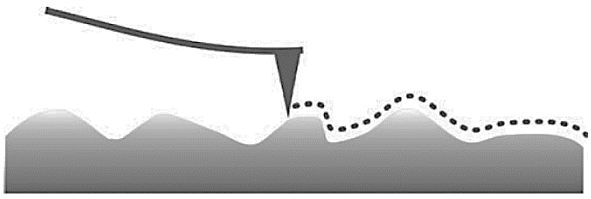

Figure 25. *'Constant force' contact-mode AFM: the tip is brought in mechanical contact with the sample and scanned across the surface, following its topography.*[52]

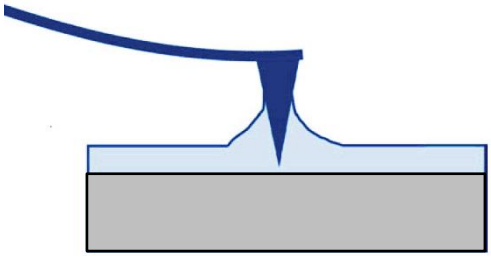

Figure 26. *Occurrence of capillary forces caused by a thin water layer adsorbed on the sample surface.*[52]

3.2.2 AC modes

As opposed to the aforementioned DC operating modes, dynamic or AC operating modes require a vertically oscillating cantilever. These cantilevers are more stiff than those used in contact-mode AFM and their spring constants typically exceed 1.0 N/m.[60] The desired oscillatory movement is commonly induced acoustically by means of a small piezoelectric crystal in the cantilever holder and its frequency approaches the resonance frequency of the cantilever. In an alternate set-up, the cantilever is oscillated by coating it with a magnetically susceptible film and exposing it to an alternating magnetic field. Interaction of the oscillating tip-cantilever system with the surface of the sample changes the frequency and the amplitude of the oscillations. These changes in oscillation form the basis of image acquisition in the two main AC operating modes: 'non-contact mode' and 'tapping-mode' AFM.[56]

In 'non-contact mode' AFM (nc-AFM), the tip-cantilever system is oscillated at 'free' resonant frequency (free of any interactions) and brought into close proximity of the sample, *without* making contact. The tip typically remains at 50 to 150 Å above the surface. At such distances, long-range, attractive Van der Waals forces predominate and pull the tip towards the surface, reducing the resonance frequency of the cantilever and its amplitude of oscillations as well.[60] Nc-AFM images are obtained by oscillating the cantilever at 'free' resonant frequency and monitoring the decrease in amplitude of these oscillations as a result of the interactions between tip and sample surface. The feedback system maintains the oscillation amplitude at a predetermined set point by moving the piezoelectric actuator and adjusting the distance between tip and sample. As the tip does not contact the sample surface, normal and lateral forces are minimized and irreversible damage to the sample is prevented.[56] The greatest disadvantage of this operating mode is that it can only be used on dry samples and ideally under UHV conditions. In ambient conditions, the presence of an adsorbed water layer on the surface will distort the image because of additional tip-surface interactions. Moreover, if the tip were to penetrate this layer during scanning, it could become 'trapped'. In nc-AFM, the amplitude of the oscillations is rather limited and hence the energy of the vibrating system is not sufficiently high to compensate for the added capillary forces acting on the tip.[52] When carried out in proper UHV conditions however, 'non-contact mode' AFM can be used to image samples with atomic resolution.[57]

As opposed to nc-AFM, 'tapping-mode' AFM is carried out by bringing the oscillating tip-cantilever system in direct contact with the surface (Figure 27). Another key difference lies in the fact that the oscillation amplitude applied in 'tapping-mode' is significantly larger than in nc-AFM.[60] As the

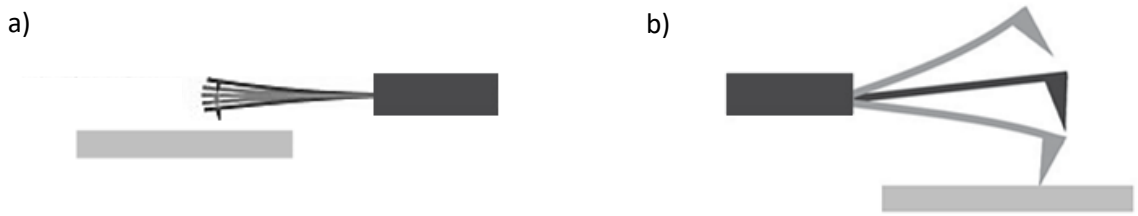

Figure 27. *a) 'Non-contact mode' AFM: image acquisition occurs without contacting the surface of the sample. b) 'Tapping-mode' AFM: the oscilating tip-cantilever system is brought in intermittent contact with the surface and is then raster scanned across the sample. The oscillation amplitude applied to the vibrating system is significantly larger than in 'non-contact mode' AFM.*[52]

vibrating system approaches the sample and the tip starts touching or 'tapping' the surface, the resonant frequency and amplitude of the cantilever oscillations start to decrease (Figure 28). This dampening is caused by the loss of energy as a result of the intermittent tip-surface interactions. These interactions are mainly repulsive in nature and arise from the same forces that are present in contact-mode AFM.[60] Once the predetermined amplitude set point is reached, the approach is complete and the scanning process can begin. The vertically oscillating tip is slowly scanned across the sample and intermittently contacts the surface, generally at a frequency of 50 to 500 kHz. Lower areas of the surface will result in an amplitude *increase* as the cantilever has more 'space' to oscillate before the tip touches the surface. Conversely, high surface features will *decrease* the oscillation amplitude.[60] Analogous to nc-AFM, a feedback loop maintains a constant cantilever oscillation amplitude and the required control signal is used to generate the corresponding topographic image.[60] This operating mode has several advantages compared to the other AFM imaging methods. Lateral forces on the sample are minimized as with nc-AFM, but the lateral resolution is significantly higher. The vertical resolution achievable in 'tapping-mode' is also very high. Because of the brief contact time, the force applied to the surface can be much higher than typically used in cm-AFM without damage to tip or surface. Even the presence of a contaminating water layer on the surface does not pose a problem. The tip penetrates the layer to make contact with the surface and easily retracts afterwards as the oscillation amplitude in 'tapping-mode' is large compared to nc-AFM.[52] Moreover, imaging surfaces in submersed conditions is also possible. In this case, the entire fluid cell is oscillated in order to induce the necessary cantilever oscillations. Otherwise, the fluid medium would uncontrollably dampen the 'free' resonant frequency of the oscillating cantilever. Similar to 'tapping-mode' imaging in air, the oscillation amplitude of the cantilever decreases when the tip starts tapping the surface.[60]

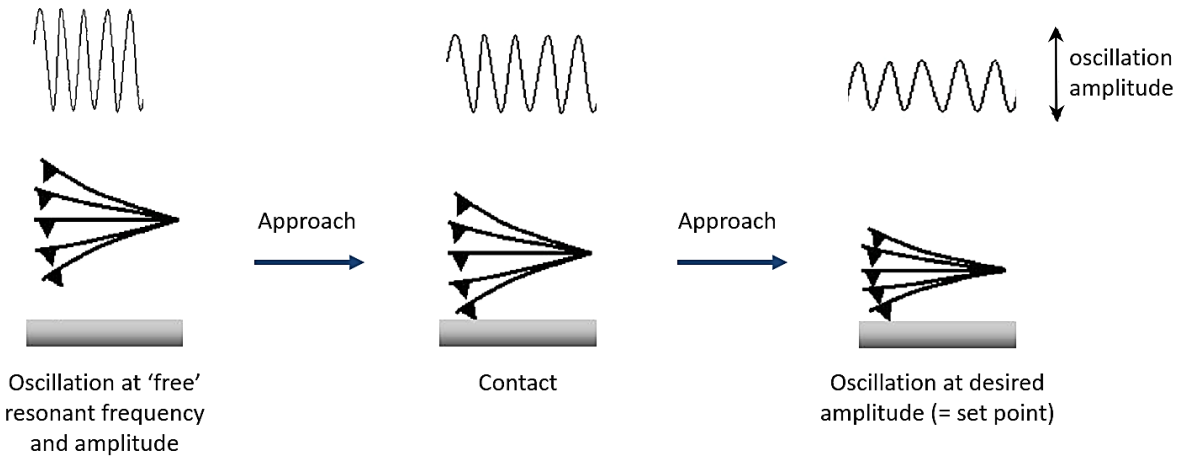

Figure 28. *Illustration of intermittent contact in 'tapping-mode' AFM. Initially, the tip-cantilever system is oscillated at 'free' resonant frequency and amplitude. As the tip closes in on and starts 'tapping' the surface, the resonant frequency and amplitude of the vibrating system start to decrease as a result of the intermittent tip-suface interaction forces. Once the pre-set oscillation amplitude (= set point) is reached, the approach is stopped and the scanning procedure can begin.*

The energy loss resulting from the periodic contact of the tip with the sample surface also induces a 'phase lag' of the cantilever oscillations relative to the driving signal sent to the piezoelectric oscillator. This 'lag' strongly depends on surface composition and increases as more energy is dissipated. By mapping the phase of cantilever oscillations during scanning, nanometer-scale information about (variations in) surface chemical composition, adhesion, friction and viscoelasticity can be obtained. As phase variations and amplitude fluctuations can be monitored simultaneously, 'tapping-mode' AFM provides information about both surface topography and composition.[60]

3.3 Scientific accomplishments

R. Brent *et al.* (2008) have used *ex situ* cm-AFM to investigate the growth mechanism of zeolite L, a unidirectional 12MR nanoporous aluminosilicate with LTL framework structure.[61] Both the hexagonal (001) face and the (100) side-wall of the cylindrical-shaped, hexagonal crystals (Figure 29) were imaged. Figure 30a shows a cm-AFM vertical deflection image of the hexagonal (001) face. Based on the step heights of the terraces observed on this surface, these researchers were able to determine that crystal growth in the c-direction occurs through the incorporation of individual cancrinite cages. The measured step heights were

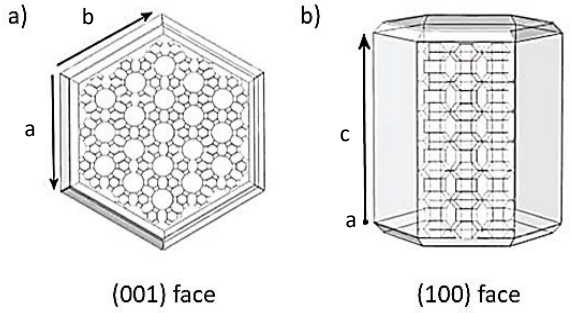

Figure 29. *Schematic representation of the a) hexagonal (001) face and the b) (100) side-wall of the cylindrical-shaped, hexagonal zeolite L crystals.*[61]

0.73 nm and 1.39 nm, corresponding to the height of one and two cancrinite units respectively (Figure 30b). Similarly, terrace heights measured on the (100) side-walls indicated that growth in the a-direction took place as a result of the lateral addition of cancrinite cages, albeit at a lower rate than along the c-direction of the cylindrical crystals.[61]

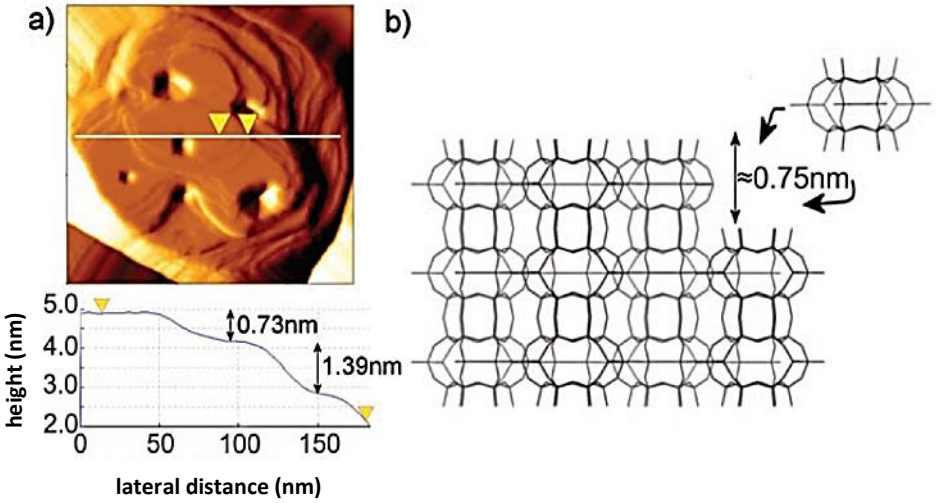

Figure 30. *a) Cm-AFM vertical deflection image of the hexagonal (001) face of a zeolite L crystal. The cross-section analyzed in the graph is highlighted between yellow arrows. Terrace heights of 0.73 and 1.39 nm were observed. b) Schematic representation of the likely cancrinite building unit being incorporated at the (001) surface and which has the equivalent height of one cancrinite cage.*[61]

L. I. Meza *et al.* (2007) on the other hand imaged the surface of a zeolite A crystal, with LTA framework structure and D4Rs and sodalite cages as SBUs, during **dissolution**.[62] This *in situ* AFM experiment was carried out in contact-mode and monitored the crystal surface as it was exposed to different solutions. Although growth and dissolution processes occur via different mechanisms, performing dissolution experiments can provide useful insights about the relative stability of different structural units. One of these dissolution experiments consisted of exposing the surface of zeolite A to a 0.5 M NaOH solution. The accompanying images are presented in figure 31.[62] At the start of the experiment (time = 0 s), the height of all the square terraces amounted to 1.2 ± 0.1 nm. As time progressed, dissolution of the zeolite A surface set in and the terraces started to 'retreat'. As evidenced by figures 31c and 31d, part of the terrace did not dissolve and the original terrace edges remained visible. The height of this persisting layer was 0.3 ± 0.1 nm, indicating that only 0.9 ± 0.1 nm of the terrace initially dissolved. It took 47 min (Figure 31f) before the original terrace was completely removed and dissolution of the next terrace could begin.[62] Taking energetics into account, the writers

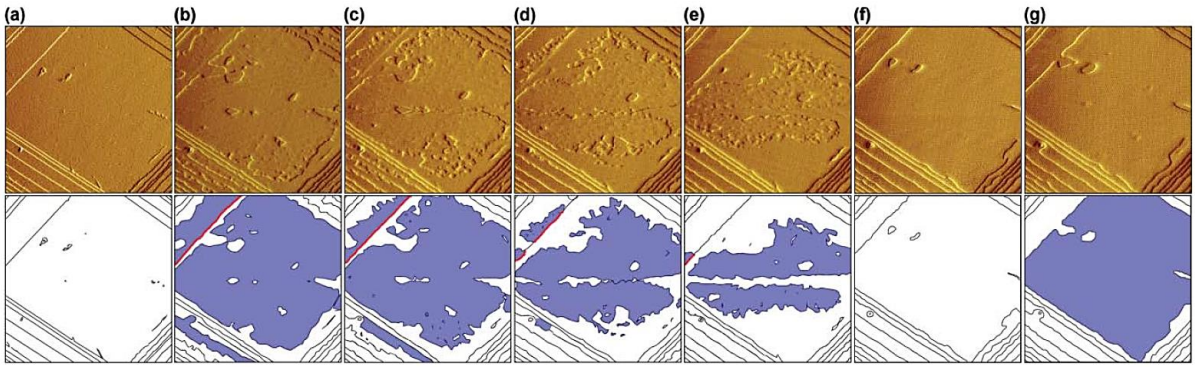

Figure 31. *Cm-AFM vertical deflection images and corresponding schematics of a zeolite A crystal surface dissolved in a 0.5 M NaOH solution during a) 0, b) 31, c) 33, d) 36, e) 38, f) 47 and g) 55 minutes. In the schematics, the black lines correspond to step heights of 1.2 nm and the red lines to 0.3 nm. The blue areas represent layers with step heights of 0.9 nm.*[62]

argued that the surface of zeolite A could either be terminated by sodalite cages or D4Rs. Removal of the 0.9 nm layer would then be consistent with dissolution of the sodalite cages and accompanying terrace 'retreat' whereas removal of the 0.3 nm layer would be in accordance with the uniform dissolution and corresponding removal of the top S4R of the D4Rs. This mechanism is illustrated in figure 32.[62] In both cases, the conclusion is the same: the 0.3 nm layer consisting of D4Rs possesses a higher stability towards dissolution in alkaline environments than the 0.9 nm layer comprised of sodalite cages. This information may prove very important in understanding the actual growth mechanism of zeolite A.[62]

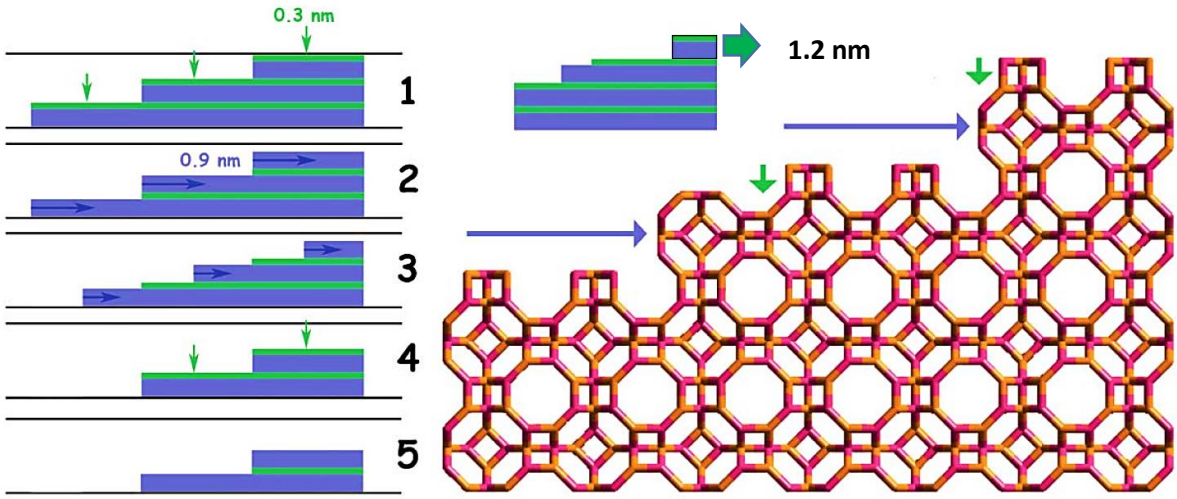

Figure 32. *Schematic illustration of the dissolution mechanism of zeolite A in alkaline conditions. Removal of the top S4R of the D4R layer (green arrow) reduces terrace height by 0.3 nm. Detachment of a sodalite cage, with exception of the bottom S4R base, and accompanying terrace retreat (blue arrow) decreases terrace height by 0.9 nm. The different layers are successively removed during dissolution. The process is either 1-2-3-4 or 2-3-4-5 depending on whether the exterior surface of the crystal is terminated by a D4R layer (green) or sodalite cages (blue) respectively.*[62]

Part II:

Materials and methods

Chapter 4: Experimental procedures and characterization techniques

4.1 Synthesis of zeolitic materials

4.1.1 Synthesis of aluminosilicate with MER framework structure

Crystals of merlinoite with different morphologies were synthesized based on the HSIL preparation method described by M. Haouas *et al.* (2014).[29] The HSIL precursor was prepared by dissolving 110.2 g of KOH (Fisher) in 600 g of water. This solution was then equally divided over six polypropylene (PP) bottles and 59.05 g of TEOS (ACROS, 98%) was added to each of them. These mixtures were thoroughly stirred until phase separation had occurred. The bottom phase, containing the HSIL, was collected and characterized. Its chemical composition amounted to 1 SiO_2 : 1 KOH : 6 H_2O and was determined by gravimetry.[63] The upper phase, consisting mainly of water and ethanol, was discarded of after taking a 20 mL sample for further analysis. The aluminate precursor was synthesized by adding 40 g of water, 41.61 g of KOH (Fisher) and 15.13 g of $Al\{OCH(CH_3)_2\}_3$ (ACROS, 98+%). These solutions were thoroughly stirred until two distinct phases were visible. Again, the bottom phase, containing the aluminate species, was collected and characterized whereas the upper phase, mainly comprised of water and propanol, was disposed of after sampling. Gravimetric characterization of the dense aluminate solution revealed a chemical composition of 0.05 Al_2O_3 : 1 KOH : 2.85 H_2O.[63]

MER synthesis mixtures with molar ratio 0.5 SiO_2 : 0.013 Al_2O_3 : 1 KOH : 8 H_2O were prepared by mixing appropriate amounts of silicate and aluminate precursors with KOH and H_2O. The resulting liquid was stirred for one hour before being transferred to a Teflon-lined stainless steel autoclave. MER syntheses were carried out in a tumbling oven at three different temperatures: 90, 150 and 175 °C. A schematic overview of the synthesis procedure, including precursor preparation, is depicted in figure 33. Samples of the solid phase and the supernatant were taken at room temperature (26 °C) after 2, 4, 8, 16, 32 and 48 hours of synthesis. The solid phase was isolated by centrifuging the product mixture at 13000 rotations per minute (rpm) and carefully removing the supernatant. The crystallized solids were then washed four times with water and dried overnight at 60 °C.

In a second experiment, a batch of MER crystals was synthesized at 90 °C in static conditions for 28 days. The chemical composition of the synthesis solution was the same as in the previous series of experiments (0.5 SiO_2 : 0.013 Al_2O_3 : 1 KOH : 8 H_2O). This mixture was divided equally over four PP bottles. Every 7 days, a sample of the crystallized solids was taken and characterized. The sampling protocol was analogous to the one described above.

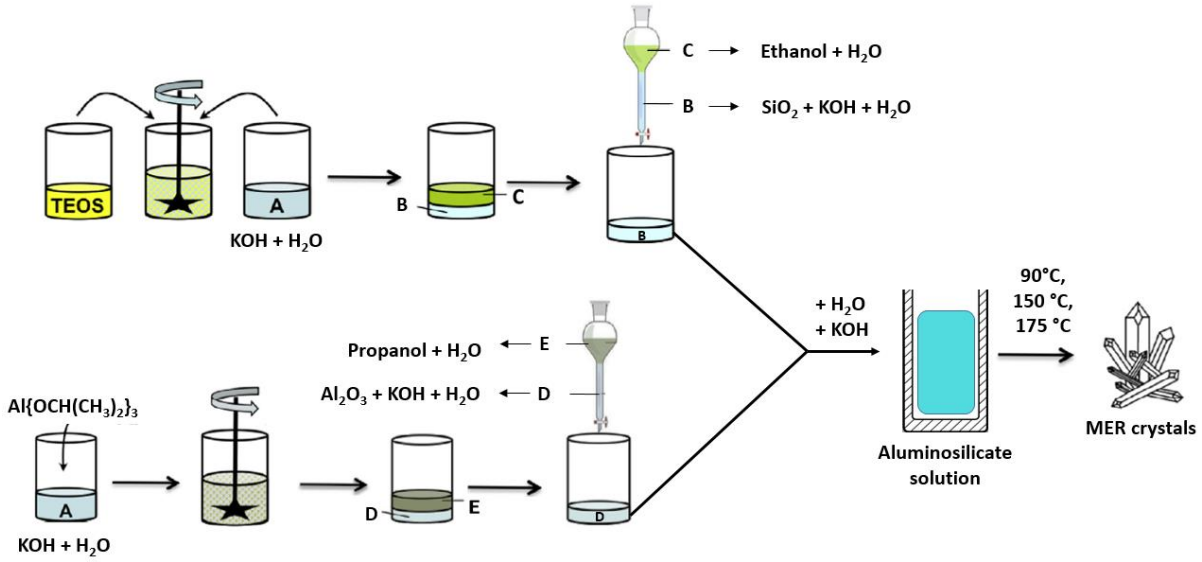

Figure 33. *Synthesis of MER crystals from aluminosilicate precursor. This liquid is prepared by adding appropriate amounts of the HSIL (B) and aluminate precursor (D) to H2O and KOH. The silicate solution (B) is obtained by mixing TEOS with KOH and H2O and collecting the bottom phase of the resulting biphasic solution (B+C). Analogously, mixing* $Al\{OCH(CH_3)_2\}_3$ *with KOH and* H_2O *results in the formation of a biphasic mixture (D+E) that ultimately yields the desired aluminate precursor after recovery of the bottom phase. In both cases, the upper phase (C and E) consists of an aqueous alcohol solution which is disposed of after sampling.*[29]

Additionally, needle-shaped MER crystals were received from Dr Mohammed Haouas, a member of the TectoSpin NMR research group of the Institut Lavoisier de Versailles. These crystals were prepared from an aluminosilicate mixture with chemical composition 0.5 SiO_2 : 0.013 Al_2O_3 : 1 KOH : 8 H_2O. Synthesis occurred at 170 °C for 48 hours and was carried out according to the protocol described by M. Haouas *et al.* (2014).[29]

4.1.2 Synthesis of germanosilicate with UTL framework structure

'As synthesized' (AS) and calcined UTL samples were received from COK. The synthesis of this germanosilicate was carried out according to the protocol described by O. V. Shvets *et al.* (2008).[64] The SDA used in this work was (6R,10S)-6,10-dimethyl-5-azoniaspiro[4,5]-decane hydroxide. Amorphous germanium oxide and silica were added to a solution containing the SDA and the mixture was stirred at room temperature for 30 min. The resulting fluid gel was transferred to a Teflon-lined autoclave and heated at 175 °C for 3 - 9 days under continuous agitation. The solid UTL product was recovered after filtering and drying the solid phase at 60 °C overnight. Calcination of AS UTL was carried out in air at 550 °C for 6 hours, effectively removing the SDA.[64]

4.1.3 Inverse σ transformation of IM-12 (parent UTL) to COK-14 (OKO)

-COK-14 samples were received from COK and the phase transformation from IM-12, the parent UTL material, to COK-14 (OKO framework structure) was performed according to the procedure originally developed at COK by E. Verheyen *et al.* (2012).[35] By heating a suspension of calcined IM-12 zeolite in a 12 M solution of HCl at 95 °C, the desired phase transformation was achieved within two days. Subsequent washing removed the Ge-atoms from the structure and calcination at 550 °C yielded the fully connected COK-14 zeolite with OKO framework structure. In ambient conditions however, rehydration occurs and COK-14 spontaneously converts back to the interrupted -COK-14 framework.[35]

4.1.4 Synthesis of germanosilicate with IWW framework structure

AS IWW samples were received from COK and synthesized following a method originally described by R. Yuan *et al.* (2016).[65] 5-azonia-spiro[4,4]-nonane hydroxide was used as SDA. The synthesis mixture consisted of crystalline germanium oxide, TEOS, the SDA and water. The mixture was thoroughly stirred and then autoclaved at 175 °C for three days while tumbling. The IWW material was recovered after filtering and washing the solid phase with deionized water, and drying the crystalline solids overnight at 60 °C.[65]

4.2 Post-synthesis treatments

4.2.1 Basic and acid treatment of needle-shaped MER sample

The needle-shaped MER crystals were subjected to an alkaline and acid post-synthesis treatment to investigate the effect of these conditions on the surface features of the crystals. In one experiment, 20 mg of MER was continuously stirred for 4 hours in 0.78 mL of a 0.5 M NaOH (Fisher) solution (pH 13.38) at 85 °C. In a second experiment, 15 mg of MER was treated under similar conditions but with 0.59 mL of a 0.5 M perchloric acid ($HClO_4$, Sigma-Aldrich, 70%) solution (pH 0.39).

4.2.2 Wet ball milling of -COK-14 and UTL-type zeolite

'Wet ball milling' is a mechanical post-synthesis treatment intended to decrease the particle size of materials by grinding them with small balls in a liquid environment. Smaller particles lead to higher surface areas per volume ratio. For catalytically active materials such as certain types of zeolites, larger surface areas significantly increase the accessibility of the catalytically active sites. Ultimately, increased catalytic activities are achieved as diffusion-related issues are greatly diminished.[66]

The milling is achieved by continuously rotating a container. In this context, the container holds a mixture of zeolite crystals, solvent and glass or zirconia milling balls. 'Wet ball milling' experiments were conducted with a Turbula T2F (Eskens, Figure 34), a device which rotates a container in an ∞-shaped loop.[67] Several parameters can be adjusted in order to influence the outcome of the milling process. The most important ones are the material, size and amount of milling balls, the number of rotations per minute, the amount of sample, the dimensions of the container, and the solvent.

Ball milled -COK-14 samples were received from COK and treated according to the method described by M. De Prins (2014).[68] One sample was milled in isopropanol with 2 mm zirconia (ZrO_2) balls during one hour at 35 rpm. A second -COK-14 sample was treated in isopropanol with 5 mm ZrO2 balls during 24 hours at the same rotation speed.

In this work, an additional ball milling experiment was carried out on an AS UTL sample. 125 mg of AS UTL was added to a 25 mL PP vial containing 12.5 g of 2 mm glass balls. The vial was then filled with ethanol and rotated at 35 rpm at room temperature for 2 hours. After the milling treatment, the glass balls were separated from the liquid phase by means of filtration. The residual suspension containing AS UTL crystals was then dried at 60 °C overnight to evaporate the ethanol. A risk assessment of all the experiments carried out in this work is provided in Appendix G.

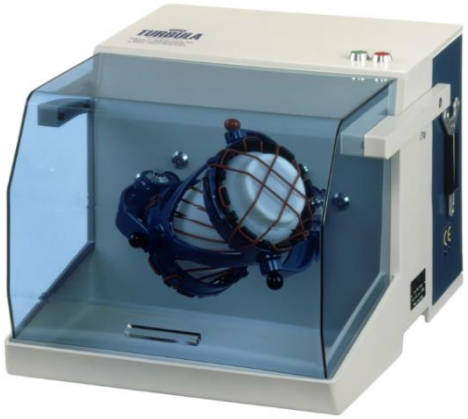

Figure 34. *Mechanical milling: T2F Turbula.*[67]

4.2.3 Treatment of as-synthesized UTL with pestle

An AS UTL sample was also treated manually with a pestle. This treatment was carried out by grinding the sample in a mortar with long hauls for 15 minutes. Similar to the ball milling experiments described earlier, this procedure aimed to increase the surface area of the solid particles. Instead of achieving this result by reducing the size of the particles, an attempt was made to *delaminate* the layered germanosilicate sample by manually applying tangential pressure.

4.3 Characterization techniques

4.3.1 X-ray diffraction

X-ray diffraction (XRD) is an important technique to gain insight in the atomic and molecular structure of solid, crystalline samples. Crystalline materials are typically made up of atoms which are arranged in a well-defined, regular pattern. As described earlier, the smallest recurring motif in this pattern is the 'unit cell'. The dimensions of this unit cell are specific for each type of material and they can therefore be used to identify the solid phase under observation. For zeolites in particular, a distinction can be made between the various framework types as each lattice structure is different and has a unique unit cell. The characterization and identification of crystalline solids occurs by exposing the sample to a beam of X-rays with wavelength λ comparable to interatomic distances in solids (0.5 – 2.5 Å).[69] These X-rays are scattered in all possible directions by the lattice atoms. In amorphous or non-crystalline materials, these waves cancel each other out, a phenomenon known as 'destructive interference'. In crystalline materials however, 'constructive interference' or 'diffraction' can take place. When the difference in path length between two scattered waves is equal to an integer multiple of their wavelength, these waves remain 'in-phase' and combine. The newly formed wave then propagates towards the detector with the added amplitude of the constituting waves. Taking into account the angle of incidence, this requirement translates into Bragg's law:[69]

$$n * \lambda = 2 * d_{hkl} * \sin\theta$$

where *n* is a positive integer, λ the wavelength of the incident X-ray beam, θ the angle of incidence and d_{hkl} the interplanar distance between equidistant *hkl* lattice planes. The *hkl* notation used to specify the different lattice planes in a crystal is referred to as 'Miller indices'. This concept of 'constructive interference' is illustrated in figure 35.[69]

Ultimately, a diffraction pattern consisting of several reflections is obtained by varying the value of (2) θ and recording the intensity of the scattered X-rays. Both the position and the intensity of these reflections depend on the crystalline structure of the material. As each structure has a unique pattern, unknown samples can be identified by comparing the pattern obtained to databases.[69]

XRD patterns of the zeolites studied in this work were recorded on a STOE STADI P Combi diffractometer with focusing Ge(111) monochromator ($CuK_{\alpha 1}$ radiation, λ = 0.154 nm) with high throughput set-up in transmission geometry and with 140°-curved image plate position sensitive detector (IP PSD) from 0 to 62.5° 2 θ.

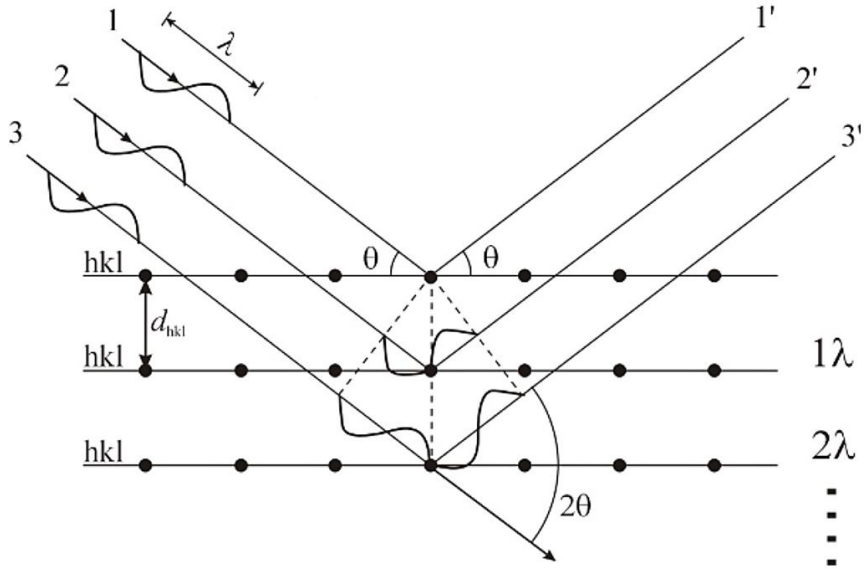

Figure 35. *Constructive interference in a crystalline solid with distance d_{hkl} between equidistant hkl lattice planes. Only those scattered waves, whose difference in path length inside the crystal (= $2 * d_{hkl} * sin\ \theta$, green arrow) is equal to an integer multiple (= n = 1, 2,…) of their wavelength (= λ) , will remain 'in-phase' and combine. This effect becomes more pronounced the more equidistant hkl planes occur in the crystal lattice.*[69]

4.3.2 Scanning electron microscopy

A scanning electron microscope (SEM) is a type of electron microscope that images the outer surface of a solid specimen by raster scanning the sample with a focused beam of high-energy electrons. These electrons interact with atoms near and at the surface, generating various signals that reveal information about the morphology of the sample and the topography and composition of its surface. Backscattered electrons (BSEs) for instance consist of electrons which are elastically 'back-scattered' by the atoms in the specimen. As no energy is dissipated in this scattering process, these BSEs possess the same kinetic energy as the electrons from the incident electron beam. As heavy atoms with high atomic number backscatter electrons more strongly than lighter elements, detection of BSEs allows for a qualitative distinction between surface areas with different chemical composition. Areas with heavier atoms and more electron density will appear brighter in the resulting SEM image. High resolutions in the order of nanometers can be achieved and samples can be imaged in a great variety of conditions and at a wide range of temperatures. However, non-conductive samples generally require a thin protective coating of electrically conducting material to prevent charge accumulation and damage to the sample.

In this work, SEM was carried out on an FEI Quanta 200 ESEM in high vacuum mode and used to determine the average size and morphology of the zeolite crystals. Samples were dusted onto carbon tape and platinum-coated prior to analysis. Images were collected in secondary electron mode with an applied voltage of 15 or 20 kV and a working distance of 10 mm.

Additional high-resolution scanning electron microscopy (HR-SEM) was performed on a Nova NanoSEM 450 (FEI Eindhoven). Powder samples were dispersed on carbon tape attached to aluminum stubs and imaged without any further sample modification. High-resolution images were obtained at low voltages (2 kV) using a Centered Back Scattering detector (CBS, a new type of BSE detector) combined with Beam Deceleration Mode.

4.3.3 Inductively coupled plasma

Inductively coupled plasma (ICP) is the most commonly used technique for the determination of trace concentrations of elements in samples. Plasma consists of electrons and ions and is one of the four fundamental states of matter, the others being solid, liquid and gas. The sample is nebulized into an aerosol and sprayed directly into the plasma flame. Gaseous and liquid samples can be injected directly, whereas solid samples need to be pretreated by acid digestions. Inside the plasma, the molecules within the sample are broken down into charged ions and electrons as temperatures can run up to 6.000 to 10.000 K.[70] As electrons and cations recombine, electromagnetic radiation is emitted at wavelengths characteristic of a particular element. The concentration of each element in the sample is then derived from the radiation intensity observed by the detector. This detection method is referred to as 'optical emission spectroscopy' (OES) and is often used in combination with ICP.[71]

ICP analysis was carried out on a -COK-14 sample to determine the Ge-content. Experiments were performed on a Varian 720 ES, an axial simultaneous ICP-OES with cooled cone interface and oxygen free optics which make it possible to measure in low UV. Sample preparation consisted of dissolving the solid zeolite sample in hydrogen fluoride (HF) and boric acid (H_3BO_3). 32 mg of -COK-14 is put in a polytetrafluoroethylene (PTFE) cup along with 0.5 mL *aqua regia* (with a 1 HNO_3 : 3 HCl chemical composition) and 3 mL HF (40 %). This cup is heated at 110 °C for 1 h and cooled afterwards. 10 mL of water is then added and the resulting mixture is poured in a PTFE 100 mL volumetric flask. Finally, 2.8 g of H_3BO_3 (99.99%) is added to the flask and the final solution is diluted with water until a volume of 100 mL is obtained.

4.3.4 Nuclear magnetic resonance spectroscopy

Nuclear magnetic resonance (NMR) spectroscopy is a widely applied analytical method which exploits the magnetic properties of certain atomic isotopes. These isotopes have a characteristic nuclear spin. When exposed to an external magnetic field, this spin typically gives rise to a subdivision of the energy levels. In sole presence of the external magnetic field, population of these energy levels follows a Boltzmann distribution. Exposure to and absorption of a second radio frequency field results in a shift of the population distribution in favor of the higher energy levels. After this radio frequency pulse, the population distribution gradually resets itself to Boltzmann equilibrium through relaxation. This population redistribution can be detected and transformed into the NMR spectrum of the isotope under observation. This spectrum is composed of peaks which contain valuable information. The position of the peak depends on the chemical and electronic environment of the isotope. Neighboring atoms and solvent molecules induce a *chemical shift* in the position of the peak. The intensity of and the area under the peak are proportional to the concentration of the species being analyzed. Consequently, NMR spectroscopy can be used to resolve the structure of unknown samples and determine the speciation of a known nucleus in solution.

The supernatant solutions of the MER syntheses at different temperatures (90, 150 and 175 °C) were analyzed by ^{27}Al, ^{29}SI and ^{39}K NMR at room temperature (26 °C) to determine their concentrations. The experiments were carried out on a Bruker Avance 500 spectrometer, operating at 130.326 MHz for ^{27}Al, 99.353 MHz for ^{29}Si and 23.338 MHz for ^{39}K. In a modified background-free probe, 10 mm PTFE tubes were used to avoid the strong background signal of glass and quartz tubes. The ^{29}Si spectra were recorded with single-pulse acquisition using a pulse of 3.71 µs (45°), a recycle delay of 5 s, an acquisition time of 1.6 s and an accumulation of 1024 scans. The ^{27}Al NMR spectra were obtained by applying 2.14 µs (15°) pulses, a recycle delay of 0.1 s, an acquisition time of 26 ms and accumulating 1024 scans. The ^{39}K NMR spectra were recorded with a pulse of 6.25 µs (22°), a recycle delay of 0.1 s, an acquisition time of 0.4 s and accumulating 1024 scans. The chemical shifts were determined using tetramethylsilane (TMS) as a reference for ^{29}Si, an aqueous solution (0.7 mol.L^{-1}) of $Al(NO_3)_3$ for ^{27}Al and a solution of 2 mol.L^{-1} KCl for ^{39}K. NMR quantification was performed by spectral decomposition analysis. Simulation of all lines was conducted by using an NMR notebook software program with Lorenzian shape except for the broad bands in ^{29}Si, which were fitted with Lorenzo-Gaussian shapes to better simulate the chemical shift distributions.

4.3.5 Atomic force microscopy

'Contact-mode' AFM was carried out at the Centre for Nanoporous Materials (University of Manchester) and performed in air on a JPK Nanowizard II Bio-AFM mounted on an inverted Axiovert 200 MAT optical microscope (Figure 37). Samples were prepared by heating a small fragment of thermoplastic resin on a glass slide at 50 °C for 1.5 minutes. A small amount of zeolite sample was then dispersed on the softened resin and re-heated at 50 °C for an additional minute to firmly fix the sample in the thermoplast. Finally, excess sample was removed from the thermoplast by means of compressed air. Silicon nitride tips (Bruker probes NP-10, spring constant 0.58 Nm^{-1}) were used with a scan rate of 1 - 2 Hz. Images were analyzed using the JPK Data Processing software. A line-fitting tool was applied to the images and individual terraces were flattened using a plane fit for cross sectional analysis. Average step height and standard deviation were determined by measuring the height of 25 different steps.

'Tapping-mode' AFM images were obtained on Cypher ES equipment (Figure 38) at the Molecular Imaging and Photonics department of the KU Leuven. An aluminum coated, N-type doped silicon AFM probe from Olympus with spring constant of 2 Nm^{-1} and 'free' resonant frequency equal to 70 kHz was used. All image corrections were performed with the SPIP 6.0.2 software package.

Figure 36. *Contact-mode AFM set up.*

Part III:

Results and discussion

Chapter 5: MER

5.1 Growth of MER synthesized at 90 °C for 28 days

Two distinct crystalline phases, chabazite (CHA) and MER, were observed for the MER synthesis at 90 °C, as evidenced by the XRD patterns (Figure 37). In early stages of the synthesis, a significant amount of CHA is formed. In time, the fraction of CHA in the final solids mixture decreases in favor of MER. This 'coupled growth' phenomenon is evidenced by the decrease in intensity and surface area of reflections specific to CHA and simultaneous increase of characteristic MER reflections (Figure 37). Formation of CHA during MER synthesis is often observed, especially at temperatures below 150 °C.[72] Evolution in size and morphology of the solids synthesized at 90 °C during 7, 14, 21 and 28 days is imaged by means of SEM (Figure 38). Crystal morphology changes noticeably over time and evolves from a discus-shape (Figure 38a) to a rectangular shape with layered surface (Figures 38d and 39). Combined with the XRD patterns, these results indicate that the discus-shaped crystals are likely to have a CHA framework structure, whereas the second phase consists predominantly of MER.

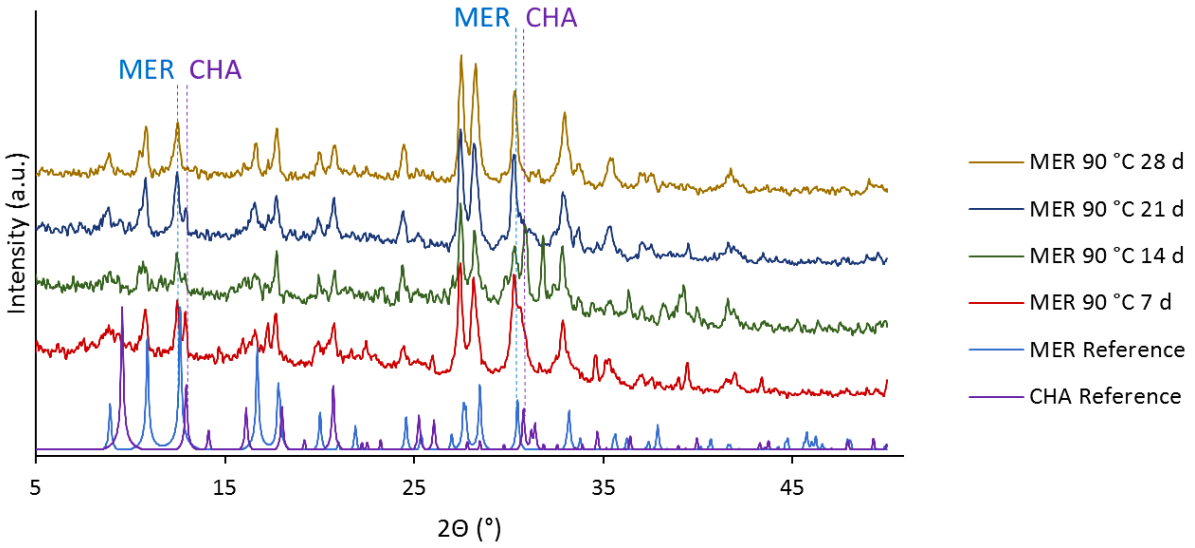

Figure 37. *XRD patterns of solid phase recovered from MER synthesis at 90 °C for: 7 (dark red), 14 (dark green), 21 (dark blue) and 28 days (brown). CHA and MER reference patterns are presented in purple and light blue respectively. Characteristic reflections of CHA and MER are highlighted in purple and light blue.*

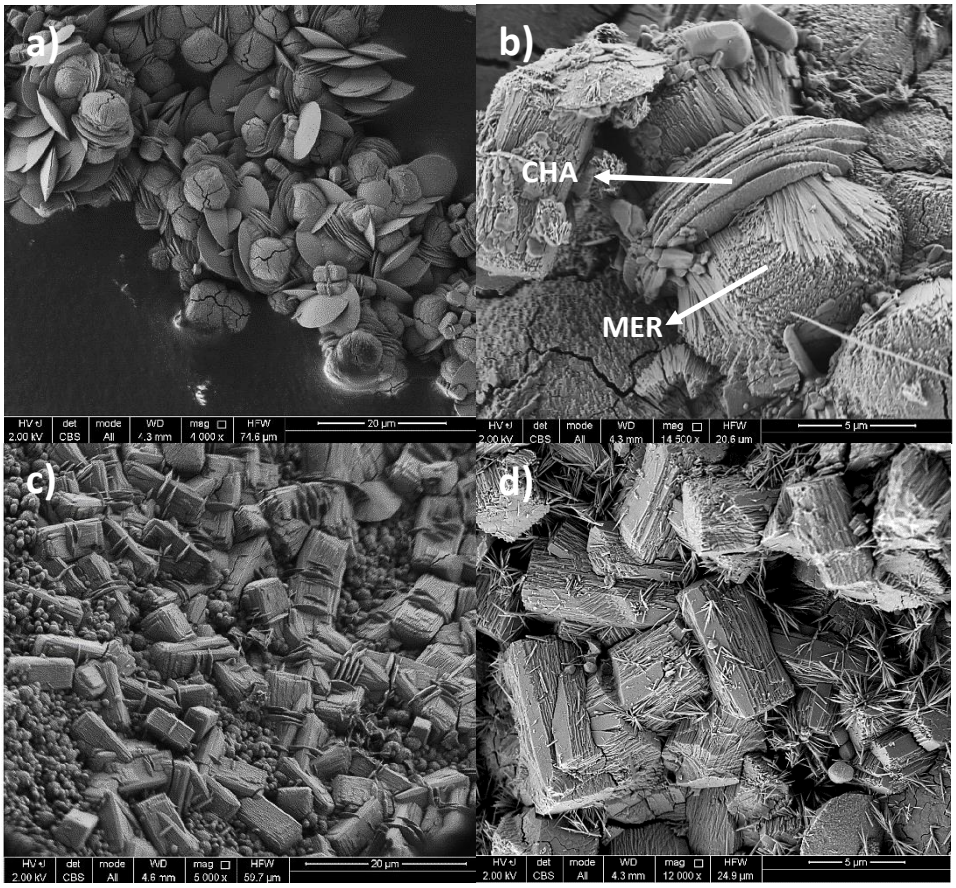

Figure 38. *SEM images of crystallized solids recovered from MER synthesis at 90 °C after a) 7, b) 14, c) 21 and d) 28 days. The crystalline particles are predominantly discus-shaped in the early stages of the synthesis (Figure 38a). A second phase emerges after 14 days which appears to grow out of the discus-shaped crystals (Figure 38b). The morphology of the solid crystals takes on a rectangular shape with layered surface features in later stages (Figure 38d). This evolution is accompanied by the gradual disappearance of the discus-shaped structures.*

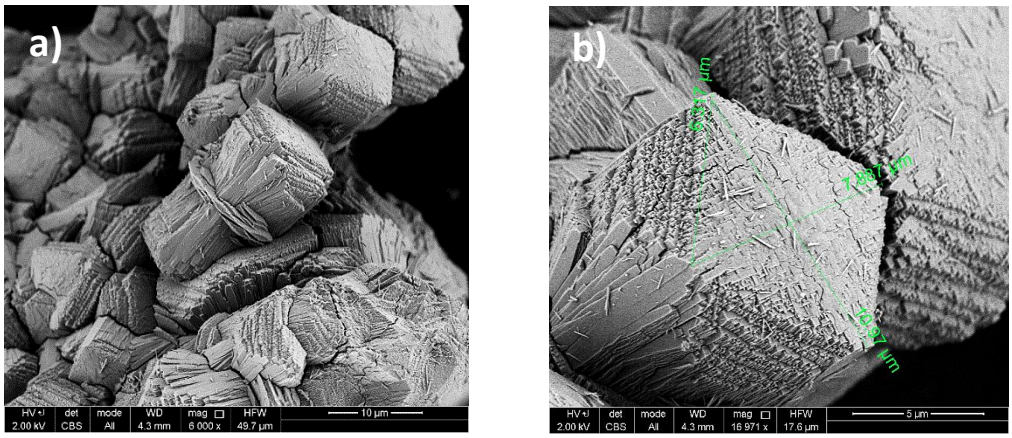

Figure 39. *a) Enlarged SEM image of solid phase recovered from MER synthesis at 90 °C after 28 days. b) The width and diameters of the quadrangular faces amount to 6.317 µm, 7.887 µm and 10.970 µm respectively.*

The crystals were also analyzed with cm-AFM. The extensive presence of discus-like structures in the solid phase recovered after 7, 14 and 21 days however heavily obstructed the imaging process. Therefore, the surface of these samples could not be imaged. The surface of the MER crystals obtained after 28 days on the other hand was successfully scanned and the resulting AFM images are provided in figure 40. The layered surface strongly resembles the one depicted in figure 38d. Due to the large height differences of the surface under observation, the contrast of the images was not sufficiently high to image surface features (such as terraces, steps,…) of the individual layers. Nonetheless, the vertical deflection images clearly show that growth of MER in these conditions occurs through **'birth and spread'**, a mechanism which is indicative of high supersaturation conditions as elaborated in section 2.2.

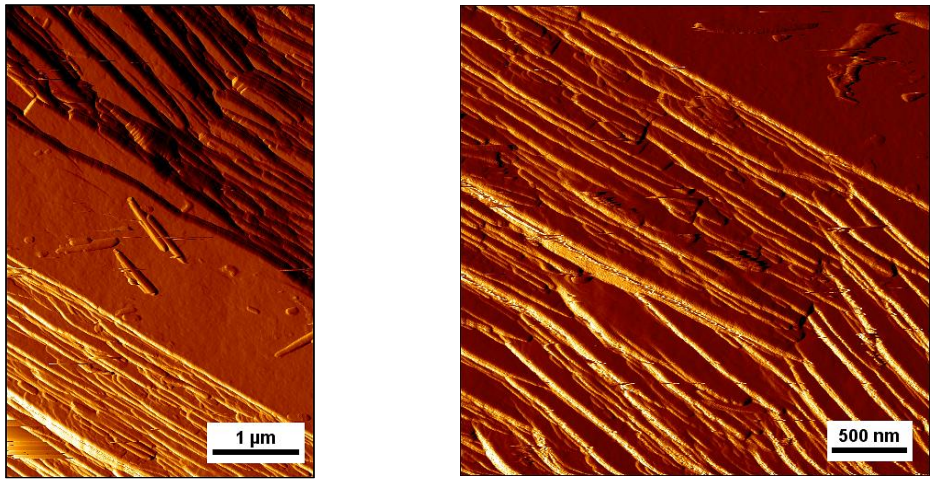

Figure 40. *Cm-AFM vertical deflection images of MER samples synthesized at 90 °C for 28 days.*

5.2 Growth of needle-shaped MER

MER samples received from Dr. Mohamed Haouas were characterized with SEM (Figure 41) and cm-AFM (Figure 42). The SEM images demonstrate these MER crystals are needle-shaped. The AFM images show that the crystal surface is completely covered with spiral patterns, indicating MER grows through **spiral growth** in these synthesis conditions. Spiral growth typically occurs at low supersaturation levels, as described in section 2.3.

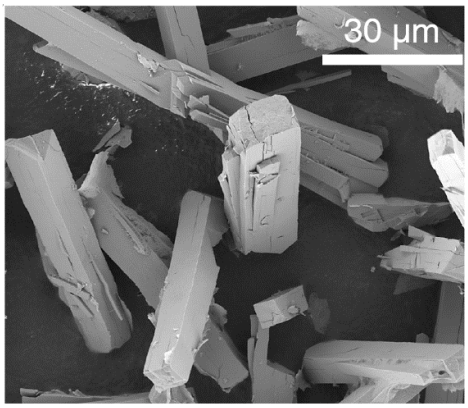

Figure 41. *SEM image of needle-shaped MER crystals.*

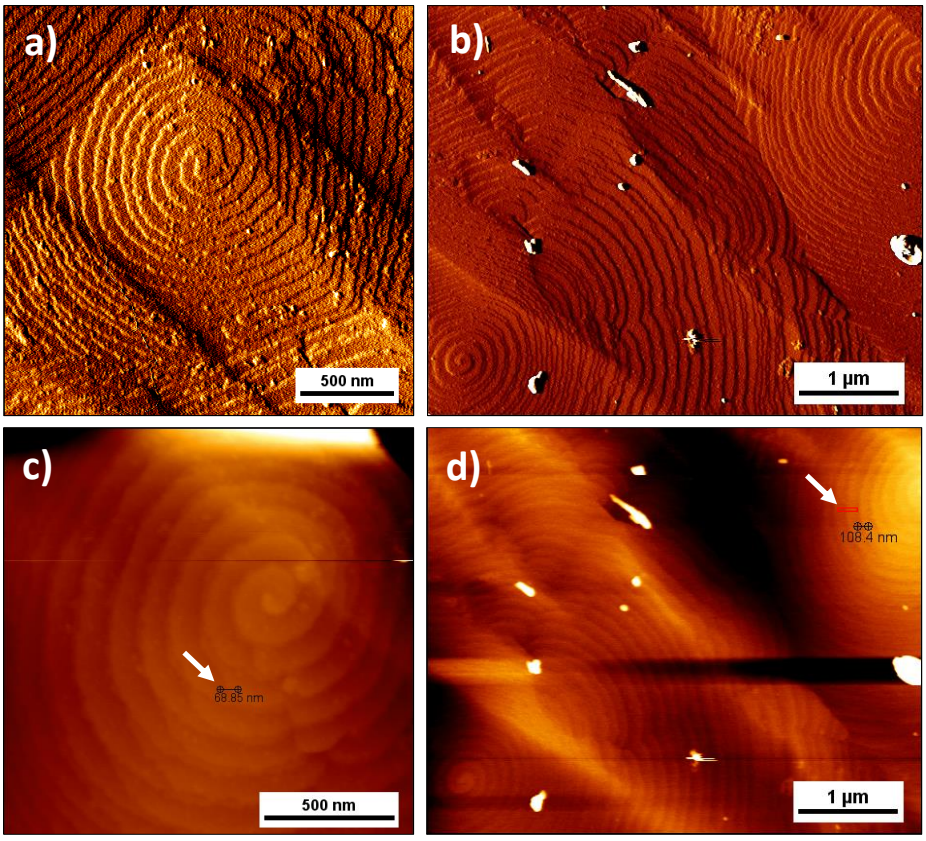

Figure 42. *a) Cm-AFM vertical deflection image of interlaced spiral on the surface of needle-shaped MER crystals. b) Cm-AFM vertical deflection image of double spirals. c) Cm-AFM height image of interlaced spiral (enlarged view). The brighter the color, the higher the relative position. d) Corresponding height image of figure 42b. The line segments added to figures 42c and 42d were respectively used for cross-sectional height analysis of single and double step heights. The red rectangle in figure 42d highlights the area used for histogram analysis.*

Height analysis of the cross-section in figure 42c revealed a single step had a height of 0.60 ± 0.10 nm. Analogously, analysis of the cross-section in figure 42d yielded a double step height of 1.30 ± 0.10 nm for the double spirals. A histogram, mapping the frequency of the different heights observed in the highlighted area in figure 42d, yielded a similar average step height of 1.40 nm. These results are summarized in figure 43. A hypothesis concerning the crystal growth mechanism and growth direction was formulated by comparing the step heights to the tetragonal unit cell parameters of the MER framework structure: a = 1.4012 nm, b = 1.4012 nm and c = 0.9954 nm. The angles between the axes (α, β and γ respectively) are all 90°.[12] The height of a single spiral terrace was determined at 0.60 ± 0.10 nm, which corresponds to half the length of the MER unit cell in both a- and b-directions.

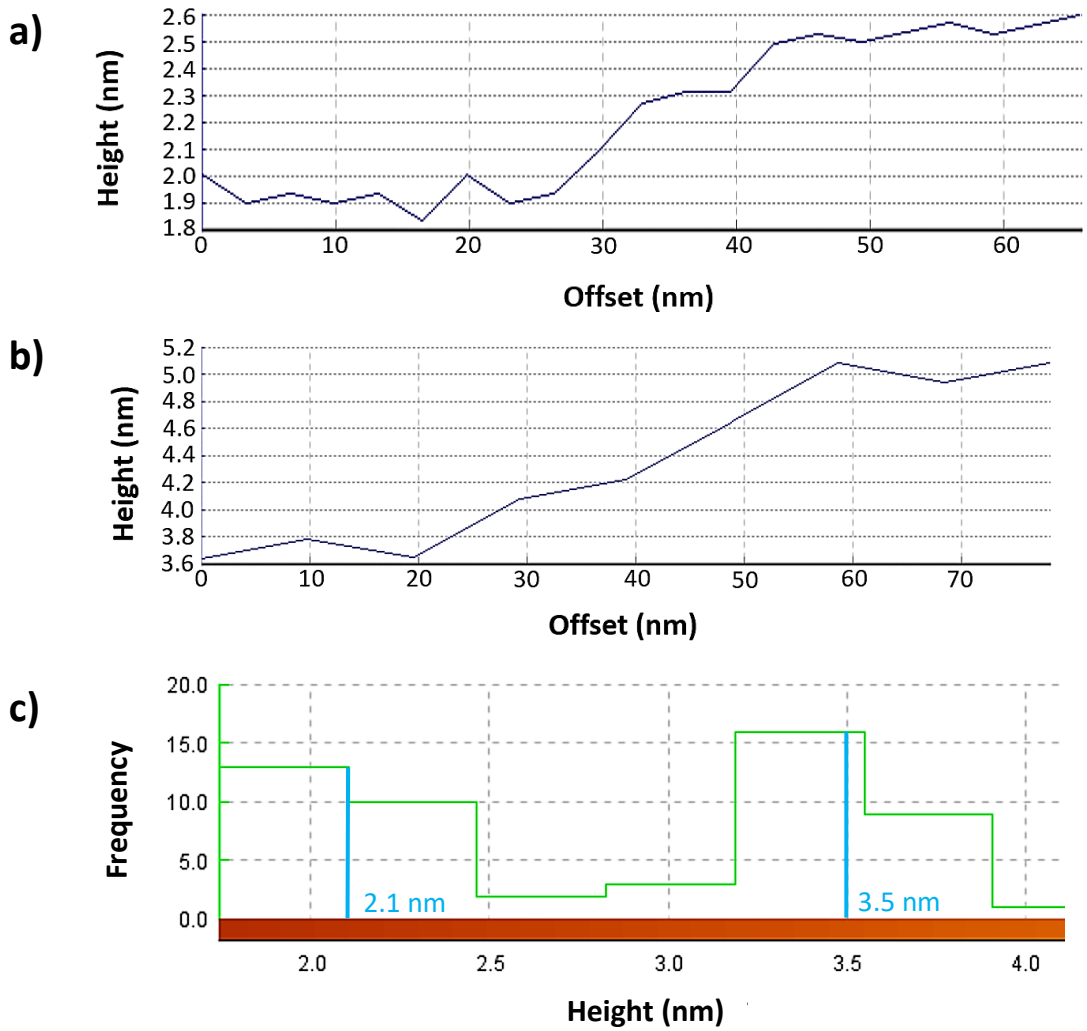

Figure 43. *a) Height profile along the line segment drawn in figure 42c. The average height of a single spiral terrace is 0.6 nm. b) Height profile along the line segment highlighted in figure 42d. The average double step height amounts to 1.3 nm. c) Histogram of the area enclosed in the red rectangle drawn in figure 42d. The average height of the lower and upper terrace is depicted in blue, resulting in an average height of 1.4 nm for the double spirals.*

As a and b have the same values, elongation of the crystal occurs on the (001) face, along the c-direction, resulting in the characteristic needle-shaped morphology. These observations indicate that growth was either observed on the (100) or the (010) face. Figure 44a provides an overview of the different crystallographic faces. A schematic illustration of the crystal structure of the (100) surface is depicted in figure 44b. The height of the spiral terraces also indicates that the initial screw dislocations in the crystal structure have a height of 0.60 ± 0.10 nm or a multiple thereof.

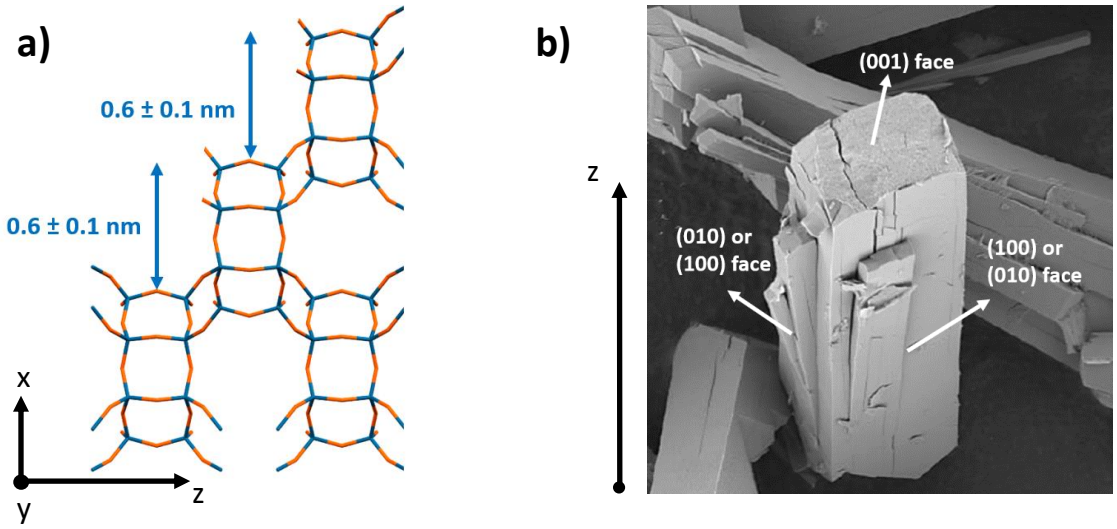

Figure 44. *a) Schematic illustration of (100) crystal surface. O atoms are represented in orange, the tetrahedrally coordinated Si- or Al-atoms in blue. The height of each successive layer is 0.6 ± 0.1 nm and corresponds to half the length of the MER unit cell in the a-direction (along the x-axis). b) SEM image of the (100), (010) and (001) crystallographic faces visible on the surface of a needle-shaped MER crystal.*

5.3 Influence of synthesis temperature on crystal growth and morphology

Synthesis of MER from one precursor mixture (0.5 SiO_2 : 0.013 Al_2O_3 : 1 KOH : 8 H_2O) but at different temperatures yielded crystals with distinct morphology and growth mechanism. This result can be explained by taking into account the relation between temperature T and supersaturation σ, was already introduced in section 2.1.:

$$\sigma = \frac{1}{e^{\frac{\Delta G_v \, \Omega}{k \, T}}} - 1$$

As growth occurs spontaneously and ΔG_v assumes a negative value, it follows that σ will increase as T decreases. NMR quantification of the elements (Si, Al and K) in the supernatant solution of the syntheses carried out at 90, 150 and 175 °C was performed to further evidence this inverse relation. As defined in section 2.1, σ is the difference between actual concentration *C* and equilibrium concentration or solubility C_0 of a species at a given temperature. Consequently, evolution of the concentration of a species over time can be used to qualitatively determine supersaturation conditions. The Si- and K-content of the synthesis mixture were deliberately kept high by adding excess amounts of KOH and silicate precursor. This allows to neglect concentration changes caused by incorporation of these species in the growing framework, as illustrated by the ^{29}Si and ^{39}K NMR

spectra (Appendices B and C respectively). In this work, supersaturation was determined by quantifying the concentration of aluminate species in the supernatant after 2, 4, 8, 16, 32 and 48 hours of synthesis. The XRD patterns of the solid phases collected at the end of these syntheses are presented in Appendix D. Evolution of Al concentration and supersaturation over time is shown in figure 45. The accompanying ^{27}Al spectra are provided in Appendix A. As sampling occurred at room temperature, supersaturation is determined with respect to the solubility of Al-species at room temperature (26 °C). This solubility amounts to 16 mole% of the initial aluminum concentration, as evidenced by the convergence of the three curves depicted in figure 45.

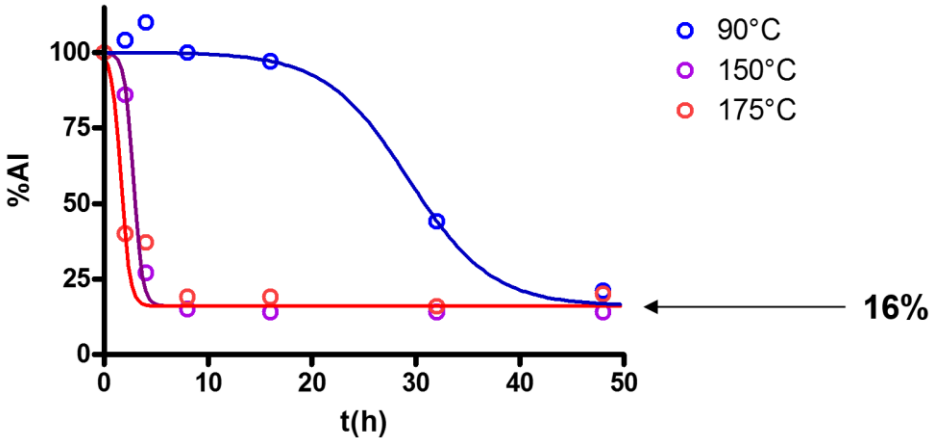

Figure 45. *Evolution of Al concentration in the supernatant as function of time (in hours) after synthesis at 90 (blue), 150 (purple) and 175 °C (red). The three curves converge at 16% as the solubility of the aluminate species is reached. Solubility and supersaturation are determined with respect to room temperature (26 °C) as the product mixture was allowed to cool before sampling. Concentrations are expressed as percentages of the initial aluminate concentration (= 100%). Deviations in the measurements can be attributed to anomalies with the NMR probe.*

According to classical crystallization theory, larger crystals are formed in low supersaturation conditions as crystal growth prevails and crystals grow faster than they nucleate. High supersaturation levels on the other hand result in the formation of smaller-sized crystals as nucleation dominates. These observations are valid under the assumption that temperature and the associated thermal energy of both systems are the same: different degrees of supersaturation are obtained by adding different amounts of precursors to the synthesis mixture. In this work, supersaturation was varied by changing T rather than the composition of the synthesis mixture. Temperature also greatly affects the kinetics of the crystallization process as nucleation and growth rates are strongly T-dependent.

At 90 °C, supersaturation is high, as depicted by the blue curve in figure 45. In these conditions, classical crystallization theory dictates that nucleation should prevail. The thermal energy provided by the system is however not sufficiently high to overcome the energetic barrier associated with nucleation. The nucleation process thus proceeds at a very slow rate and no significant changes in Al concentration are observed for 16 hours. After 32 hours, the Al-content of the supernatant solution has decreased significantly, indicating an appreciable amount of stable nuclei has been formed and crystal growth has set in. As crystal growth is initiated in high supersaturation conditions, the prevailing growth mechanism is expected to be **layer growth** or **'birth and spread' growth**. This hypothesis is evidenced by the AFM images shown in figure 40 (p. 51). As temperature decreases during the quenching process, supersaturation will even increase. Crystallization then proceeds at elevated rates and the Al concentration rapidly diminishes. This effect is similar to 'seeding', where addition of seed crystals to the synthesis mixture greatly improves the crystallization rate. This improvement can be attributed to the increased surface area where the framework-forming species can attach to. In addition, the presence of stable nuclei prior to synthesis might catalyze the formation of new nuclei, speeding up the crystallization process.[73] After 48 hours, crystal growth comes to an end as the solubility of the Al-species (at 26 °C) is reached.

At 150 °C and 175 °C on the other hand, the system provides sufficient thermal energy to overcome the energetic barrier for nucleation and stable nuclei are extensively and rapidly formed. Due to the 'seeding' effect, crystallization takes place in minutes as temperature decreases due to quenching and accompanying supersaturation increase. Solubility is already reached after 8 hours, illustrating the rapid crystallization process. Because of the low supersaturation conditions in which crystal growth is initiated, growth is expected to occur through a **spiral growth** mechanism. This hypothesis is evidenced by the AFM images shown in figure 42 (p. 52).

5.4 Post-synthesis treatment of needle-shaped MER samples

5.4.1 Alkaline treatment

AFM images of the surface of the needle-shaped MER crystals after exposure to a 0.5 M NaOH alkaline solution are provided in figure 46. The treatment proved too severe as the previously observed spiral patterns (Figure 42, p. 52) have completely dissolved. The crystal surface is now covered with lumps of what appears to be a second phase. This would mean that dissolution of MER resulted in the formation of a new precursor mixture which then recrystallized on the surface of the treated MER crystals at 85 °C. Additional analysis with high-resolution XRD should be carried out in order to identify this new phase. Moreover, XRD analysis should reveal the extent of the damage done to the MER structure as a result of the treatment. Because of the very low yield of the experiment however, it was not possible to collect a sufficient amount of sample to perform the analyses on. Characterization of the remaining liquid phase by ICP should provide important information about its chemical composition. The supernatant is expected to be enriched in silicate species as the treatment was intended to de-silicate the MER sample.

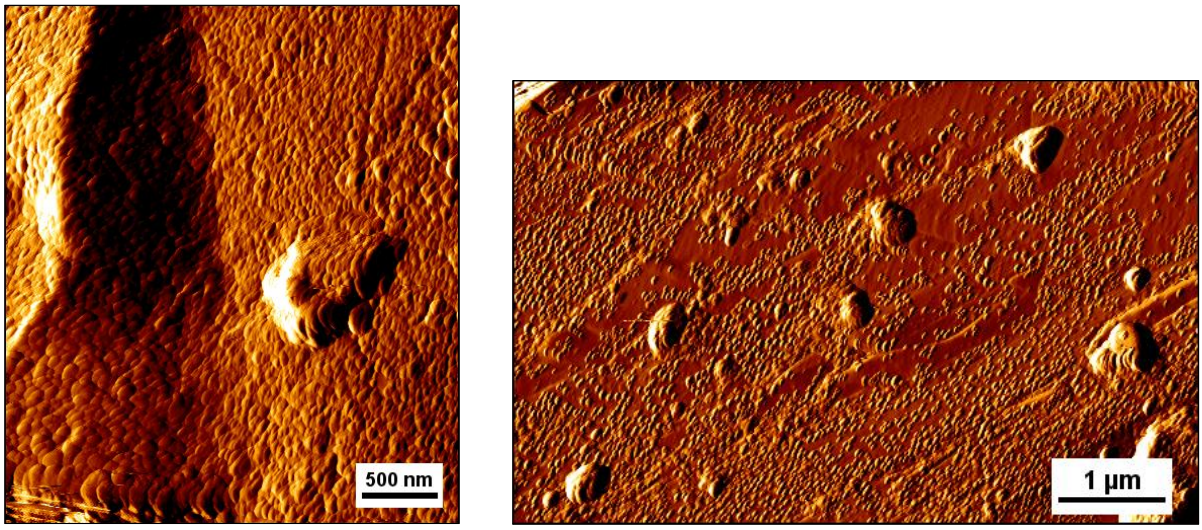

Figure 46. *Cm-AFM vertical deflection images of MER surface after treatment with a 0.5 M NaOH solution. The spiral patterns previously observed have completely been dissolved and have been replaced by lumps of what appears to be a second phase.*

5.4.2 Acid treatment

The surface of the needle-shaped MER crystals after treatment with a 0.5 M $HClO_4$ acidic solution has been imaged with cm-AFM (Figure 47a). The spiral patterns previously observed have again completely dissolved. The crystal surface is now covered with large craters and holes. Similar to the alkaline treatment, small lumps of a potential second phase have formed on the surface, albeit less abundantly than in figure 42 (p. 52). More importantly however, dissolution of MER in acid conditions has exposed screw dislocations on the crystal surface. Height analysis of the cross-section highlighted in figure 47b reveals that the average step height of that dislocation amounts to 8.0 ± 0.2 nm (Figure 48). This result suggests that the analyzed screw dislocation can be at the origin of one of the spiral patterns observed *prior* to acid treatment as the height is a multiple of 0.6 ± 0.1 nm. Additional XRD analysis should be carried out to identify the different crystalline phases present in the solids mixture and to determine the structural damage done to the MER crystals as a result of the acid treatment. It was however not possible to collect a sufficient amount of sample as the yield of the experiment was very low.

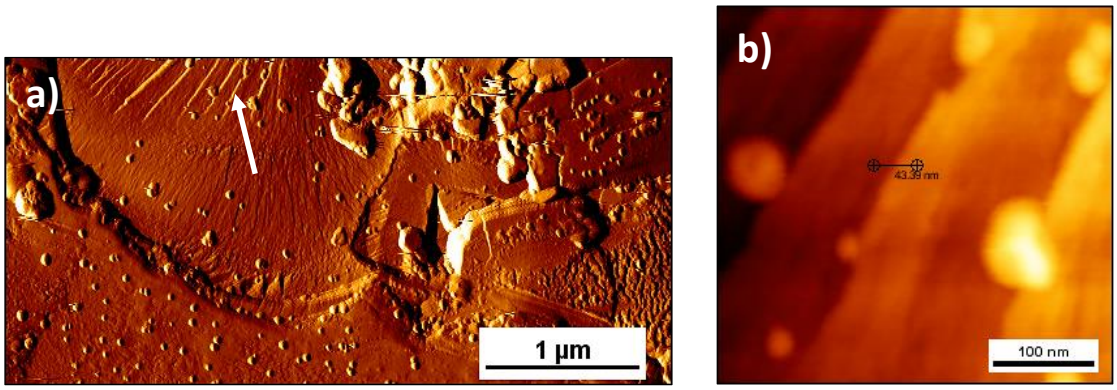

Figure 47. *a) Cm-AFM vertical deflection image of MER surface after exposure to a 0.5 M perchloric acid solution. The spiral patterns previously observed on the needle-shaped MER crystals has completely been dissolved and replaced by large holes and craters. b) Cm-AFM height image of the screw dislocation highlighted in figure 47a (enlarged view).*

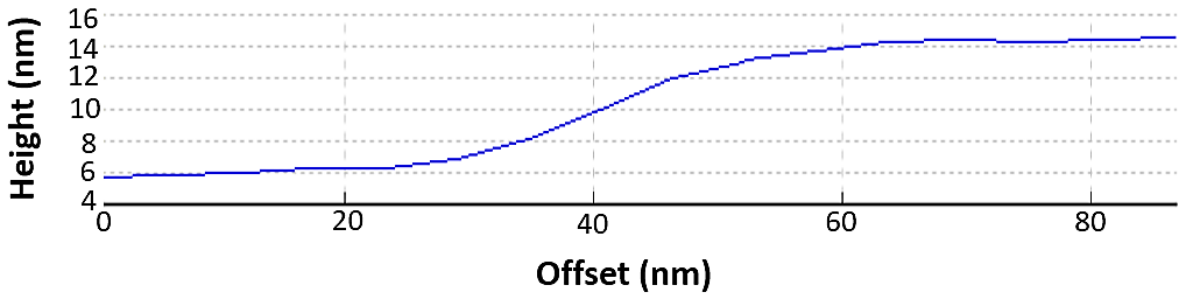

Figure 48. *Height profile along the line segment drawn in figure 47b. The average step height of the screw dislocation amounts to 8.0 ± 0.2 nm.*

Chapter 6: UTL and -COK-14

6.1 Growth of UTL

Shape and size of AS UTL were determined by SEM (Figure 49). The SEM images show the occurrence of rather large particles with sheet-like crystal morphology. The surface of these particles was also imaged by cm-AFM (Figure 50). The vertical deflection images further demonstrate the extensive presence of terraces with clearly discernable steps on the crystal surface. Additional AFM images are provided in Appendix E. These surface features are characteristic of a **'birth and spread'** growth mechanism, which typically occurs in high supersaturation conditions. Height analysis of the terrace steps resulted in an average height of 1.5 ± 0.1 nm (Figure 51). This result is in accordance with step heights obtained by R. L. Smith *et al.* (2014), who carried out similar AFM analysis on AS UTL samples.[74] UTL has a monoclinic unit cell with parameters a = 2.89964 nm, b = 1.39679 nm, c = 1.24493 nm and α, β and γ equal to 90°, 104.91° and 90° respectively.[12] Interplanar distances d_{hkl} in a monoclinic unit cell are calculated with:

$$\frac{1}{d_{hkl}^2} = \frac{1}{sin^2\,\beta}\left(\frac{h^2}{a^2} + \frac{k^2\,sin^2\,\beta}{b^2} + \frac{l^2}{c^2} - \frac{2\,h\,l\cos\beta}{a\,c}\right)$$

where h, k and l are the Miller indices of a plane in the crystal lattice and a, b, c, α, β and γ refer to the unit cell parameters. Using the (*hkl*) = (200) reflection (Figure 54, p. 62), the distance between two successive silicate layers is obtained, which also corresponds to the height of one UTL monolayer. This calculation yields a value of d_{200} = 1.44 nm, which is equal to half the length of the unit cell in the a-direction. As the average step height of 1.5 ± 0.1 nm matches the value of the d_{200}-spacing, the terraces are concluded to consist of UTL monolayers which grow on the (100) face.

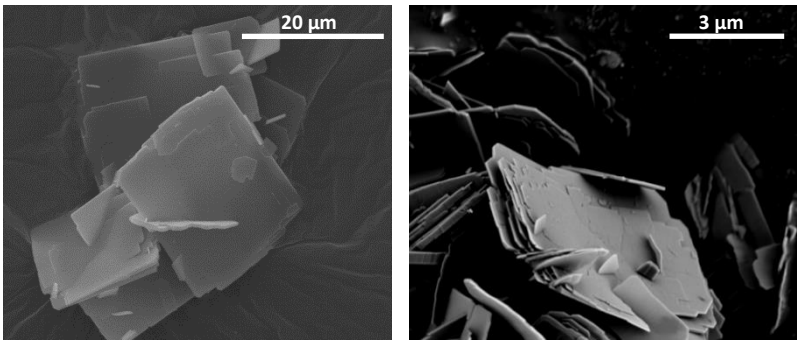

Figure 49. *a) SEM image of AS UTL crystals with sheet-like morphology. b) High-resolution SEM image demonstrating the layered structure of UTL.*

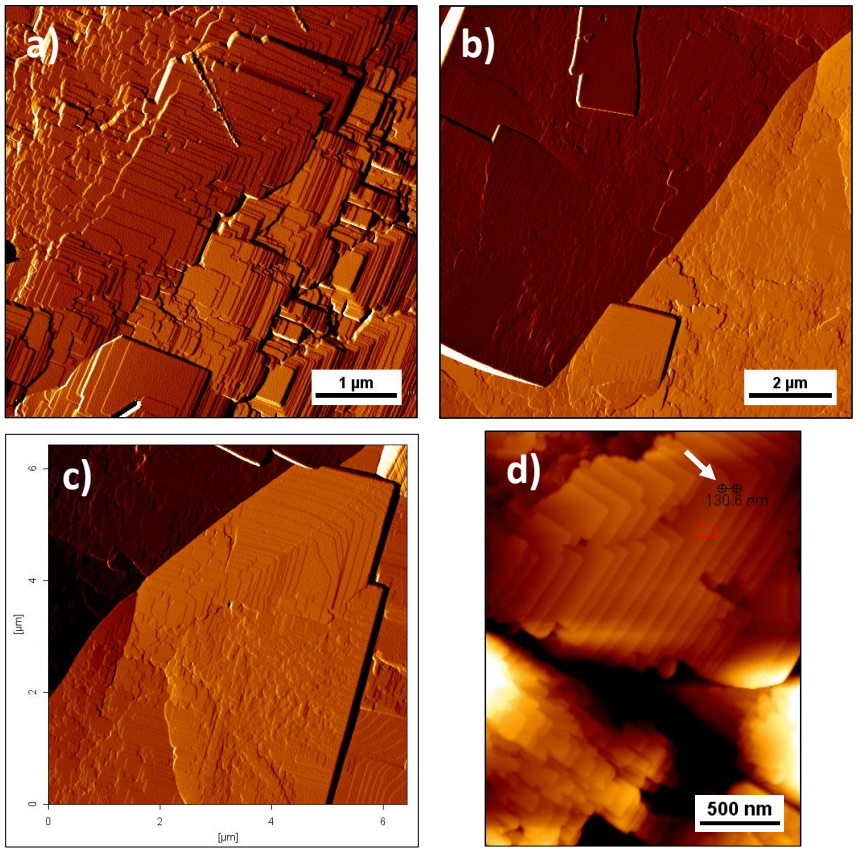

Figure 50. *a,b,c) Cm-AFM vertical deflection images of AS UTL. The surface is fully covered with terraces which demonstrate pyramidal patterns. d) Cm-AFM height image of the crystal surface. The cross-section used for step height analysis is highlighted as well as the area used to generate the histogram (red rectangle).*

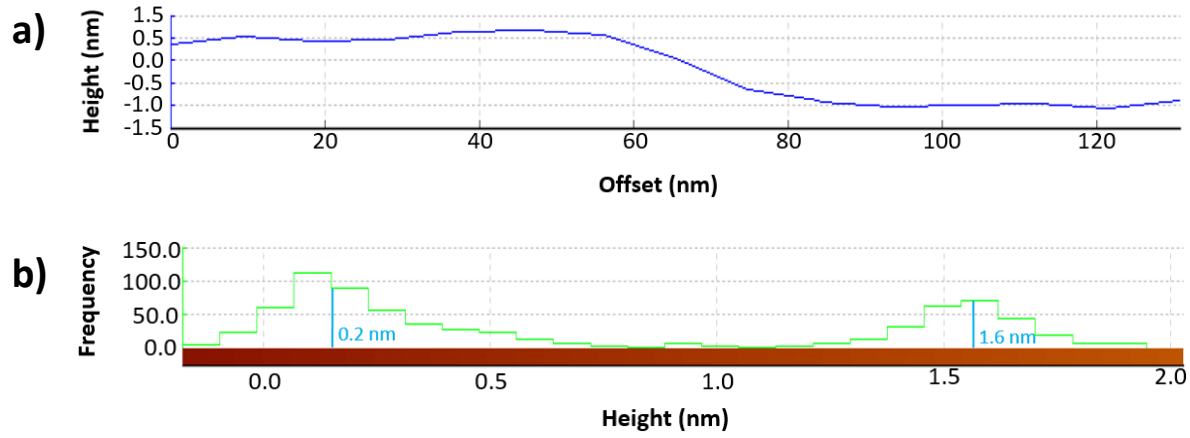

Figure 51. *a) Height profile along the line segment in figure 50d. The average step height of the terrace amounts to 1.5 nm. b) Histogram of area enclosed in the red rectangle highlighted in figure 50d. An average step height of 1.4 nm is obtained by taking into account the average height of the lower and upper terraces, which are depicted in blue.*

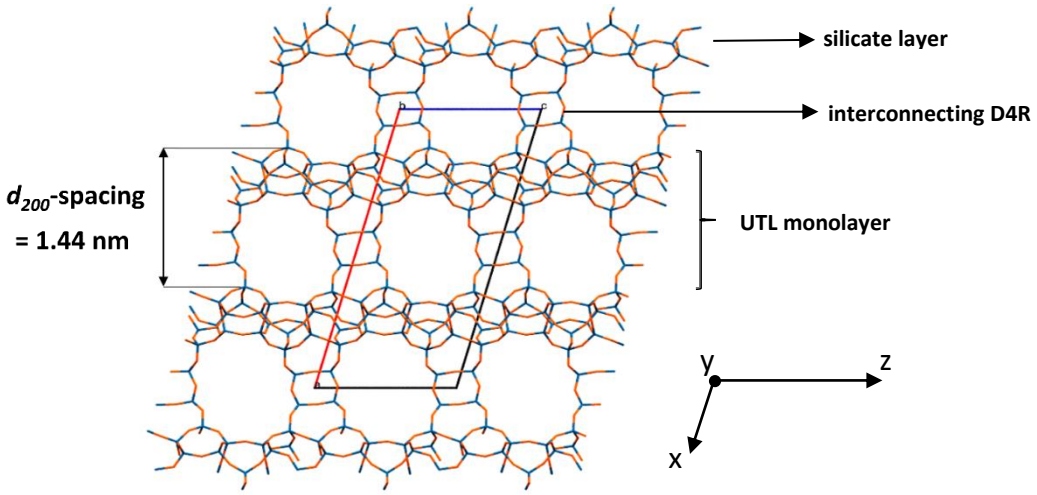

Figure 52. *Schematic illustration of the layered UTL framework structure. O atoms are represented in orange, the tetrahedrally coordinated Si- or Ge-atoms in blue. The vertical distance between two successive silicate layers, which corresponds to the d_{200}-spacing and the height of one UTL monolayer, is highlighted and amounts to 1.44 nm. This value is equal to half the length of the UTL unit cell in the a-direction. The monoclinic shape of the unit cell is illustrated as well.*

6.2 Ball milled as-synthesized UTL

The ball milling treatment proved effective in reducing the size of the treated particles, as evidenced by SEM imaging (Figure 53). Average particle size is smaller and crystal morphology less defined in comparison with the untreated AS UTL crystals depicted in figure 49a (p. 59). Moreover, this result was achieved with a limited loss of crystallinity. The XRD pattern of a ball milled (BM) AS UTL sample shows limited decrease in reflection intensity compared to untreated AS UTL samples (Figure 54). This observation is in agreement with previous results obtained by K. Akçay *et al.* (2004), who treated zeolite HY in similar conditions. These researchers argued that the presence of a solvent is key in limiting crystallinity losses.[75]

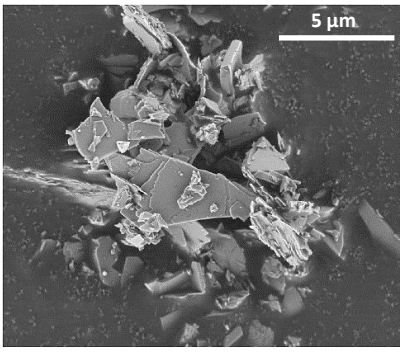

Figure 53. *SEM image of ball milled AS UTL sample.*

BM AS UTL was also characterized with 'tapping-mode' AFM. A 3D rendering of the surface and its features is shown in figure 55 and was constructed by combining phase and height data from the AFM experiment. The milling process has led to the deposition of a significant amount of debris on the UTL surface. In addition, the treatment resulted in the creation of small holes and 'scratches'. As small particles can attach to the glass milling balls, they damage the surface of larger UTL crystals upon impact, generating small holes which further increase the available surface area.

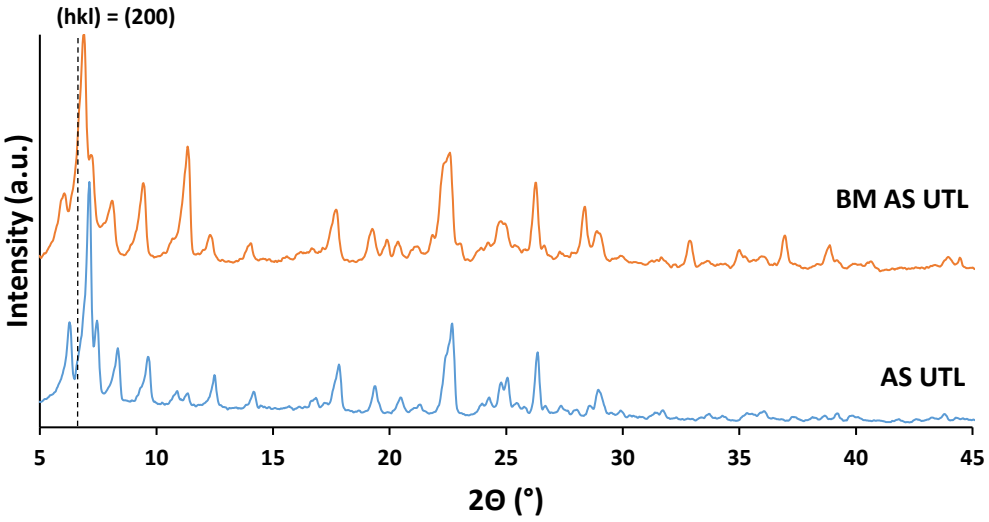

Figure 54. *XRD patterns of AS UTL and BM AS UTL. The (hkl) = (200) reflection used to determine the distance between two successive silicate layers (= d_{200}-spacing) is highlighted with a dotted line.*

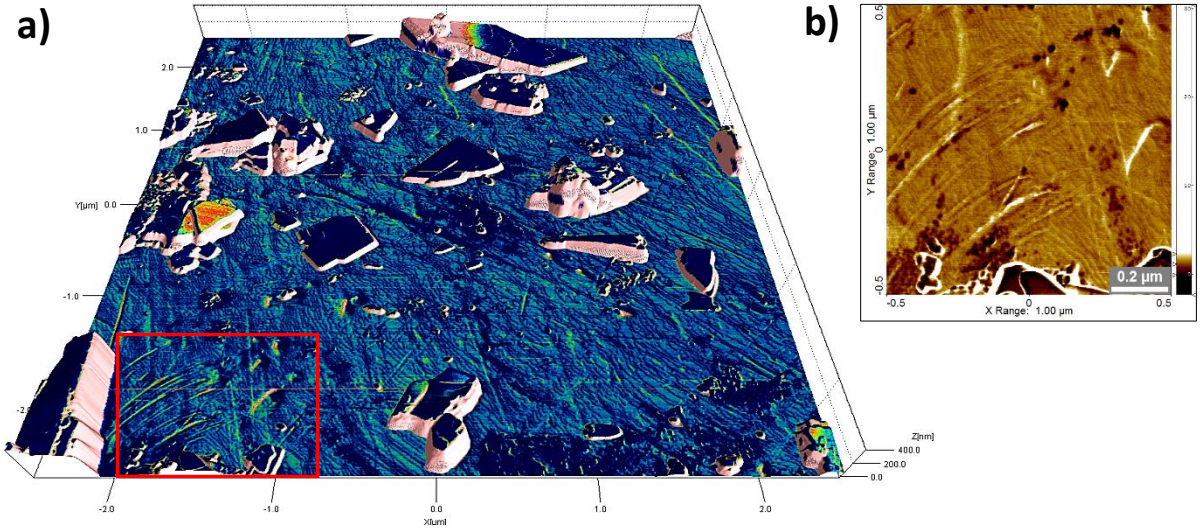

Figure 55. *a) 3D representation of the AS UTL surface after ball milling, obtained by combining phase and height data acquired in 'tapping-mode' AFM. The image clearly demonstrates the presence of debris on top of the terrace-covered surface. b) Enlarged phase image of the area contained in the red rectangle in (a). Small holes and 'scratches' have been formed on the surface as a result of the ball milling treatment.*

6.3 As-synthesized UTL treated with pestle

AS UTL was manually treated with a pestle and characterized by means of SEM (Figure 56) and cm-AFM (Figure 57). The average particle size has decreased compared to untreated samples and the once terrace-rich AS UTL surface (Figure 50a, p. 60) has been completely levelled out by the treatment. It was not expected that a macroscopically applied force would have such an effect on a microscopic level. The particulate matter deposited on the manually treated (MT) AS UTL surface appears to be debris. However, it is also possible these particulates (partly) consist of template molecules, as the zeolite has not been calcined prior to treatment. The presence of 'cracks' on the surface also indicates a starting delamination as a result of the tangentially applied pressure. Detachment of layers from the parent material by delamination is another potential method to increase the available surface area. Similar the ball milling, these results were achieved with a limited loss of crystallinity, as evidenced by the XRD patterns provided in figure 58.

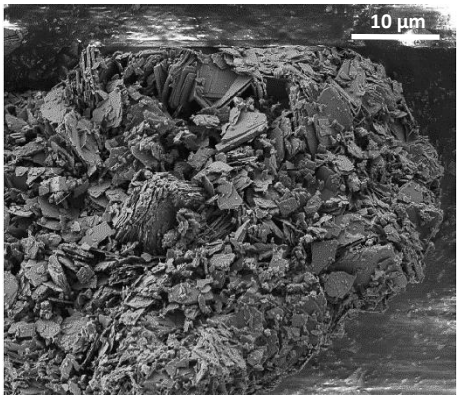

***Figure 56**. SEM image of MT AS UTL sample: particle size is much smaller with respect to untreated AS UTL.*

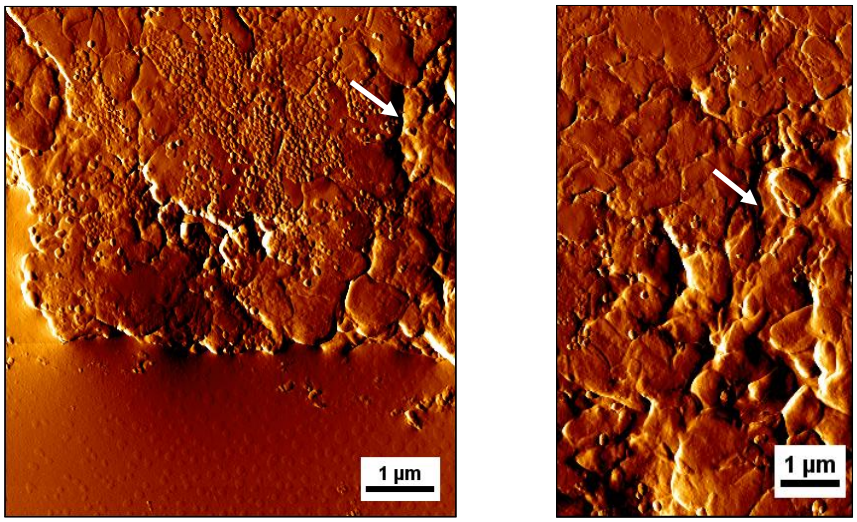

***Figure 57.** Cm-AFM vertical deflection images of the AS UTL surface after treatment with a pestle. The once terrace-rich surface has been completely levelled out and is now covered with particulate matter. 'Cracks' in the surface are highlighted by white arrows and indicate a starting delamination of the layered UTL sample.*

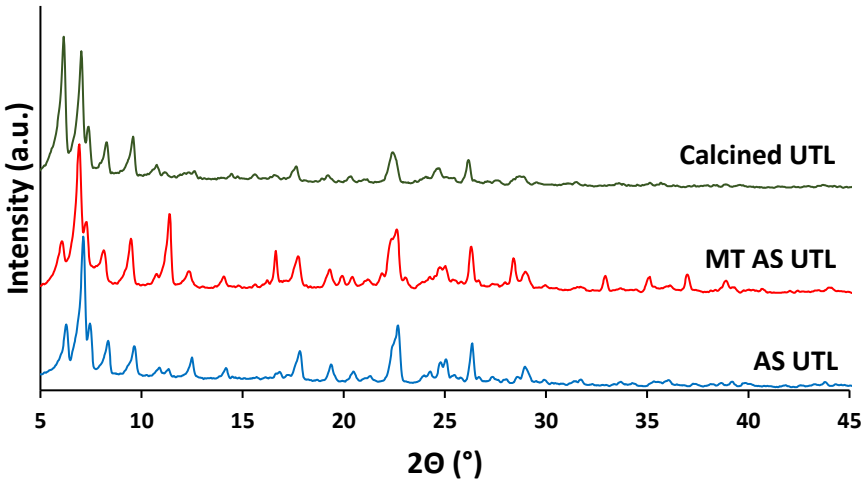

Figure 58. *XRD patterns of AS UTL, MT AS UTL and Calcined UTL. A clear difference is observed for calcined UTL and AS UTL, which can be attributed to the collapse of the UTL framework structure upon removal of the SDAs by calcination.*

6.4 Surface characterization of calcined UTL

Cm-AFM images of the surface of a calcined UTL sample demonstrate an increased surface roughness (Figure 59). The remaining terraces are not as clearly defined as for AS UTL (Figure 50, p. 60). As elaborated in section 1.5, the UTL framework structure becomes unstable upon calcination and accompanied removal of the SDAs. The resulting structural collapse is responsible for the perceived changes in surface features and is exemplified by the XRD patterns provided in figure 58. The fact that some terraces remain visible, can point towards an incomplete calcination protocol. Determination of the average step height proved difficult because of the rough surface, but the few obtained heights were comparable to the values for AS UTL (Figure 60).

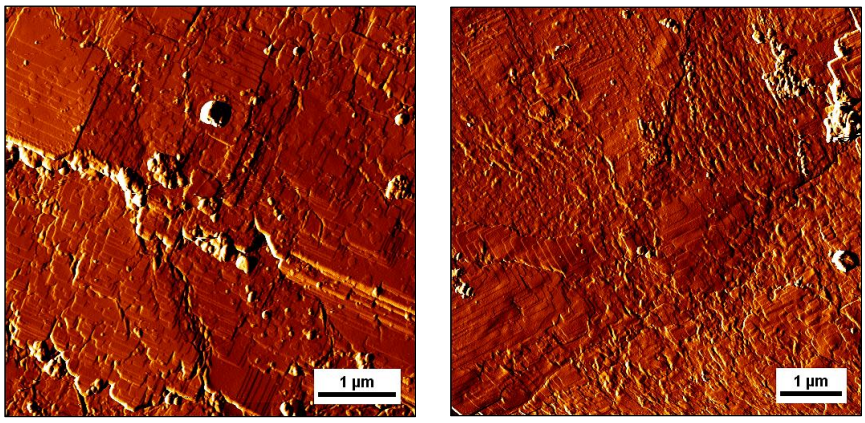

Figure 59. *Cm-AFM vertical deflection images of calcined UTL. The surface is rough and the terraces are less well-defined compared to AS UTL. The amorphous lumps on top of the surface can consist of template molecules which were not removed by washing.*

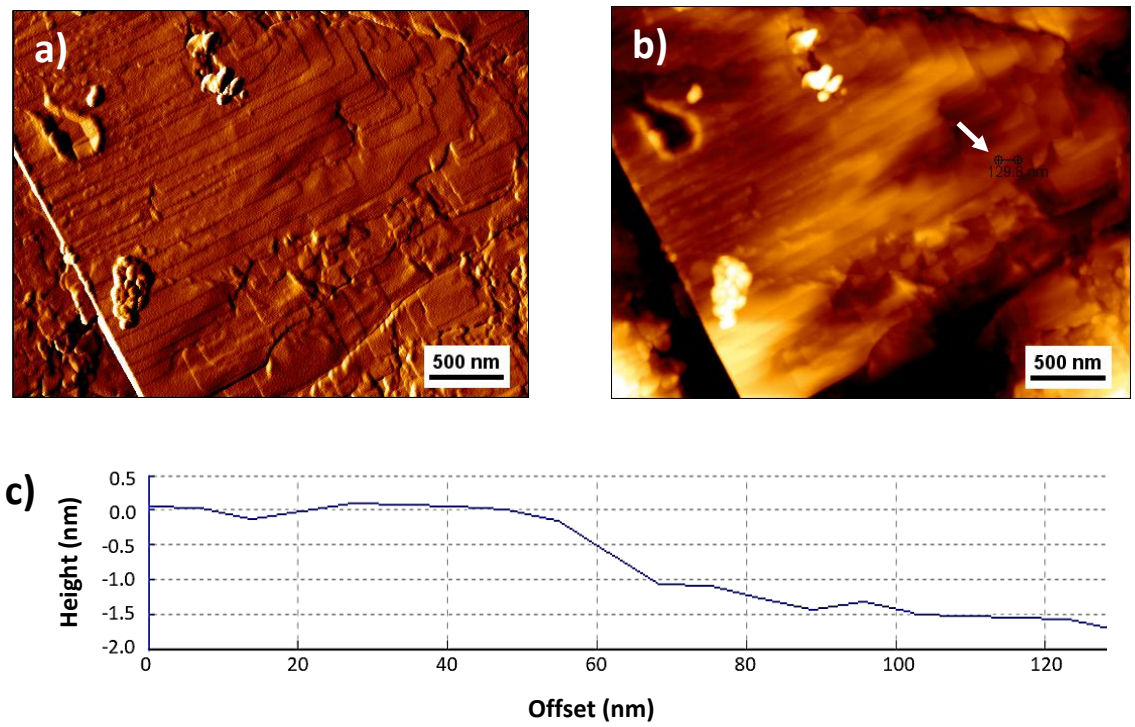

Figure 60. *a) Cm-AFM vertical deflection image of calcined UTL surface (enlarged view). b) Corresponding cm-AFM height image of figure 60a. c) Height profile of the cross-section in figure 60b, indicating the average terrace step height amounts to 1.5 nm.*

6.5 Surface characterization of -COK-14

-COK-14 was analyzed by SEM (Figure 61) and cm-AFM (Figure 62). Additional cm-AFM images are presented in Appendix F. Similar to AS UTL (Figure 50, p. 60), -COK-14 crystals have a sheet-like morphology and their surface is covered with terraces, albeit less extensively. Average terrace step height, determined by cross-sectional height analysis, amounted to 1.2 ± 0.1 nm (Figure 62e). Although -COK-14 does not possess a fully connected OKO framework structure, its unit cell dimensions are approximated by unit cell parameters specific to OKO. The OKO framework structure has a monoclinic unit cell with dimensions a = 2.40638 nm, b = 1.38332 nm, c = 1.23516 nm and α, β and γ equal to 90°, 109.128° and 90° respectively.[12] Analogously to UTL, the height of an OKO monolayer was determined by using the (200) reflection and yielded a value of d_{200} = 1.14 nm (Figure 63, p. 67). A decrease of 0.30 nm with respect to the d_{200}-spacing for UTL was expected, as transformation of the UTL parent material to -COK-14 essentially comes down to the removal of Ge-S4Rs from the D4Rs connecting the silicate layers (Figure 11, p. 14). L. I. Meza *et al.* (2007) have also demonstrated that removal of a S4R lowers the average terrace step height by 0.30 nm.[62]

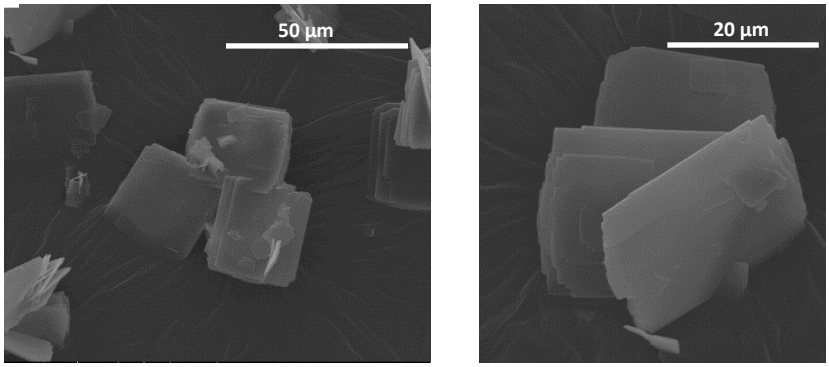

Figure 61. *SEM images of -COK-14 samples, demonstrating the sheet-like morphology of the crystals.*

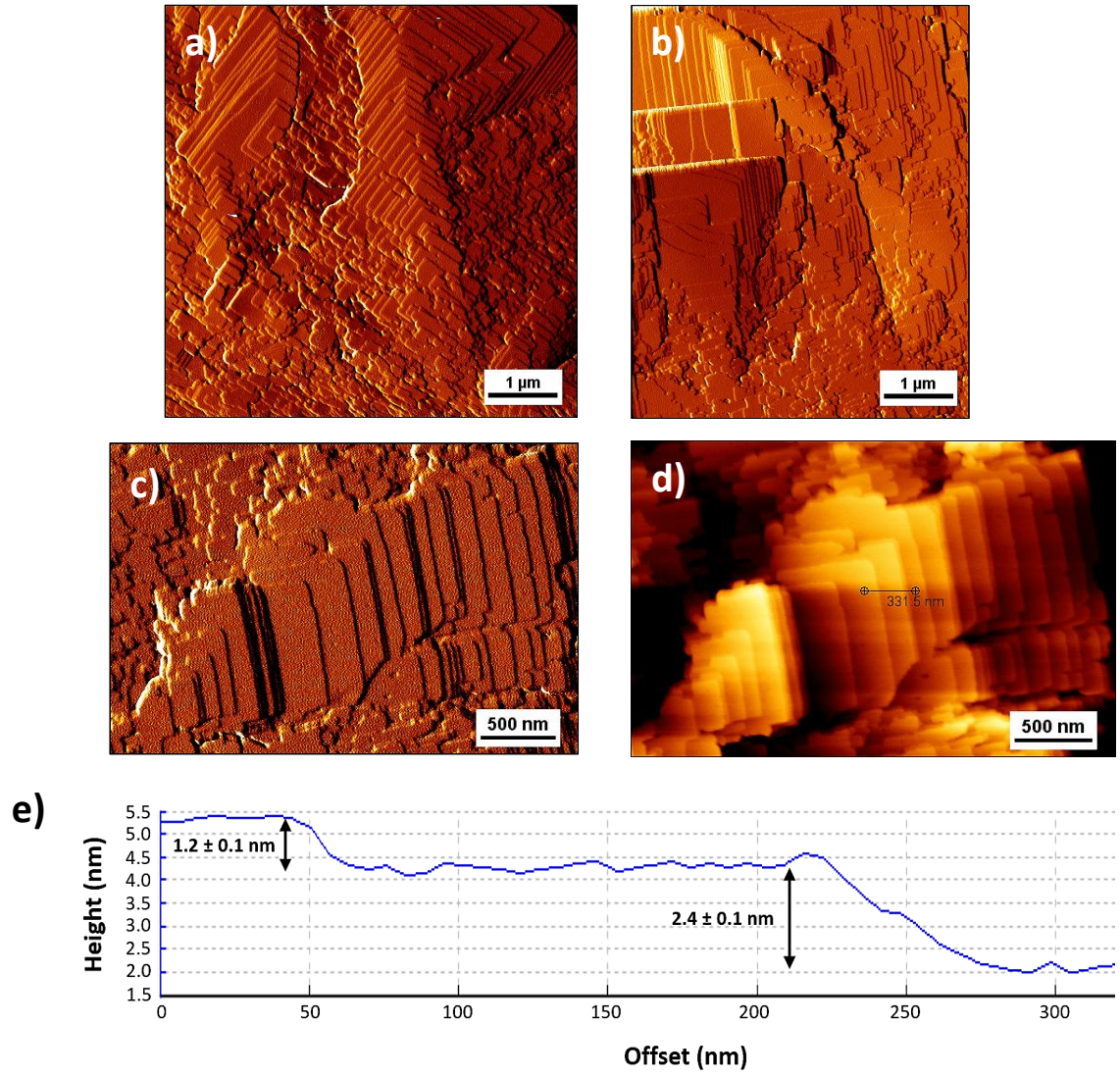

Figure 62. *a-c) Cm-AFM vertical deflection images of the terrace-rich -COK-14 surface. d) Corresponding cm-AFM height image of figure 62c. e) Accompanying height profile of the cross-section in figure 62d. The average step height of a single terrace equals 1.2 ± 0.1 nm and 2.4 ± 0.1 nm for double terraces.*

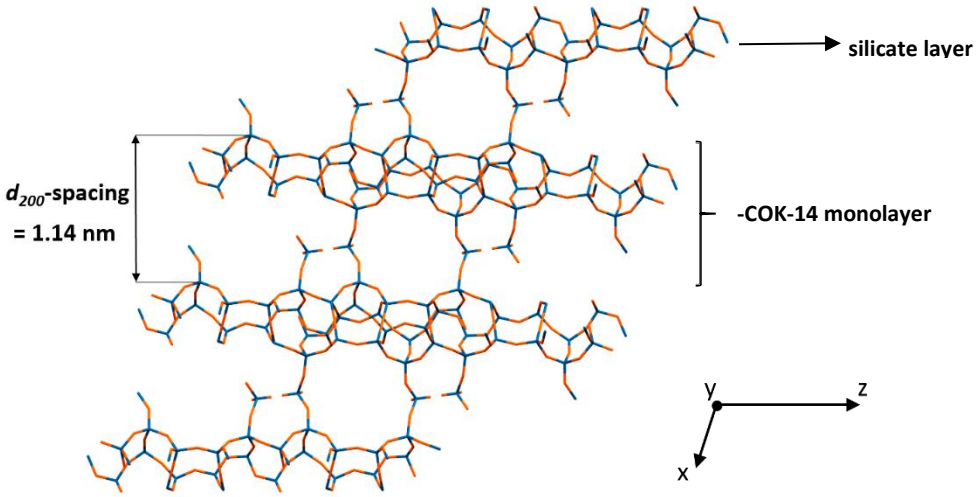

Figure 63. *Schematic illustration of the interrupted framework of the pure-silica -COK-14. O atoms are represented in orange, the tetrahedrally coordinated Si-atoms in blue. Absence of the interconnecting D4Rs shown in figure 52 (p. 61) is clearly observable. Removal of the Ge-S4Rs results in a 0.3 nm decrease of the d_{200}-spacing and -COK-14 monolayer height compared to the AS UTL framework structure (Figure 52, p. 61).*

Some -COK-14 crystals exhibited unexpected 'lumps' on their surface, which are exemplified in the AFM images in Figure 64. ICP analysis was carried out to determine the Ge-content of the sample and to verify whether the 'lumps' could consist of reprecipitated germanium oxide (GeO_4). Ge was only detected in trace amounts (0.7 wt%) however, ruling out this GeO_4 hypothesis. Height profiling with cm-AFM revealed that the average height of the 'lumps' amounts to 1.2 nm ± 0.2 nm (Figure 65), which corresponds to the average terrace step height of -COK-14 (Figure 62e). This result suggests the imaged 'lumps' are in fact 2D nuclei which are at the basis of **layer growth** and '**birth and spread**' **growth mechanisms**, as explained in section 2.2.

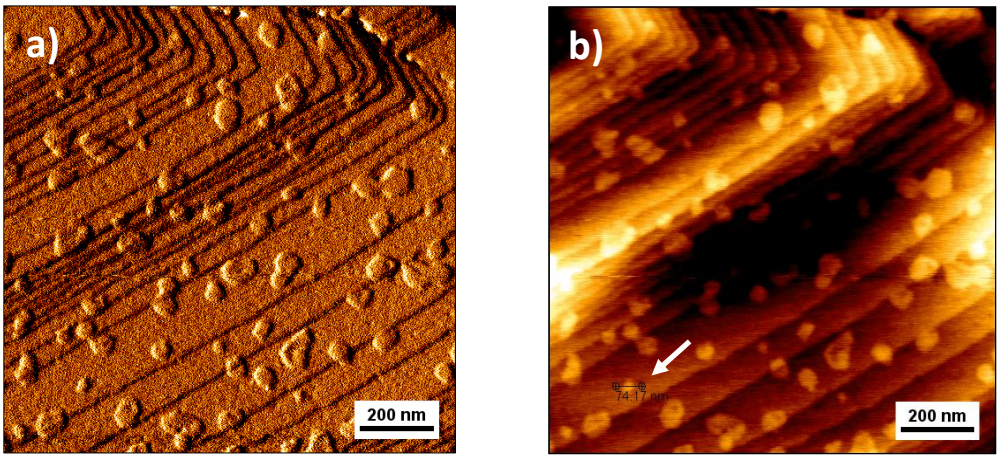

Figure 64. *a) Cm-AFM vertical deflection image of -COK-14 showing 'lumps' on the surface. b) Accompanying cm-AFM height image, with the cross-section used for height determination.*

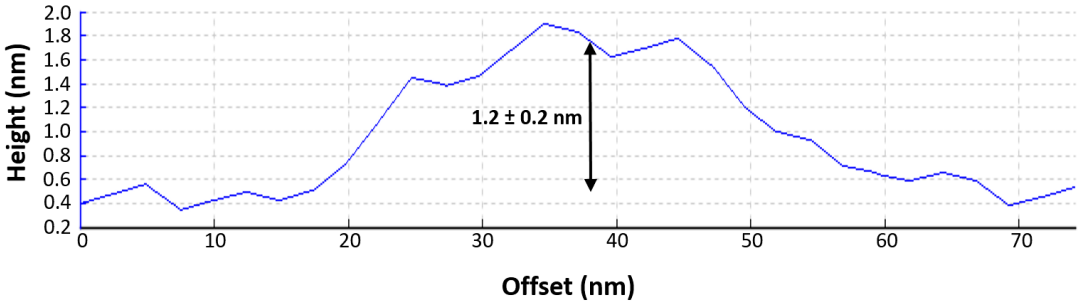

Figure 65. *Height profile of the line segment in figure 64b. The average height of the analyzed 'lump' amounts to 1.2 ± 0.2 nm, which corresponds to the terrace step height determined for -COK-14.*

6.6 Ball milled -COK-14

The effects of ball milling with 2 mm and 5 mm ZrO_2 balls on the crystal dimensions was determined by SEM (Figure 66). These images show that treatment of -COK-14 with 2 mm milling balls for 1 hour resulted in the formation of larger particles compared to the particles collected after milling with larger ZrO_2 grinding balls for 24 hours. This observation may seem counter-intuitive, but K. Akçay *et al.* (2004) have reported similar results.[75] By varying the size of the grinding balls and the time span of the ball milling treatment of zeolite HY, these researchers found that short milling times (< 2 hours) and small milling balls (2 mm) resulted in the formation of larger particles than the ones obtained with 3 mm milling balls. Longer milling times (≥ 10 hours) ultimately led to the formation of particles with approximately the same size, independent of the dimensions of the milling balls.[75] The SEM images also highlight another important difference between the ball milled samples: the -COK-14 crystals treated with 5 mm milling balls exhibit a large amount of holes in comparison to the sample milled with 2 mm grindings balls.

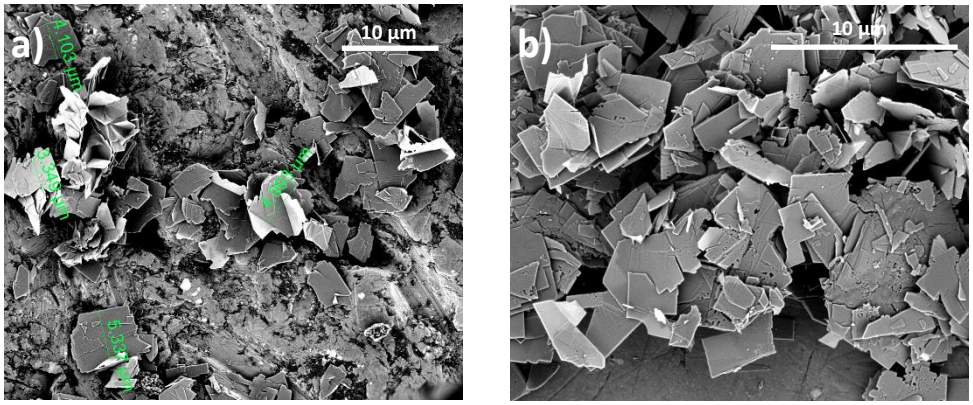

Figure 66. *a) SEM image of -COK-14 crystals after ball milling treatment with 2 mm ZrO_2 balls for 1 hour. b) SEM image of -COK-14 sample milled with 5 mm ZrO_2 balls for 24 hours. Longer treatment of -COK-14 with larger balls clearly results in the formation of smaller particles. Additionally, the surface of these crystals shows the presence of many holes.*

These findings were further substantiated by cm-AFM vertical deflection images (Figure 67). These images illustrate the previously observed size difference and validate the occurrence of large amounts of holes on the surface of -COK-14 treated with 5 mm milling balls. Moreover, figure 67a clearly demonstrates delamination of the layered -COK-14 as a result of the grinding treatment with 2 mm ZrO_2 balls. These observations can be rationalized by taking into account the dimensions of the resulting particles. The substantial surface area of the larger particles obtained with 2 mm milling balls leads to increased friction forces between the crystals as the surfaces contact each other during the procedure. This interaction predominantly results in delamination of the layered zeolite (Figure 67a). Conversely, the smaller particles formed by the milling treatment with 5 mm balls can more easily attach to the milling balls and damage the surface of other crystals upon impact. This damage leads to the extensive creation of holes on the surface. Ultimately, both procedures lead to an increased surface area as the average particle size decreases with respect to untreated samples and the crystalline structure is modified either by delamination or hole-formation. PXRD analysis of the treated solids could not be performed due to the limited amount of sample. Based on the results obtained for BM AS UTL however, loss of crystallinity of the -COK-14 sample treated for 1 hour with 2 mm milling balls is expected to be limited. Due to the long milling time (24 hours) on the other hand, expectations are that the crystalline structure of the -COK-14 sample treated with 5 mm will have changed significantly. For zeolite HY for instance, 45% of the crystallinity was lost after milling times greater than 10 hours, independent of the size of the grinding balls.[75]

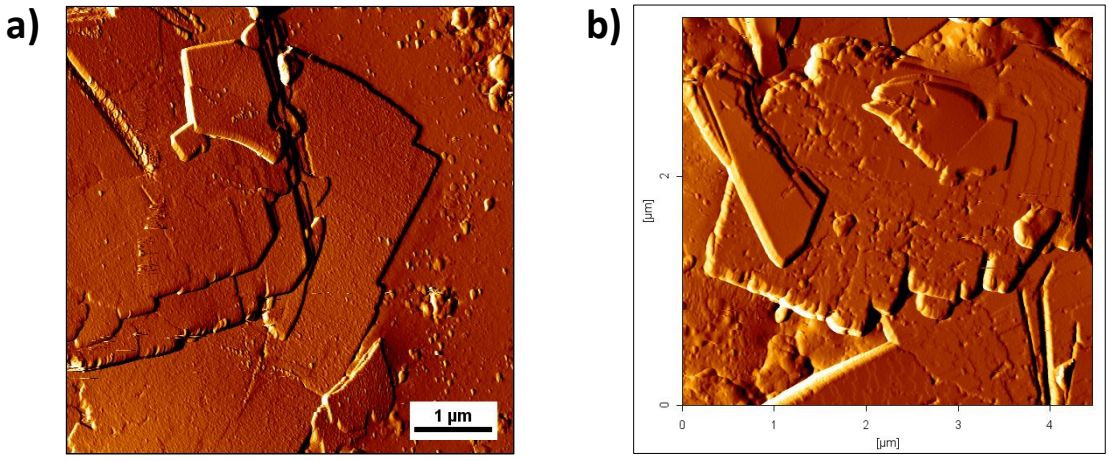

Figure 67. *a) Cm-AFM vertical deflection image of a -COK-14 sample subjected to a ball milling treatment with 2 mm ZrO_2 grinding balls for 1 hour. Delamination of the layered -COK-14 zeolite is clearly observable. b) Cm-AFM vertical deflection image of a ball milled -COK-14 sample. The treatment was carried out with 5 mm grinding balls for 24 hours. The dimensions of the resulting particles are smaller than the ones obtained for the procedure with 2 mm balls. The surface is scarred with a large amount of holes as a result of the milling treatment.*

Chapter 7: IWW

7.1 Surface characterization of IWW

Crystal size and morphology were determined by means of SEM (Figure 68), which revealed a cluster of small IWW crystals with plate-like morphology. Further characterization of the IWW surface was carried out by cm-AFM. Because of the heavily aggregated nature of the sample, imaging of the surface proved difficult. One of the few obtained images shows the occurrence of layer-like structures and excessive amounts of spherical 'lumps' superimposed on a very rough surface (Figure 69). These surface features are indicative of an **adhesive type** growth mechanism, which only occurs at very high supersaturation conditions. Because of the roughness of the IWW surface, no height information could be collected. Additional synthesis experiments need to be carried out in order to determine the most optimal conditions for IWW to grow. These conditions primarily involve the concentration of framework-forming elements in the synthesis mixture and the temperature, as these parameters are the predominant factors influencing supersaturation conditions during crystal growth. Based on the results obtained for MER, it is expected that higher temperatures and less concentrated precursor mixtures will favorably influence the growth of IWW as supersaturation decreases.

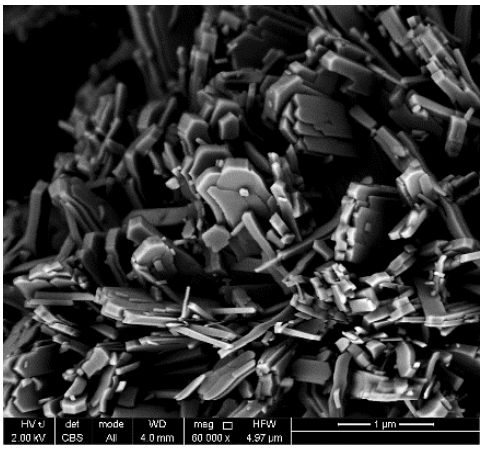

Figure 68. *SEM image of a cluster of small, plate-like IWW crystals.*

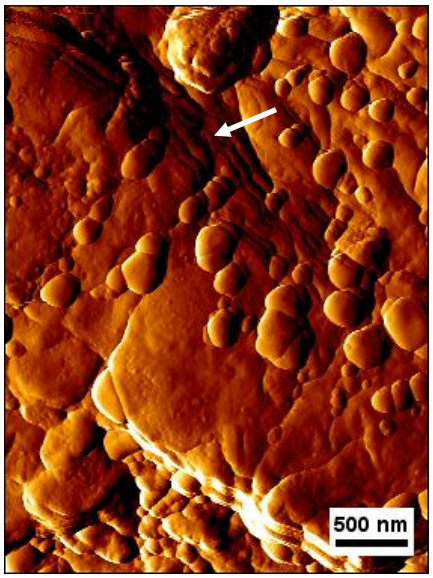

Figure 69. *Cm-AFM vertical deflection image of IWW surface, demonstrating the presence of layers (white arrow) and spherical 'lumps' covering the surface.*

Chapter 8: Conclusion

In this work, the surfaces of several zeolite structures were successfully characterized by means of AFM. By identifying and quantifying distinct features on the crystal surface, a hypothesis was formulated about the prevailing growth mechanisms. Furthermore, mechanical treatment was carried out on several crystalline samples in an attempt to increase the available surface area without compromising on crystallinity. These samples were imaged by cm-AFM before and after treatment in order to determine the extent of the damage to the surface as a result of the treatment.

Growth of MER synthesized at 90 °C for 28 days occurred through a 'birth and spread' mechanism and was evidenced by the corresponding cm-AFM vertical deflection images. Synthesis of MER from the same precursor mixture but at 170 °C however, yielded needle-shaped crystals with spiral patterns superimposed on the surface, indicating crystal formation took place through 'spiral growth'. The average step height of a single spiral terrace averaged at 0.6 ± 0.1 nm, which corresponded to half the length of the MER unit cell in a- and b-directions. The distinction in MER growth mechanisms was attributed to differences in supersaturation conditions during crystal growth initiation. Liquid state NMR-analysis of the supernatant solution collected after 2, 4, 8, 16, 32 and 48 hours of synthesis at different temperatures (90, 150 and 175 °C) revealed supersaturation increases with decreasing temperature. Alkaline and acid treatment of needle-shaped MER samples resulted in complete dissolution of the previously observed spiral patterns, as exemplified by the vertical deflection images. In addition, exposure to the alkaline solution led to the deposition of what appears to be a second phase on the crystalline surface. Acid treatment of MER on the other hand exposed the presence of screw dislocations which could be at the origin of the spirals observed on the MER surface after synthesis at 90 °C.

Characterization of AS UTL with cm-AFM indicated crystal growth occurred via a 'birth and spread' mechanism. Average terrace step height amounted to 1.5 ± 0.1 nm and corresponded to step heights described in the literature. As the measured step height matched the d_{200}-spacing, the terraces were concluded to consist of UTL monolayers growing on the (100) face. Calcination of AS UTL led to an observable increase of the surface roughness. This observation could be attributed to the structural collapse associated with removal of the SDAs from the framework structure. Transformation of UTL to -COK-14 resulted in a 0.3 nm decrease of the average step height as a result of the removal of the Ge-S4Rs, which was expected based on previous findings by L. I. Meza *et al.* (2007).

Ball milling experiments carried out on AS UTL succeeded in reducing the average particle size with minimal loss of crystallinity. A 3D representation of the treated AS UTL surface, which was constructed from data obtained in 'tapping-mode' AFM, also indicated the formation of holes and 'scratches' as a result of the procedure. Treatment of AS UTL with a pestle yielded similar results, the main difference being that the surface of the treated crystals had been completely levelled out and exhibited a starting delamination. Ball milling performed on -COK-14 with ZrO_2 grinding balls of different sizes indicated that the combination of short milling times (1 hour) and smaller grinding balls (2 mm) favored the formation of larger particles with respect to longer treatments (24 hours) and larger milling balls (5 mm). Moreover, the structure of the larger particles demonstrated extensive delamination after the treatment, whereas the surface of the smaller particles was covered with holes instead. This observation could be rationalized by considering the size of the resulting particles. The substantial surface area of larger particles obtained with the 2 mm grinding treatment, led to the emergence of significant friction forces between contacting crystal surfaces, resulting mainly in delamination. Smaller particles on the other hand could more easily attach to the milling balls and perforate the surface of other crystals upon impact, hence damaging the surface and creating numerous holes.

Characterization of IWW revealed the occurrence of layer-like structures and excessive amounts of spherical 'lumps' superimposed on a very rough surface. Such surface features are characteristic of an 'adhesive type' growth, a growth mechanism which typically occurs at very high supersaturation conditions. Additional synthesis experiments, focusing primarily on the composition of the precursor mixture and the temperature, need to be carried out in order to determine the most optimal conditions for IWW to grow. Based on the results obtained for MER, growth of IWW is expected to occur at lower supersaturation conditions when higher temperatures and less concentrated precursor mixtures are employed.

Chapter 9: Outlook

This work focused on the *ex situ* characterization of zeolite structures. Samples were prepared, treated, dried and then analyzed by AFM. More accurate information about the growth mechanism of these zeolite structures could however be obtained by imaging the growth process *in situ*. It is known that zeolites only crystallize at appreciable rates at elevated temperatures. Most AFM set-ups are not equipped to handle such temperatures, making it virtually impossible to follow zeolite growth in real-time. This limitation could be circumvented by exploiting the 'seeding effect' observed during MER synthesis. The presence of a number of stable nuclei significantly increases the crystallization rate, theoretically allowing crystal growth to proceed at lower temperatures (50-70 °C). Optimization of flow rates and composition of the precursor mixture should be performed prior to implementation, but the possibilities of this procedure are real.

Alternatively, additional information about the occurrence and stability of certain building units could be obtained by carrying out dissolution experiments similar to the ones performed by R. Brent *et al.* (2008). In this work, an attempt was made to visualize the effect of alkaline and acid treatments on the surface structure of needle-shaped MER crystals *ex situ*. However, the concentration of these solutions proved too high and the previously observed spiral patterns dissolved completely after 4 hours. Better results could be acquired by reducing the length of the treatment or, more importantly, by reducing the concentration of the solutions. Alternatively, an *in situ* experimental set-up would allow real-time imaging of the dissolution process, as demonstrated by L. I. Meza *et al.* (2007). Analogously to the procedure described in the previous paragraph, flow rates and chemical composition of the precursor mixture should be optimized prior to realization as to obtain the clearest images possible.

Bibliography

[1] B. Yilmaz and U. Muller, “Catalytic applications of zeolites in chemical industry,” *Top. Catal.*, vol. 52, no. 6–7, pp. 888–895, 2009.

[2] C. S. Cundy and P. a Cox, “The Hydrothermal Synthesis of Zeolites : History and Development from the Earliest Days to the Present Time,” *Chem. Rev.*, vol. 103, no. February, pp. 663–702, 2003.

[3] J. Weitkamp, “Zeolites and catalysis,” *Solid State Ionics*, vol. 131, no. 1, pp. 175–188, 2000.

[4] P. A. Wright and M. Lozinska, “Structural Chemistry and Properties of Zeolites,” in *Zeolites and Ordered Porous Solids: Fundamentals and Applications*, 2011, pp. 1–36.

[5] G. Bellussi and V. Fattore, “Isomorphous Substitution in Zeolites: A Route for the Preparation of Novel Catalysts,” *Stud. Surf. Sci. Catal.*, vol. 69, pp. 79–92, 1991.

[6] E. Polat, M. Karaca, H. Demir, and a N. Onus, “Use of natural zeolite (clinoptilolite) in agriculture,” *J. Fruit Ornam. Plant Reserarch*, vol. 12, pp. 183–189, 2004.

[7] S. Wang and Y. Peng, “Natural zeolites as effective adsorbents in water and wastewater treatment,” *Chem. Eng. J.*, vol. 156, no. 1, pp. 11–24, 2010.

[8] S. Ozaydin, G. Kocer, and A. Hepbasli, “Natural Zeolites in Energy Applications,” *Energy Sources, Part A Recover. Util. Environ. Eff.*, vol. 28, no. 15, pp. 1425–1431, Nov. 2006.

[9] Grand View Research, “Zeolite Molecular Sieve Market Analysis By Application (Detergents, Catalysts) And Segment Forecasts To 2022,” 2015. [Online]. Available: http://www.grandviewresearch.com/industry-analysis/synthetic-zeolite-market.

[10] Grand View Research, “Zeolite Molecular Sieve Market By Application (Detergents, Catalysts) Is Expected To Reach $4.27 Billion By 2022: New Report By Grand View Research, Inc.,” 2015. [Online]. Available: https://globenewswire.com/news- release/2015/06/29/748254/ 10140056/en/Zeolite-Molecular-Sieve-Market-By-Application-Detergents-Catalysts-Is-Expected-To-Reach-4-27-Billion-By-2022-New-Report-By-Grand-View-Research-Inc.html.

[11] A. R. Loiola, J. C. R. A. Andrade, J. M. Sasaki, and L. R. D. da Silva, “Structural analysis of zeolite NaA synthesized by a cost-effective hydrothermal method using kaolin and its use as water softener.,” *J. Colloid Interface Sci.*, vol. 367, no. 1, pp. 34–9, Feb. 2012.

[12] International Zeolite Association, “Database of Zeolite Structures.” [Online]. Available: http://www.iza-structure.org/databases/.

[13] C. Baerlocher, L. B. McCusker, and D. H. Olson, *Atlas of Zeolite Framework Types*, 6th ed. Amsterdam: Elsevier, 2007.

[14] T. F. Degnan, G. K. Chitnis, and P. H. Schipper, “History of ZSM-5 fluid catalytic cracking additive development at Mobil,” *Microporous Mesoporous Mater.*, vol. 35–36, pp. 245–252, 2000.

[15] C. J. Rhodes, “Properties and applications of zeolites,” *Sci. Prog.*, vol. 93, no. 3, pp. 223–284, 2010.

[16] E. R. Cooper, C. D. Andrews, P. S. Wheatley, P. B. Webb, P. Wormald, and R. E. Morris, "Ionic liquids and eutectic mixtures as solvent and template in synthesis of zeolite analogues.," *Nature*, vol. 430, no. 7003, pp. 1012–1016, 2004.

[17] E. R. Parnham and R. E. Morris, "Ionothermal Synthesis of Zeolites , Metal – Organic Frameworks , and Inorganic – Organic Hybrids," *Acc. Chem. Res.*, vol. 40, no. 10, pp. 1005–1013, 2007.

[18] P. Wasserscheid and W. Keim, "Ionic Liquids-New 'Solutions' for Transition Metal Catalysis.," *Angew. Chem. Int. Ed. Engl.*, vol. 39, no. 21, pp. 3772–3789, Nov. 2000.

[19] Y.-P. Xu, Z.-J. Tian, S.-J. Wang, Y. Hu, L. Wang, B.-C. Wang, Y.-C. Ma, L. Hou, J.-Y. Yu, and L.-W. Lin, "Microwave-enhanced ionothermal synthesis of aluminophosphate molecular sieves.," *Angew. Chem. Int. Ed. Engl.*, vol. 45, no. 24, pp. 3965–70, Jun. 2006.

[20] E. R. Parnham, E. A. Drylie, P. S. Wheatley, A. M. Z. Slawin, and R. E. Morris, "Ionothermal Materials Synthesis Using Unstable Deep-Eutectic Solvents as Template-Delivery Agents," *Angew. Chemie*, vol. 118, no. 30, pp. 5084–5088, Jul. 2006.

[21] R. M. Barrer, "33. Synthesis of a zeolitic mineral with chabazite-like sorptive properties," *J. Chem. Soc.*, p. 127, Jan. 1948.

[22] D. W. Breck, W. G. Eversole, R. M. Milton, T. B. Reed, and T. L. Thomas, "Crystalline Zeolites. I. The Properties of a New Synthetic Zeolite, Type A," *J. Am. Chem. Soc.*, vol. 78, no. 23, pp. 5963–5972, Dec. 1956.

[23] E. M. Flanigen, R. W. Broach, and S. T. Wilson, "Introduction to zeolites," 2010.

[24] R. V. Gaines, H. C. Skinner, E. E. Foord, B. Mason, and A. Rosenzweig, "Minerals Arranged by the New Dana Classification." [Online]. Available: http://webmineral.com/danaclass.shtml#77.1.

[25] R. Rinaldi, E. Passaglia, and D. Pongiluppi, "Merlinoite, a new mineral of the zeolite group," *NEUES JAHRBUCH FUR MINERALOGIE - MONATSHEFTE*, December, 1976.

[26] A. Bieniok, K. Bornholdt, U. Brendel, and W. H. Baur, "Synthesis and crystal structure of zeolite W, resembling the mineral merlinoite," *J. Mater. Chem.*, vol. 6, p. 271, 1996.

[27] A. Corma, M. J. Diaz-Cabanas, F. Rey, S. Nicolopoulus, and K. Boulahya, "ITQ-15: the first ultralarge pore zeolite with a bi-directional pore system formed by intersecting 14- and 12-ring channels, and its catalytic implications.," *Chem. Commun. (Camb).*, no. 12, pp. 1356–1357, 2004.

[28] P. A. Barrett, S. Valencia, and M. A. Camblor, "Synthesis of a merlinoite-type zeolite with an enhanced Si/Al ratio via pore filling with tetraethylammonium cations," *J. Mater. Chem.*, vol. 8, no. 10, pp. 2263–2268, 1998.

[29] M. Haouas, L. Lakiss, C. Martineau, J. El Fallah, V. Valtchev, and F. Taulelle, "Silicate ionic liquid synthesis of zeolite merlinoite: Crystal size control from crystalline nanoaggregates to micron-sized single-crystals," *Microporous Mesoporous Mater.*, vol. 198, pp. 35–44, 2014.

[30] J.-L. Paillaud, B. Harbuzaru, J. Patarin, and N. Bats, "Extra-Large-Pore Zeolites with Two-Dimensional Channels Formed by 14 and 12 Rings," *Science (80-.).*, vol. 304, no. 5673, pp. 990–992, 2004.

[31] W. J. Roth, P. Nachtigall, R. E. Morris, P. S. Wheatley, V. R. Seymour, S. E. Ashbrook, P. Chlubná, L. Grajciar, M. Položij, A. Zukal, O. Shvets, and J. Cejka, "A family of zeolites with controlled pore size prepared using a top-down method.," *Nat. Chem.*, vol. 5, no. 7, pp. 628–33, 2013.

[32] O. V. Shvets, P. Nachtigall, W. J. Roth, and J. Cejka, "UTL zeolite and the way beyond," *Microporous Mesoporous Mater.*, vol. 182, pp. 229–238, 2013.

[33] N. Kasian, E. Verheyen, G. Vanbutsele, K. Houthoofd, T. I. Koranyi, J. A. Martens, and C. E. A. Kirschhock, "Catalytic activity of germanosilicate UTL zeolite in bifunctional hydroisomerisation of n-decane," *Microporous Mesoporous Mater.*, vol. 166, pp. 153–160, 2013.

[34] T. Blasco, A. Corma, M. J. Díaz-Cabañas, F. Rey, J. A. Vidal-Moya, and C. M. Zicovich-Wilson, "Preferential Location of Ge in the Double Four-Membered Ring Units of ITQ-7 Zeolite," *J. Phys. Chem. B*, vol. 106, no. 10, pp. 2634–2642, Mar. 2002.

[35] E. Verheyen, L. Joos, K. Van Havenbergh, E. Breynaert, N. Kasian, E. Gobechiya, K. Houthoofd, C. Martineau, M. Hinterstein, F. Taulelle, V. Van Speybroeck, M. Waroquier, S. Bals, G. Van Tendeloo, C. E. a. Kirschhock, and J. a. Martens, "Design of zeolite by inverse sigma transformation," *Nat. Mater.*, vol. 11, no. 12, pp. 1059–1064, 2012.

[36] C. Cascales, E. Gutiérrez-Puebla, M. A. Monge, and C. Ruíz-Valero, "(NH4)2Ge7O15: A microporous material containing GeO4 and GeO6 polyhedra in nine-rings," *Angew. Chemie Int. Ed.*, vol. 37, no. 1–2, pp. 129–131, Feb. 1998.

[37] M. Mazur, M. Kubu, P. S. Wheatley, and P. Eliasova, "Germanosilicate UTL and its rich chemistry of solid-state transformations towards IPC-2 (OKO) zeolite," *Catal. Today*, vol. 243, no. C, pp. 23–31, 2015.

[38] J. Sun, C. Bonneau, A. Cantín, A. Corma, M. J. Díaz-Cabañas, M. Moliner, D. Zhang, M. Li, and X. Zou, "The ITQ-37 mesoporous chiral zeolite.," *Nature*, vol. 458, no. 7242, pp. 1154–7, Apr. 2009.

[39] A. Corma, F. Rey, S. Valencia, J. L. Jordá, and J. Rius, "A zeolite with interconnected 8-, 10- and 12-ring pores and its unique catalytic selectivity.," *Nat. Mater.*, vol. 2, no. 7, pp. 493–497, 2003.

[40] L. Burel, N. Kasian, and A. Tuel, "Quasi all-silica zeolite obtained by isomorphous degermanation of an as-made germanium-containing precursor," *Angew. Chemie - Int. Ed.*, vol. 53, no. 5, pp. 1360–1363, 2014.

[41] P. Chlubna-Eliasova, Y. Tian, A. B. Pinar, M. Kubu, J. Cejka, and R. E. Morris, "The assembly-disassembly-organization-reassembly mechanism for 3D-2D-3D transformation of germanosilicate IWW zeolite," *Angew. Chemie - Int. Ed.*, vol. 53, no. 27, pp. 7048–7052, 2014.

[42] P. Cubillas and M. W. Anderson, "Synthesis Mechanism: Crystal Growth and Nucleation," in *Zeolites and Catalysis: Synthesis, Reactions and Applications*, J. Cejka, A. Corma, and S. Zones, Eds. WILEY-VCH Verlag GmbH, 2010, p. 918.

[43] G. Cao and Y. Wang, “Fundamentals of homogeneous nucleation,” *Nanostructures Nanomater. Synth. Prop. Appl.*, vol. 3, pp. 68–69, 2004.

[44] F. Di Renzo, “Zeolites as tailor-made catalysts: Control of the crystal size,” *Catal. Today*, vol. 41, no. 1–3, pp. 37–40, May 1998.

[45] J. Ulrich, T. Stelzer, John W. Mullin, and J. W. Mullin, “Crystallization,” *Kirk-Othmer Encycl. Chem. Technol.*, pp. 1–63, 2001.

[46] L. N. Rashkovich, J. J. Yoreo, C. a. Orme, and a. a. Chernov, “In situ atomic force microscopy of layer-by-layer crystal growth and key growth concepts,” *Crystallogr. Reports*, vol. 51, no. 6, pp. 1063–1074, 2006.

[47] P. Smereka, “Spiral crystal growth,” *Phys. D Nonlinear Phenom.*, vol. 138, no. 3–4, pp. 282–301, 2000.

[48] A. M. Walker, B. Slater, J. D. Gale, and K. Wright, “Predicting the structure of screw dislocations in nanoporous materials.,” *Nat. Mater.*, vol. 3, no. 10, pp. 715–20, 2004.

[49] I. Sunagawa, “Growth and Morphology of Crystals,” *Forma*, vol. 14, no. 358, pp. 147–166, 1999.

[50] G. Binnig and C. F. Quate, “Atomic Force Microscope,” *Phys. Rev. Lett.*, vol. 56, no. 9, pp. 930–933, Mar. 1986.

[51] University of Camebridge, “Atomic Force Microscopy,” 2014. [Online]. Available: http://www.doitpoms.ac.uk/tlplib/afm/intro.php.

[52] P. C. Braga and D. Ricci, “Atomic Force Microscopy: Theory and Practice in Bacteria Morphostructural Analysis,” *Antibiot. Resist. Methods Protoc.*, vol. 242, no. 2, pp. 199–207, 2004.

[53] L. Grossman, “Focus: Electric Field from a Built-In Flex,” *Physics (College. Park. Md).*, vol. 28, Jul. 2011.

[54] University of Hamburg, “Atomic Force Microscopy.” [Online]. Available: http://www.nanoscience.de/HTML/methods/afm.html.

[55] Uppsala Universitet, “Atomic force microscopy (AFM).” [Online]. Available: http://www.farmfak.uu.se/farm/farmfyskem/instrumentation/afm.html.

[56] A. Alessandrini and P. Facci, “AFM: a versatile tool in biophysics,” *Meas. Sci. Technol.*, vol. 16, no. 6, pp. R65–R92, 2005.

[57] F. J. Giessibl, “Advances in atomic force microscopy,” *Rev. Mod. Phys.*, vol. 75, p. 949, 2003.

[58] nanoScience Instruments, “AFM modes,” 2016. [Online]. Available: http://www.nanoscience.com/products/afm/technology-overview/afm-modes/.

[59] F. Moreno-Herrero, J. Colchero, J. G??mez-Herrero, and A. M. Baro, “Atomic force microscopy contact, tapping, and jumping modes for imaging biological samples in liquids,” *Phys. Rev. E - Stat. Nonlinear, Soft Matter Phys.*, vol. 69, no. 3 1, pp. 1–9, 2004.

[60] H.-Q. Li, “The Common AFM Modes,” 1997. [Online]. Available: http://www.chemistry.uoguelph.ca/educmat/chm729/afm/details.htm.

[61] R. Brent and M. W. Anderson, “Fundamental crystal growth mechanism in zeolite L revealed by atomic force microscopy,” *Angew. Chemie - Int. Ed.*, vol. 47, no. 29, pp. 5327–5330, 2008.

[62] L. I. Meza, M. W. Anderson, and J. R. Agger, “Differentiating fundamental structural units during the dissolution of zeolite A.,” *Chem. Commun. (Camb).*, no. 24, pp. 2473–2475, 2007.

[63] L. van Tendeloo, M. Haouas, J. A. Martens, C. E. A. Kirschhock, E. Breynaert, and F. Taulelle, “Zeolite synthesis in hydrated silicate ionic liquids,” *Faraday Discuss.*, vol. 179, pp. 437–449, 2015.

[64] O. V. Shvets, A. Zukal, N. Kasian, N. Zilkova, and J. Cejka, “The role of crystallization parameters for the synthesis of germanosilicate with UTL topology,” *Chem. - A Eur. J.*, vol. 14, no. 32, pp. 10134–10140, 2008.

[65] R. Yuan, N. Claes, E. Verheyen, A. Tuel, S. Bals, E. Breynaert, J. A. Martens, and C. E. A. Kirschhock, “Synthesis of an IWW-type germanosilicate zeolite using 5-azonia-spiro[4,4]nonane as a structure directing agent,” *New J. Chem.*, 2016.

[66] P. a. Zielinski, a. Van Neste, D. B. Akolekar, and S. Kaliaguine, “Effect of high-energy ball milling on the structural stability, surface and catalytic properties of small-, medium- and large-pore zeolites,” *Microporous Mater.*, vol. 5, no. 3, pp. 123–133, 1995.

[67] Eskens, “TURBULA shaker mixer,” 2016. [Online]. Available: http://www.eskens.com/producten/turbula-shaker-mixer/.

[68] M. De Prins, “COK-14 catalyst activation and optimization for hydroisomerization and -cracking of hydrocarbons,” KU Leuven, 2014.

[69] KU Leuven - Nuclear Solid State Group, “X-ray diffraction – Bruker D8 Discover,” 2016. [Online]. Available: https://fys.kuleuven.be/iks/nvsf/experimental-facilities/x-ray-diffraction-2013-bruker-d8-discover.

[70] The Linde Group, “Inductively coupled plasma,” 2016. [Online]. Available: http://hiq.linde-gas.com/en/analytical_methods/inductively_coupled_plasma.html.

[71] Evans Analytical Group, “CP-OES vs ICP-MS: A Comparison,” 2016. [Online]. Available: http://www.eag.com/mc/icp-oes-vs-icp-ms.html.

[72] H.-F. Chen, J.-N. Fang, H.-J. Lo, S.-R. Song, Y.-L. Chen, S.-H. Chung, C.-Y. Lee, L.-J. Li, and I.-C. Lin, “THE SYNTHESIS OF MERLINOITE,” *West. Pacific Earth Sci.*, vol. 2, no. 4, pp. 365–380, 2002.

[73] R. W. Thompson, “Nucleation, growth and seeding in zeolite synthesis,” *Verified Syntheses of Zeolitic Materials*. [Online]. Available: http://www.iza-online.org/synthesis/ VS_2ndEd/ Nucleation.htm.

[74] R. L. Smith, P. Eliasova, M. Mazur, M. P. Attfield, J. Cejka, and M. W. Anderson, “Atomic force microscopy of novel zeolitic materials prepared by top-down synthesis and ADOR mechanism,” *Chem. - A Eur. J.*, vol. 20, no. 33, pp. 10446–10450, 2014.

[75] K. Akçay, A. Sirkecioglu, M. Tatlier, Ö. T. Savasçi, and A. Erdem-Senatalar, “Wet ball milling of zeolite HY,” *Powder Technol.*, vol. 142, no. 2–3, pp. 121–128, 2004.

Appendix A: ^{27}Al NMR spectra of MER supernatant solutions

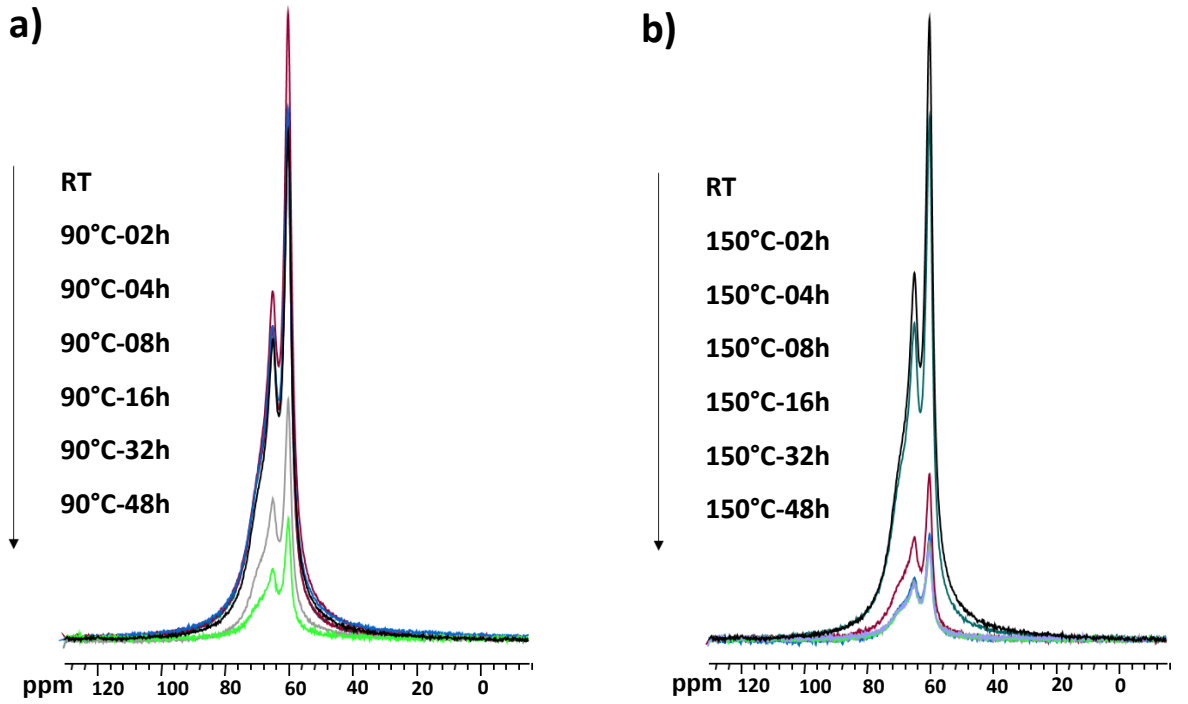

Samples	Al q^n (%)					Rel. Conc. (%)	Avg. Conn. <n>
	0	1	2	3	4		
RT	0	0	25	34	41	100	3.15
90°C-02h	0	0	25	38	37	104	3.12
90°C-04h	0	0	17	42	40	110	3.23
90°C-08h	0	0	32	33	36	100	3.04
90°C-16h	0	0	19	43	38	97	3.18
90°C-32h	0	0	18	42	40	44	3.22
90°C-48h	0	0	21	41	38	21	3.17

Samples	Al q^n (%)					Rel. Conc. (%)	Avg. Conn. <n>
	0	1	2	3	4		
RT	0	0	25	34	41	100	3.15
150°C-02h	0	0	28	35	37	86	3.08
150°C_04h	0	0	29	38	33	27	3.05
150°C_08h	0	0	17	44	39	15	3.22
150°C_16h	0	0	20	42	38	14	3.19
150°C_32h	0	0	20	43	37	14	3.17
150°C_48h	0	0	24	40	36	14	3.12

Figure i: *^{27}Al NMR spectra of supernatant solutions collected after 0, 2, 4, 8, 16, 32 and 48 hours of synthesis at a) 90 °C and b) 150 °C. The average connectivity of the aluminate species ($q^{<n>}$) is quantified in the accompanying tables. No clear changes in Al speciation were observed. Al concentrations are normalized with respect to the initial mixture at room temperature (RT) (= 100 %). Al solubility is reached at 21 % and 14 % of the initial Al concentration for the syntheses at 90 °C and 150 °C respectively. Deviations in the measurements can be attributed to anomalies with the NMR probe.*

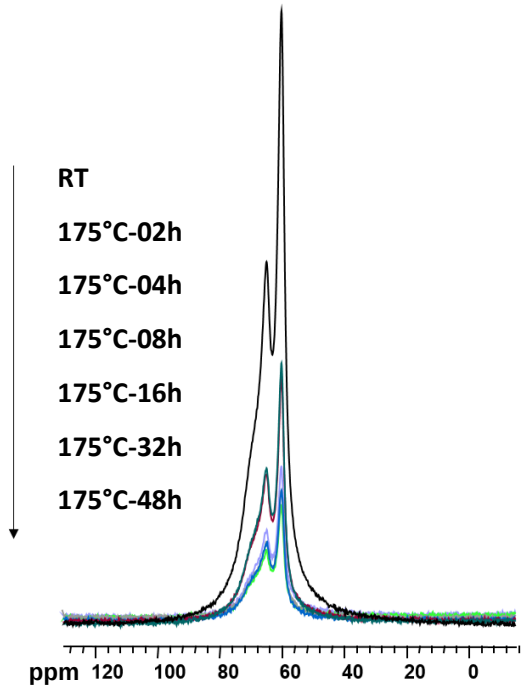

Samples	Al q^n (%)					Rel. Conc. (%)	Avg. Conn. <n>
	0	1	2	3	4		
RT	0	0	25	34	41	100	3.15
175°C-02h	0	0	22	41	37	40	3.15
175°C-04h	0	0	19	43	38	37	3.18
175°C-08h	0	0	20	42	38	19	3.18
175°C-16h	0	0	21	41	38	19	3.18
175°C-32h	0	0	18	43	39	16	3.21
175°C-48h	0	0	17	42	41	20	3.24

Figure ii: *^{27}Al NMR spectra of supernatant solutions collected after 0, 2, 4, 8, 16, 32 and 48 hours of synthesis at 175 °C. The average connectivity of the aluminate species ($q^{<n>}$) is quantified in the accompanying table. No clear changes in Al speciation were observed. Al concentrations are normalized with respect to the initial mixture at room temperature (RT). Al solubility is reached at 20 % of the initial Al concentration. Deviations in the measurements can be attributed to anomalies with the NMR probe.*

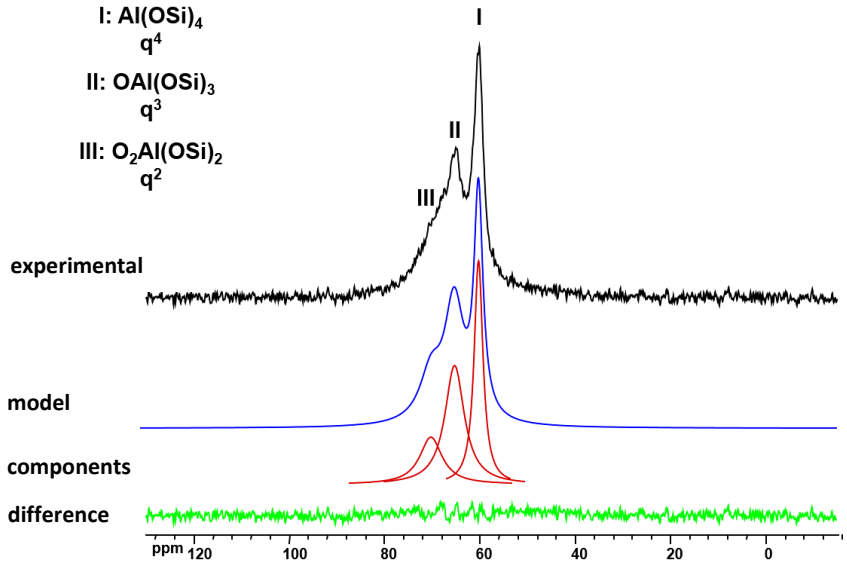

Figure iii: *Example of spectral decomposition of ^{27}Al signal obtained from MER sample synthesized at 150 °C for 32 hours, allowing identification and quantitation of the different aluminate species.*

Appendix B: ^{29}Si NMR spectra of MER supernatant solutions

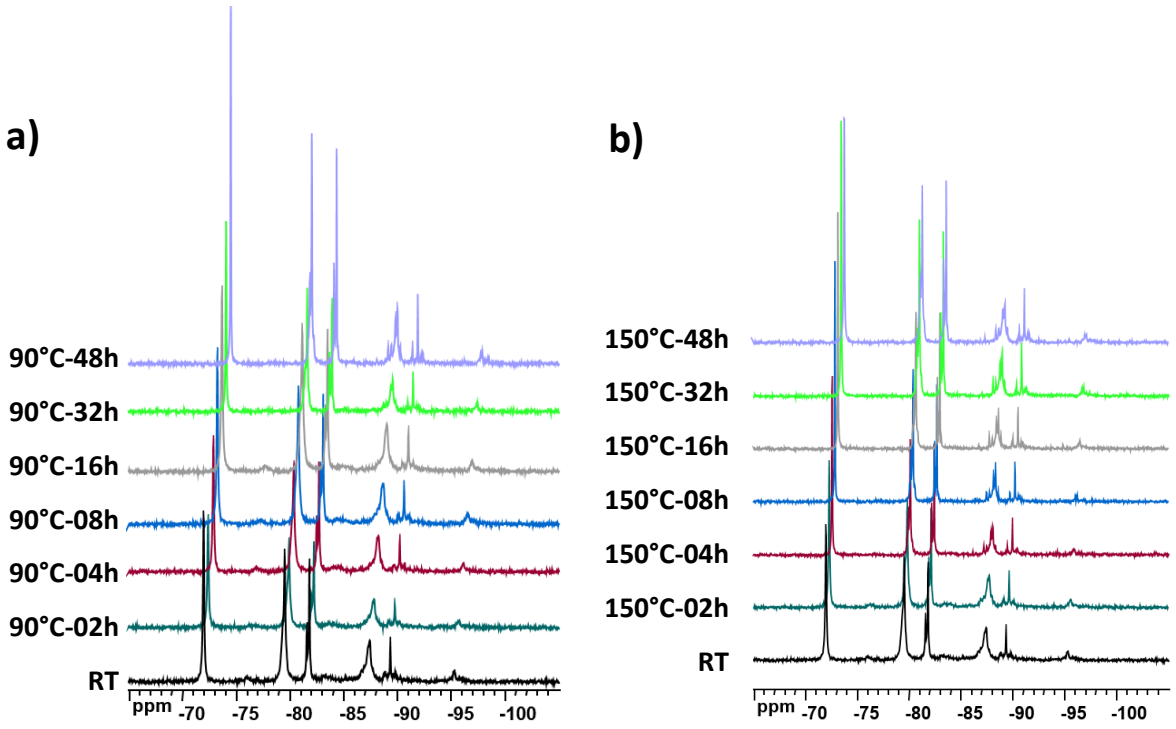

Samples	Si q^n (%)					Rel. Conc. (%)	Avg. Conn. <n>
	0	1	2	3	4		
RT	23	28	44	4	0	100	1.30
90°C_02h	21	29	46	4	0	78	1.33
90°C_04h	20	30	46	4	0	95	1.34
90°C_08h	24	29	44	4	0	99	1.28
90°C_16h	27	29	41	3	0	102	1.20
90°C_32h	21	30	43	6	0	77	1.34
90°C_48h	21	29	44	5	0	104	1.33

Samples	Si q^n (%)					Rel. Conc. (%)	Avg. Conn. <n>
	0	1	2	3	4		
RT	23	28	44	4	0	100	1.30
150°C_02h	24	28	44	4	0	95	1.27
150°C_04h	21	30	43	6	0	79	1.34
150°C_08h	21	32	43	5	0	79	1.31
150°C_16h	20	30	43	6	0	87	1.35
150°C_32h	25	29	42	4	0	102	1.25
150°C_48h	27	28	42	3	0	98	1.22

Figure iv: *^{29}Si NMR spectra of supernatant solutions collected after 0, 2, 4, 8, 16, 32 and 48 hours of synthesis at a) 90 °C and b) 150 °C. The spectra were constructed with a small increment for clarity. The average connectivity of the silicate species ($q^{<n>}$) is quantified in the accompanying tables. No significant changes in Si speciation were observed. Si concentrations are normalized with respect to the initial mixture at room temperature (RT). Concentration changes are within the margin of error of the experimental set-up and can be neglected.*

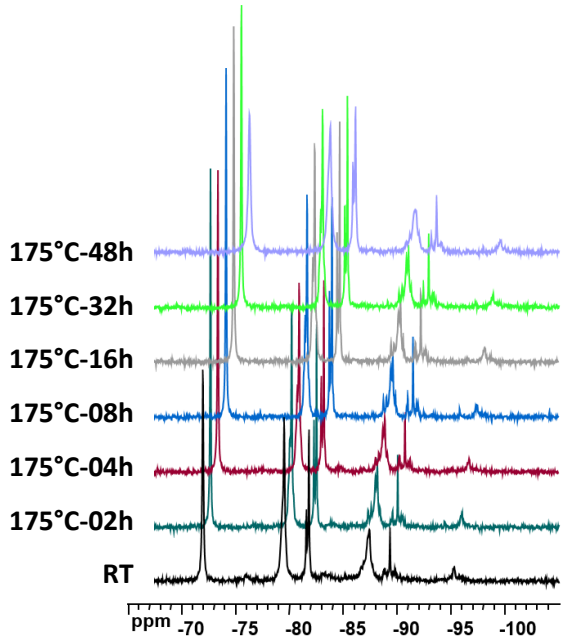

Samples	Si q^n (%)					Rel. Conc. (%)	Avg. Conn. <n>
	0	1	2	3	4		
RT	23	28	44	4	0	100	1.30
175°C_02h	24	30	43	3	0	40	1.25
175°C_04h	25	29	42	4	0	37	1.24
175°C_08h	26	28	42	3	0	19	1.22
175°C_16h	26	28	43	4	0	19	1.24
175°C_32h	26	28	43	4	0	16	1.24
175°C_48h	27	27	42	4	0	20	1.23

Figure v: *^{29}Si NMR spectra of supernatant solutions collected after 0, 2, 4, 8, 16, 32 and 48 hours of synthesis at 175 °C. The spectra were constructed with a small increment for clarity. The average connectivity of the silicate species ($q^{<n>}$) is quantified in the accompanying table. No significant changes in Si speciation were observed. Si concentrations are normalized with respect to the initial mixture at room temperature (RT). Concentration changes are within the margin of error of the experimental set-up and can be neglected.*

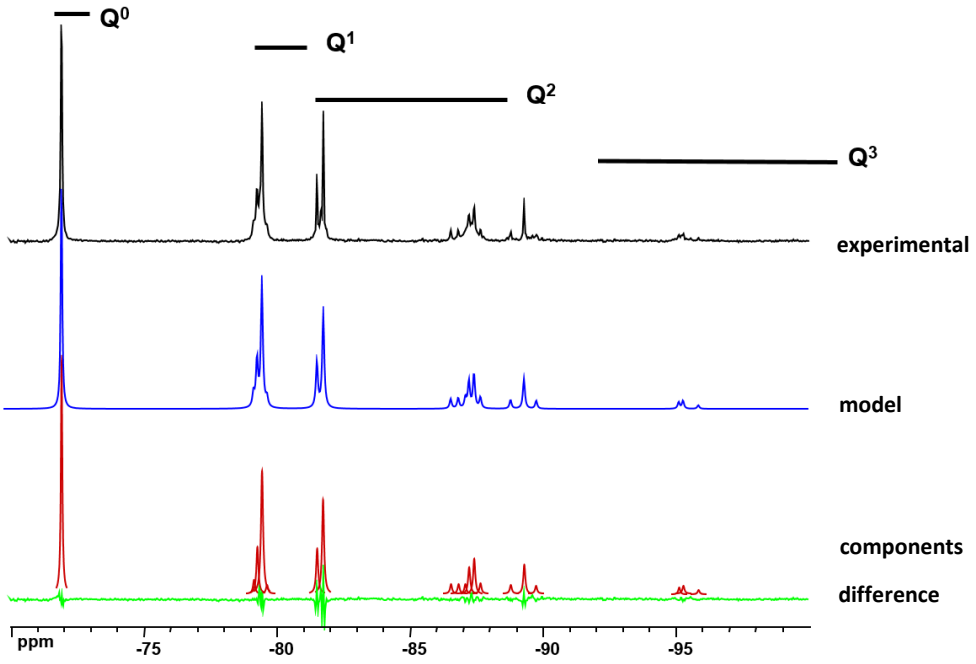

Figure vi: *Example of spectral decomposition of ^{29}Si signal obtained from MER sample synthesized at 150 °C for 32 hours, allowing identification and quantitation of the different silicate species.*

Appendix C: ^{39}K NMR spectra of MER supernatant solutions

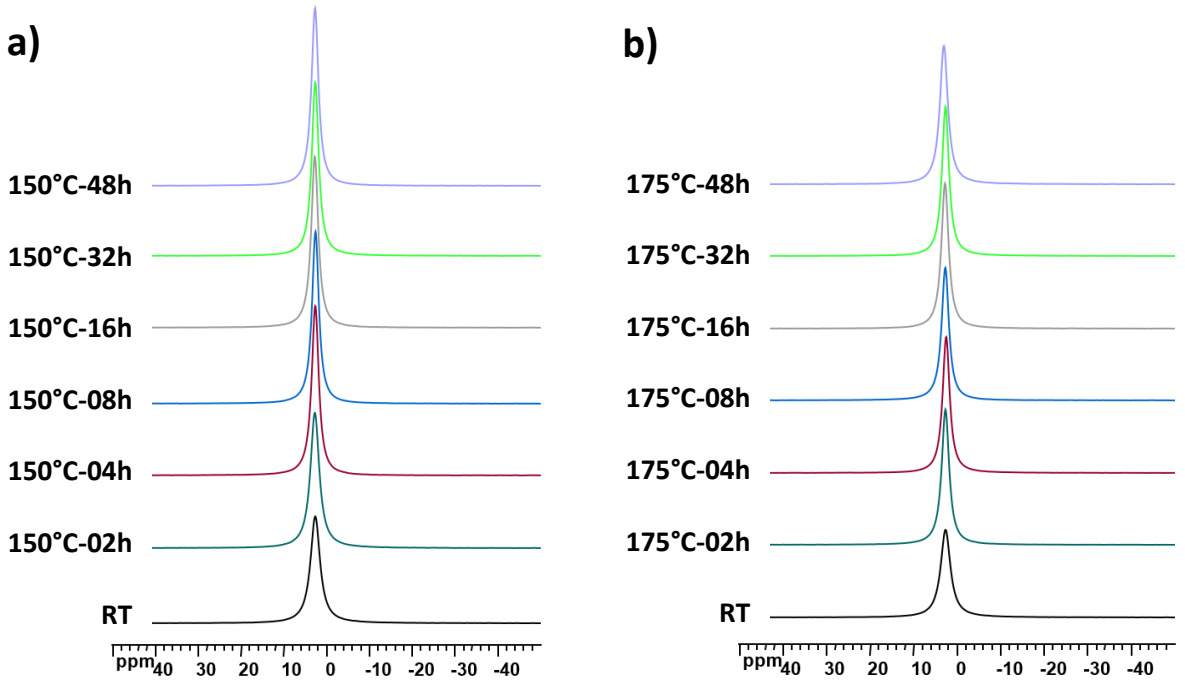

Samples	δ (ppm)	Rel. Conc. (%)
RT	2.6	82
150°C_02h	2.7	98
150°C_04h	2.6	98
150°C_08h	2.6	96
150°C_16h	2.7	98
150°C_32h	2.6	100
150°C_48h	2.7	104

Samples	δ (ppm)	Rel. Conc. (%)
RT	2.6	82
175°C_02h	2.7	99
175°C_04h	2.5	96
175°C_08h	2.7	95
175°C_16h	2.7	103
175°C_32h	2.6	104
175°C_48h	3.0	107

Figure vii: *^{39}K NMR spectra of supernatant solutions collected after 0, 2, 4, 8, 16, 32 and 48 hours of synthesis at a) 150 °C and b) 175 °C. Chemical shift (δ) with respect to the KCl reference solution are quantified in the accompanying tables. K concentrations are normalized with respect to the initial mixture at room temperature (RT). Concentration changes are within the margin of error of the experimental set-up and can be neglected.*

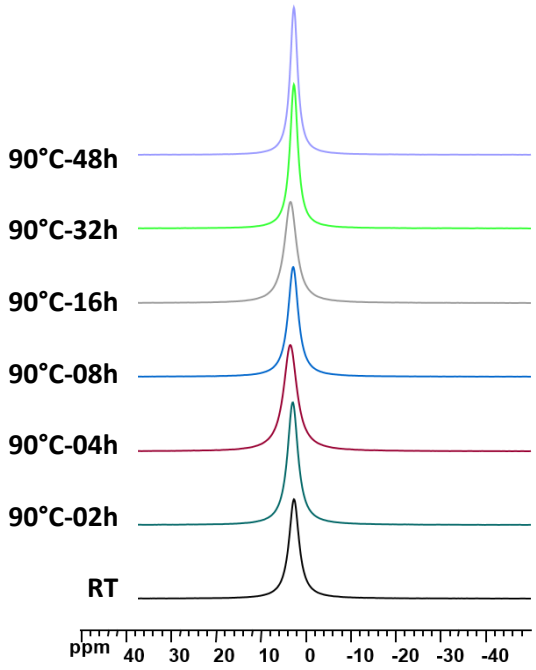

Samples	δ (ppm)	Rel. Conc. (%)
RT	2.6	82
90°C_02h	2.9	109
90°C_04h	3.5	115
90°C_08h	2.8	88
90°C_16h	2.6	92
90°C_32h	2.6	85
90°C_48h	2.7	91

Figure viii: *^{39}K spectrum of supernatant solutions collected after 0, 2, 4, 8, 16, 32 and 48 hours of synthesis at 90 °C. Chemical shift (δ) with respect to the KCl reference solution are quantified in the accompanying tables. The quantitation is not accurate because the tuning of the probe was not properly adjusted. However, this does not affect the overall result at all and only concerns this series of measurements.*

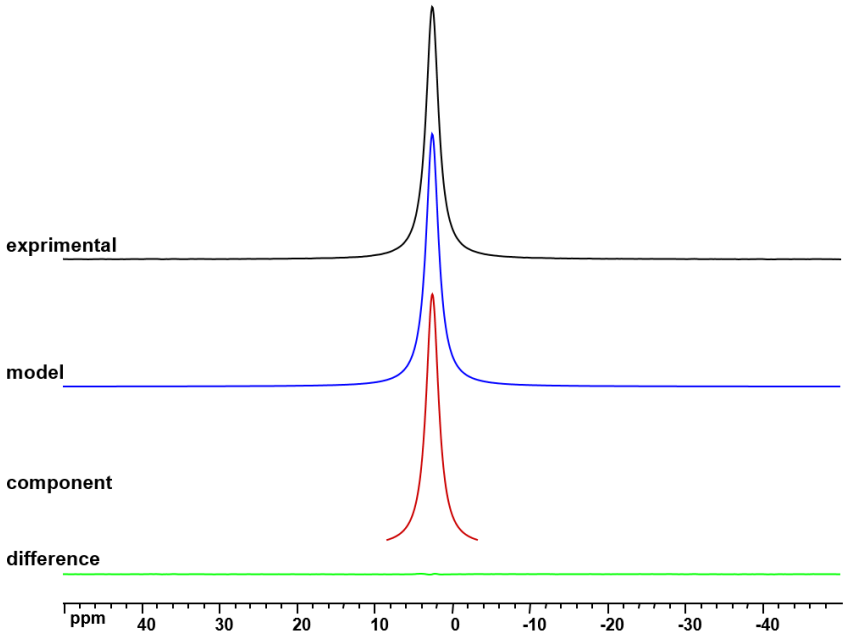

Figure ix: *Example of spectral decomposition of ^{39}K signal obtained from MER sample synthesized at 150 °C for 32 hours, allowing quantitation of the K concentration.*

Appendix D: XRD patterns of solid phases collected after MER synthesis at 90, 150 and 175 °C.

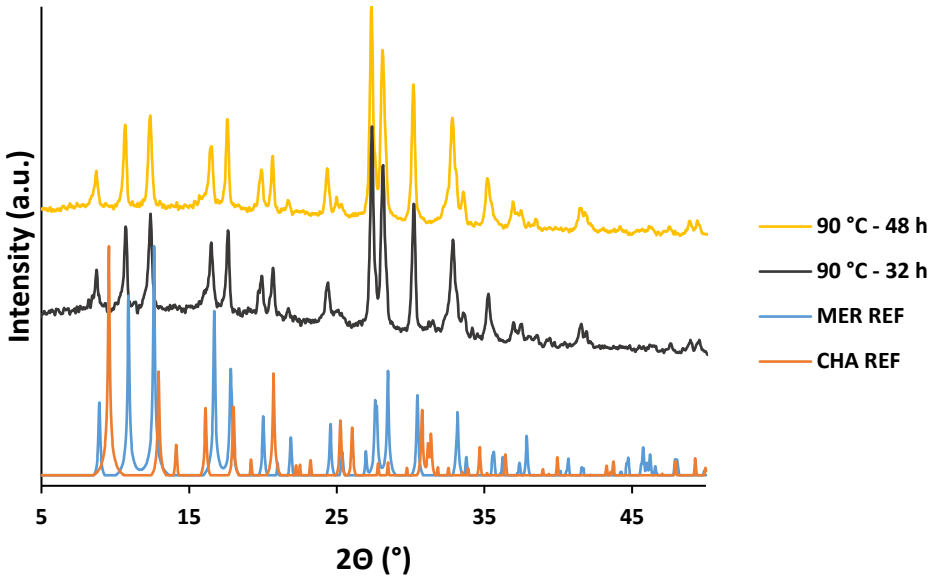

Figure x: *XRD patterns of solid phase recovered from MER synthesis at 90 °C for 32 and 48 hours. No solids could be isolated from the other syntheses. These patterns indicate the predominant formation of MER as almost no characteristic CHA reflections are visible. CHA and MER reference patterns are presented in orange and light blue respectively*

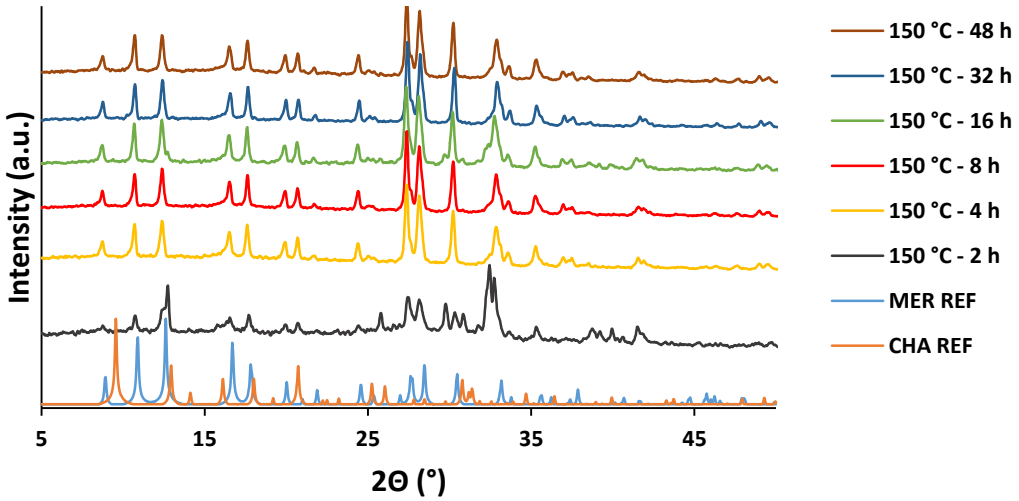

Figure xi: *XRD patterns of solid phase recovered from MER synthesis at 150 °C for 2, 4, 8, 16, 32 and 48 hours. The solids obtained after 2 hours of synthesis exhibit a limited degree of crystallinity. Synthesis times of 4 hours and more clearly favor the formation of MER. CHA and MER reference patterns are presented in orange and light blue respectively*

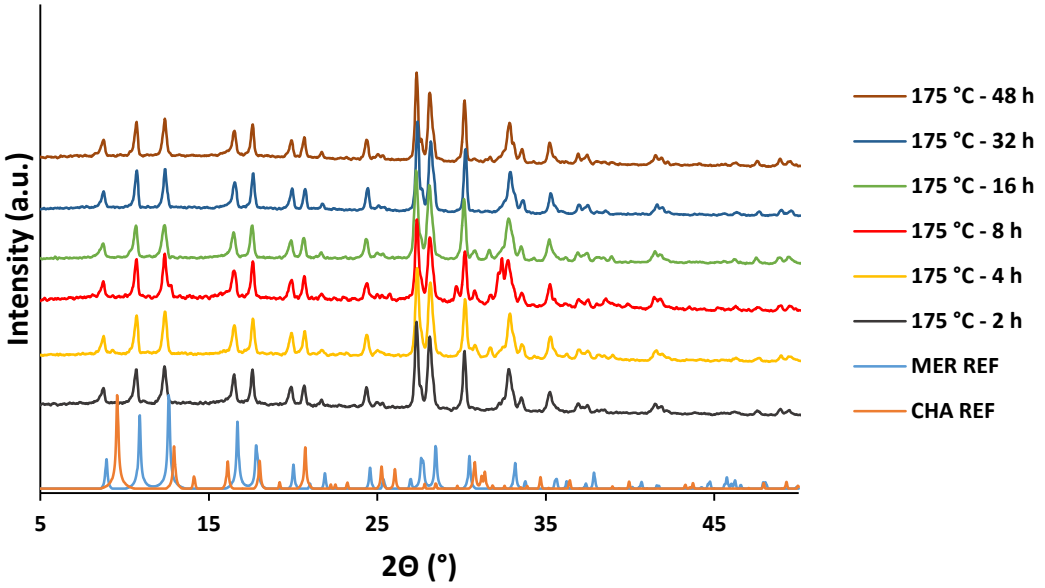

Figure xii: *XRD patterns of solid phase recovered from MER synthesis at 175 °C for 2, 4, 8, 16, 32 and 48 hours. Already after 2 hours, it is clear that MER is almost exclusively formed. CHA and MER reference patterns are presented in orange and light blue respectively*

Appendix E: Additional AFM images of as-synthesized UTL

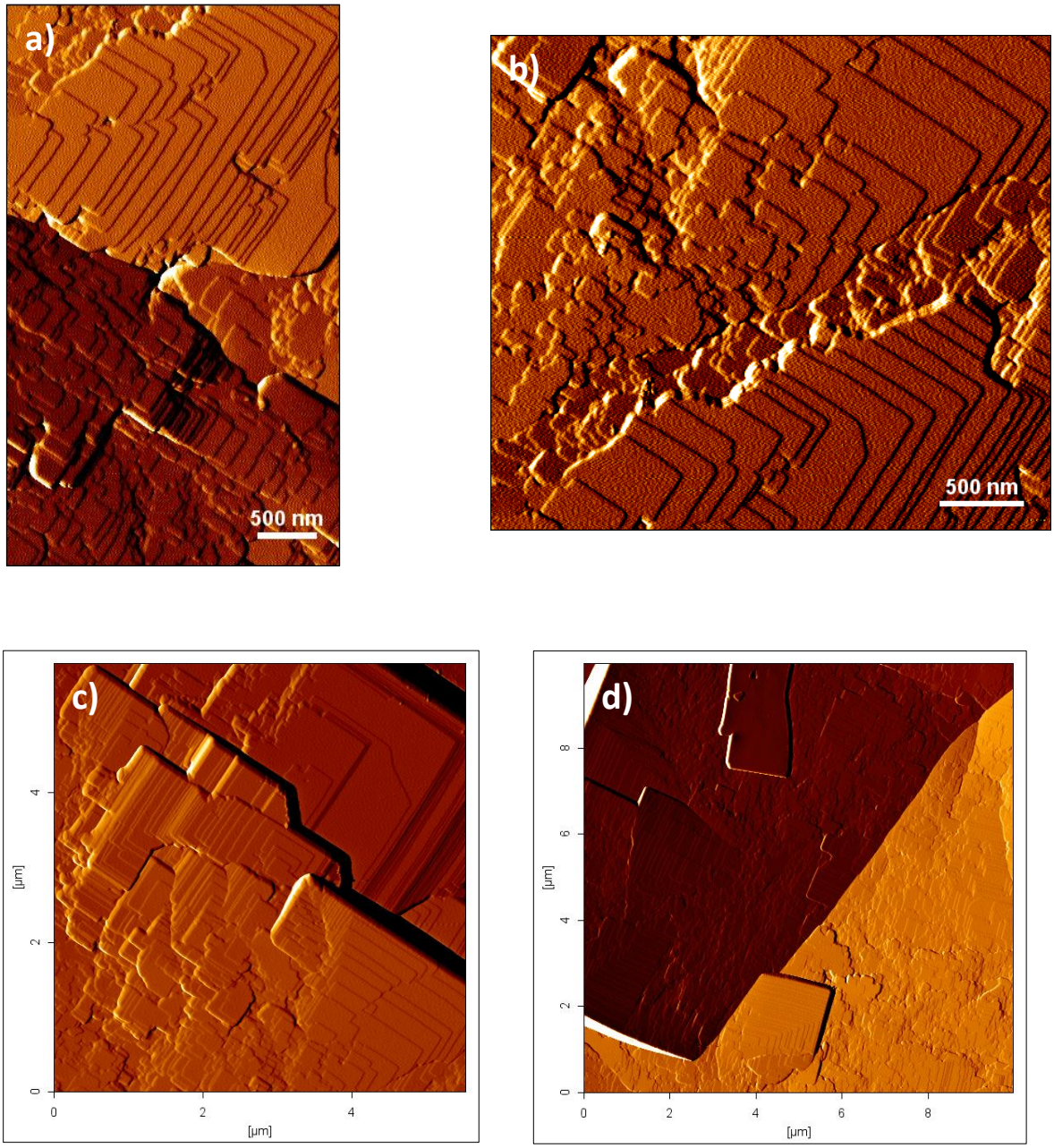

Figure xiii: *a-d) Cm-AFM vertical deflection images of the AS UTL surface.*

Appendix F: Additional AFM images of -COK-14

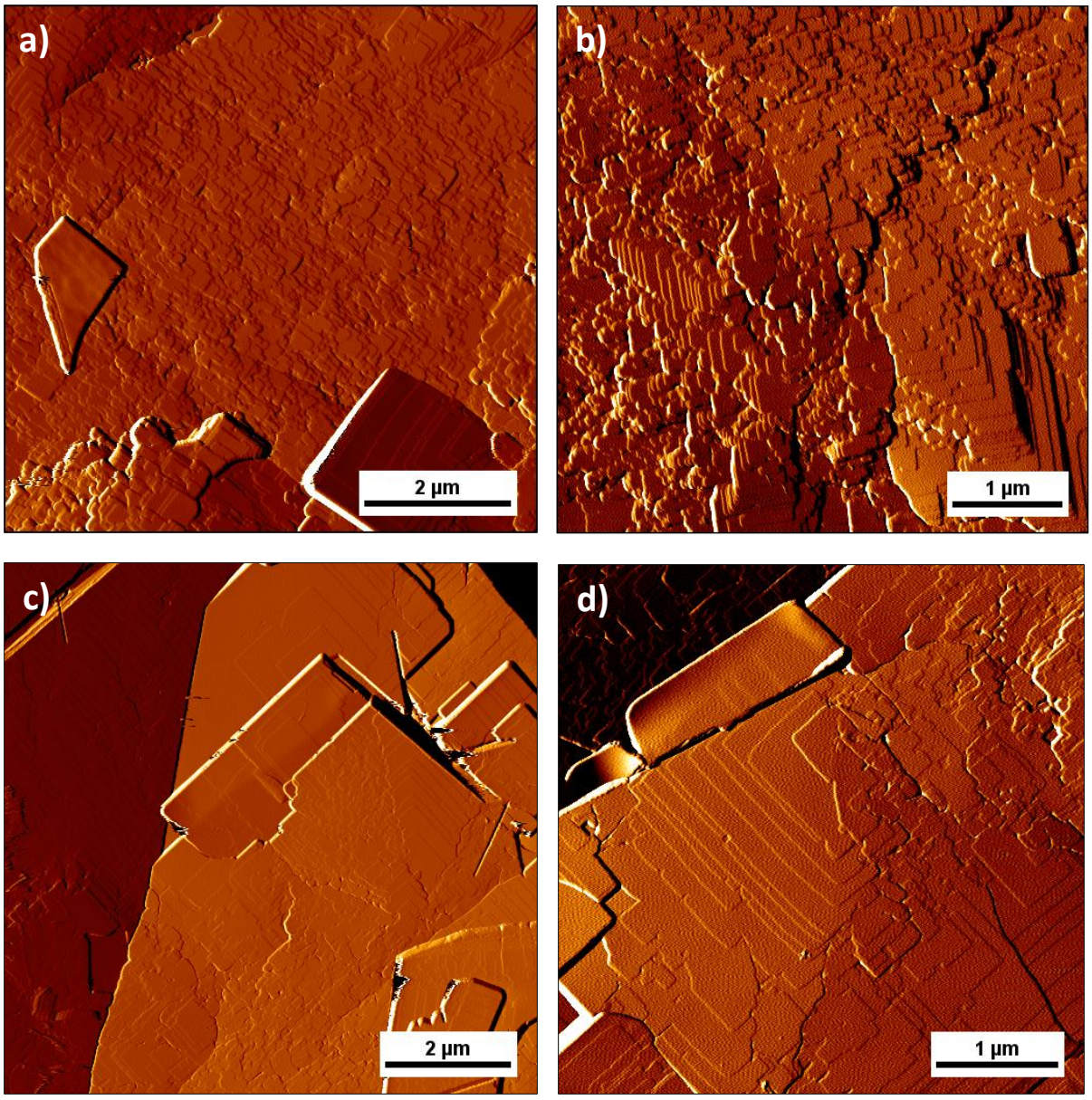

Figure xiv: *a-d) Cm-AFM vertical deflection images of -COK-14.*

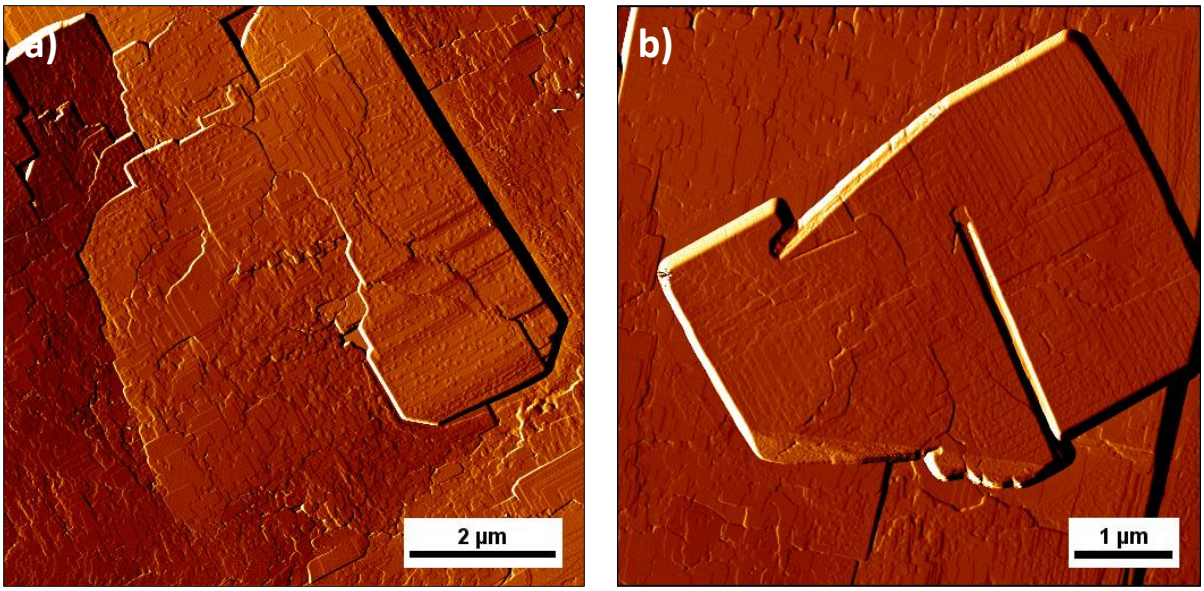

Figure xv: *a-b) Cm-AFM vertical deflection images of -COK-14, demonstrating the extensive occurrence of 'lumps' on the surface.*

Appendix G: Risk assessment

The risk assessment of the performed experiments is provided on the following pages.

DIENSTEN ALGEMEEN BEHEER
DIRECTIE STAFDIENSTEN ALGEMEEN BEHEER
DIENST VGM
W. DE CROYLAAN 58 – BUS 5530, BE-3001 LEUVEN
TEL. + 32 16 32 20 24 FAX + 32 16 32 29 95
WWW.KULEUVEN.BE/VGM vgm@kuleuven.be

KATHOLIEKE
UNIVERSITEIT
LEUVEN

NOTIFICATION FORM:
RISK ASSESSMENT FOR EXPERIMENT WITH CHEMICALS PRODUCTS IN HAZARD CLASS E3 EN E4

Complete the form electronically, in consultation with your specialised HSE Contact chemical safety.

1. Identification of the division (users)

Application/contact person: Maarten Houlleberghs
Tel: +32 496 67 580 2
E-mail address: maarten.houlleberghs@student.kuleuven.be

Division: COK
Stockroom code[1]:
Head: Johan Martens

2. Identification of the experiment

Title(name): Synthesis of merlinoite + post-treatment (max. 40 characters)
Start date: 1/10/2015 Planned end date: 25/04/2016

☒ New experiment
☐ Existing experiment without prior risk assessment
☐ Modification/expansion of an existing experiment with prior risk assessment
This modification/expansion concerns (please indicate and describe in the form):
☐ persons
☐ rooms of the experiment
☐ chemicals products
☐ other risks
☐ prolongation
File number or reference number previous advice: ☐ (if known)

☐ If HSE FILE available:
☐ experiment in the context of an existing activity
Give the number of the activities:
☐ experiment in the context of a new activity (in consultation with specialised HSE Contact and head of division[1])
Give the title of the new activity for the HSE-file: (max. 40 characters)

☒ Continuous tests (**unattended** activity within or outside working hours)

[1] https://admin.kuleuven.be/vgm/intranet/doc/antenne/antennemagazijncodes.xlsx/view[1]

Description of the chemicals used (or formed)*

Product name	Cas number	Physical state (solid/liquid/ gas)	Quantity used	Concentration used	Chemical hazard class (E4/E3/E2/E1)
1. Tetraethylsilicate	78-10-4	Liquid	1 kg	98%	E2
2. Potassium hydroxide	1310-58-3	Solid	550 g	pure	E3
3. Sodium hydroxide	1310-73-2	Solid	5 g	pure	E3
4. Aluminumisopropoxide	555-31-7	Solid	50 g	98+%	E4
5. Perchloric acid	7601-90-3	Liquid	5 mL	70%	E3
6.					

*** If possible, replace highly hazardous products or processes by less hazardous ones !**

Location of experiment

Building	Room	Description of subactivity (eg. preparation, experiment, follow-up, measurement,…)	Room specifications
Corelab 1A	02-184 (SYN 12)	1. Preparation of solutions	☒ within your own division ☐ allocated to another division*
Corelab 1A	02-180 (SYN 13)	2. Washing + Centrifuging	☐ within your own division ☒ allocated to another division*
Corelab 1A	02-306 (SYN 20)	3. Drying	☒ within your own division ☐ allocated to another division*
Corelab 1A	02-314 (oven room)	4. Synthesis of MER at pre-defined temperature	☒ within your own division ☐ allocated to another division*
Corelab 1A	03.301	5. Ball-milling experiment with Turbula	☒ within your own division ☐ allocated to another division*

* If experiments are conducted in a room allocated to another division, please send also the notification form to this head of division (in copy).

Persons who conducting the experiment or for a practical the supervisors

Name – first name	Birth date	Staff category
Houlleberghs Maarten	**27/03/1991**	☐ KU ☒ Student KU ☐ UZ ☐ VIB ☐ Externals:
Lieben Sara	**22/01/1991**	☒ KU ☐ Student KU ☐ UZ ☐ VIB ☐ Externals:
		☐ KU ☐ Student KU ☐ UZ ☐ VIB ☐ Externals:
		☐ KU ☐ Student KU ☐ UZ ☐ VIB ☐ Externals:
		☐ KU ☐ Student KU ☐ UZ ☐ VIB ☐ Externals:
		☐ KU ☐ Student KU ☐ UZ ☐ VIB ☐ Externals:
		☐ KU ☐ Student KU ☐ UZ ☐ VIB ☐ Externals:
		☐ KU ☐ Student KU ☐ UZ ☐ VIB ☐ Externals:
		☐ KU ☐ Student KU ☐ UZ ☐ VIB ☐ Externals:

3. Description experiment and risk assessment

Description of handling and techniques:

Number* of sub-experiment	Description of handling and techniques	Equipment used	Numbers ** of products used
1	Preparation of HSIL and aluminate precursor + Preparation of MER synthesis mixture with composition 0.5 SiO2 : 0.013 Al2O3 : 1 KOH : 8 H2O + Synthesis at 90, 150 and 175 °C + Sampling of supernatant after centrifuging + Washing solid phase with water (4x) and drying solids at 60 °C	Balance, glassware, 250 ml and 125 ml PP bottles, stirring plate and magnetic stirring rods, centrifuge, pasteur pipettes, separatory funnel	1,2,4
2	Alkaline post-treatment of MER with 0.5M NaOH solution	Balance, small PP vial, heating/stirring plate + magnetic stirring rod	3
3	Acidic post-treatment of MER with 0.5M perchloric acid solution	Balance, small PP vial, heating/stirring plate + magnetic stirring rod	5
4	Ball-milling experiment with Turbula	Turbula, glass milling balls (2 and 5 mm), small PP vial	/
5			

* Number of the subactivity as indicated under “Location of experiment”

** Number of the chemicals as indicated in “Description of the chemicals used (or formed)”

Frequency of the experiment:

- ☒ Daily
- ☒ Weekly
- ☐ Monthly
- ☐ Less than monthly

Optionally, more information about the experiment can be added (eg. reaction scheme)

Risks associated with the chemicals

Before handling chemicals, identify their hazards (R or H and S or P phrases)!

These can be found in the KU Leuven database of hazardous substances (via KU Loket, General, Hazardous materials) or in the manufacturer’s safety data sheets.

In the table below, indicate the hazards of the products in risk class E3 and **E4**.

Name of chemical	Tetraethylsilicate	Potassium hydroxide	Sodium hydroxide	Aluminum-isopropoxide	Perchloric acid	
Explosion and fire hazard						
Extremely or highly flammable (**H220, H222,224, H228,** H225) / (R11,R12)	☒	☐	☐	☒	☐	☐
Flammable gas, aerosol, solid (H221, H223**, H228**)	☐	☐	☐	☐	☐	☐
Self heating, my catch fire **(H251,H252)**	☐	☐	☐	☐	☐	☐
Fire, explosive – projection hazard (H204, **H202**, **H203**), Mass explode in fire (H205)	☐	☐	☐	☐	☐	☐
Explosive (**EUH001, EUH006, H200, H201**) /(**R1,R2,R3**,R5) +combustible materials (H271, H272)/(R9) + T↑(H240, H241), sealed and T↑ (EUH044) /(R44)	☐	☐	☐	☐	☒	☐
Flammable vapour-air mixture (EUH018)	☐	☐	☐	☐	☐	☐
Explosive peroxides (EUH019)						
Incompatible with water (EUH014, H260) /(R14,R15)	☐	☐	☐	☐	☐	☐
Catches fire spontaneously if exposed to air **(H250)**	☐	☐	☐	☐	☐	☐
Explosive + metals (R4) + O2 **(R6**)	☐	☐	☐	☐	☐	☐
Incompatible with oxidizing materials (R16)	☐	☐	☐	☐	☐	☐
Unstable product (**R17**, R18, R19)	☐	☐	☐	☐	☐	☐
Acute health hazard						
Highly toxic (**H300, H330, H310**) / (**R26, R27, R28**) + acid (EUH032)/ (R32) Toxic (H311, H331, EUH070) / (R23, R24) + water (EUH029) / (R29) + acid (EUH031) / (R31)	☐	☐	☐	☐	☐	☐
Sever burns (H314) / (R35)	☐	☒	☒	☐	☒	☐
Long-term health hazard						
Carcinogenic or possible carcinogenic (**H350, H350i, H351**) / (**R40, R45, R49**)	☐	☐	☐	☐	☐	☐
Teratogenic (H361d, **H360D**) / (**R61**, R63) and harmful to fertility (H361f, **H360F**) / (**R60**, R62) , both hazards (H361fd, **H360FD, H360Df**, **H360Fd)**	☐	☐	☐	☐	☐	☐
Mutagenic (H341, **H340**) / (**R46**)	☐	☐	☐	☐	☐	☐
Damage to certain organs (H371, H372, **H370**) through prolonged or repeated exposure (H373)	☐	☐	☐	☐	☐	☐
Severe irreversible effects (possible) (R39, R68), Health damage after prolonged exposure (R48)	☐	☐	☐	☐	☐	☐

Additional remarks for certain products:

Other risks associated with the experiment

☐ Burning, freezing (☒ high or low temperatures, ☐ cryogenic materials, …)
☐ Implosion, explosion (☐ high pressure, ☐ low pressure, ☐ underpressure, …)
☐ Fire (☒ ovens, ☐ heating spirals, ☐ bunsen burner, ☐ oil baths, …)
☐ Non-ionizing radiation (☐ NMR, ☐ lasers, ☐ UV-lamps, ...)
☐ Elektrocution (☐ unproteced outlets, ☐ humid environment, ☐ high voltage, ...)
☒ Unattended operation (☐ remote room, ☒ outside working hours, ...)
☐ Risk of falling (☐ set-ups at height, ☐ at height, ☐ hard to reach places, ...)
☐ Biosafety risk (☐ pathogenic µ-organisms, ☐ GGO, ☐ cells, ☐ blood, ☐ laboratory animals, ...)
☒ Ionizing radiation (X-rays, isotopes, ...)
☐ In case of a serious incident, asking for help may NOT be possible (ex. use of toxic gasses or vapours, risk of explosion, presence of inert gases in the lab, …)
☐ Other:

Precautionary measures

Number of subexperiment*	1	2	3	4	5
Collective protective equipment					
- Closed system	☐	☐	☐	☒	☐
- Fume cabinet	☒	☒	☒	☐	☐
- Local ventilation	☒	☒	☒	☐	☐
- General ventilation	☒	☒	☒	☐	☐
- Safety screen	☐	☐	☐	☐	☐
- Waste containers	☒	☒	☒	☒	☐
- Other:	☐	☐	☐	☐	☐
Personal protective equipment					
- Laboratory coat	☒	☒	☒	☐	☐
- Safety glasses	safety spectacles (artno. 18042)	safety spectacles (artno. 18042)	safety spectacles (artno. 18042)	safety spectacles (artno. 18042)	choose an item.
- Gloves:	Disposable safety gloves nitrile EN 374 (artno. 58951)	Disposable safety gloves nitrile EN 374 (artno. 58951)	Disposable safety gloves nitrile EN 374 (artno. 58951)	Disposable safety gloves nitrile EN 374 (artno. 58951)	Kies een item.
- Masks:	Kies een item.	Kies een item.	Kies een item.	Kies een item.	Kies een item.
- Disposable cleanroom cap	☐	☐	☐	☐	☐
- Other	☐	☐	☐	☐	☐

Specific precautionary measures

☒ checking the functioning of the fume cabinet
☒ checking glassware for cracks
☐ attaching clamp rings to cooling hoses
☐ automatic switch off of heating when cooling fails
☐ overpressure protection
☐ presence of a fire extinguisher for metal fires (Class Dextinguisher)
☐ presence of an oxygen pack (required when handling cyanides)
☐ detector alarm when handling toxic or combustible gasses
☐ presence of a gas mask with specific filters (intervention)
☐ presence of a calcium gluconate ointment (handling hydrogen acid)
☐ presence of an intervention kit
☐ specific neutralization product, i.e.
☐ completing and submitting the continuous tests form (see https://admin.kuleuven.be/vgm/intranet/EN/Documents/unattendedexp.doc

☐ necessity of the presence of a second person in the neighborhood
☒ automatic alarm system (e.g. specific personal alarm)
Other:

Work practices

☒ Applying the Code of Good Laboratory Practice
https://admin.kuleuven.be/vgm/intranet/ChemischeVeiligheidCodeGoedeLabopraktijken.html)
☒ Internal training and guidance
☒ Selective waste collection – chemical waste

Special precautionary measures in case of failure

Describe the actions needed in case of emergency (e.g. malfunctioning of electricity, ventilation, water supply, gas supply, compressed air, ...)

* Number of the subexperiment as indicated under "Location of the experiment"

The experiment may not start, if all the precautionary measures can't be applied!
Personal protective equipment can be obtained via this request form:
https://admin.kuleuven.be/vgm/intranet/EN/Documents/requestformindividualprotectiveequipment.doc

Chemical waste

Indicate the waste category of each waste fraction.

Waste fraction	Waste category	Available container
If pure substances:		
Tetraethylsilicate	☐1 - ☐2 - ☒ 3 - ☐ 4 - ☐5 - ☐ 6 - ☐ Other	☒
Potassium hydroxide	☐1 - ☒2 - ☐ 3 - ☐ 4 - ☐5 - ☐ 6 - ☐ Other	☒
Sodium hydroxide	☐1 - ☒2 - ☐ 3 - ☐ 4 - ☐5 - ☐ 6 - ☐ Other	☒
Aluminumisopropoxide	☐1 - ☐2 - ☒ 3 - ☐ 4 - ☐5 - ☐ 6 - ☐ Other	☒
Perchloric acid	☒1 - ☐2 - ☐ 3 - ☐ 4 - ☐5 - ☐ 6 - ☐ Other	☒
	☐1 - ☐2 - ☐ 3 - ☐ 4 - ☐5 - ☐ 6 - ☐ Other	☐
If mixtures:		
Main component :percholric acid with water	☒1 - ☐2 - ☐ 3 - ☐ 4 - ☐5 - ☐ 6 - ☐ Other	☒
Main component :sodium hydroxide with water	☐1 - ☒2 - ☐ 3 - ☐ 4 - ☐5 - ☐ 6 - ☐ Other	☒
Main component :potassium hydroxide with water	☐1 - ☒2 - ☐ 3 - ☐ 4 - ☐5 - ☐ 6 - ☐ Other	☒
Main component :ethanol with water	☐1 - ☐2 - ☒ 3 - ☐ 4 - ☐5 - ☐ 6 - ☐ Other	☒
Main component :propanol with water	☐1 - ☐2 - ☒ 3 - ☐ 4 - ☐5 - ☐ 6 - ☐ Other	☒
Main component : tetraethylsilicate/aluminumisopropoxide with potassium hydroxide and water	☐1 - ☐2 - ☒ 3 - ☐ 4 - ☐5 - ☐ 6 - ☐ Other	☐
Other:		
	☐1 - ☐2 - ☐ 3 - ☐ 4 - ☐5 - ☐ 6 - ☐ Other	☐
	☐1 - ☐2 - ☐ 3 - ☐ 4 - ☐5 - ☐ 6 - ☐ Other	☐

Comments / questions:

Deliver this form to your general HSE Coordinator and Head.
The general HSE Coordinator sends this notification to the HSE-Department if products of Class E4 with clearance are involved.

Advice HSE services

Summary in layman's terms

Zeolites are indispensable in present-day life. Petrol refining, catalysts and detergents are merely some examples of application areas where these crystalline solids are abundantly used. This versatility can be attributed to their diverse composition and unique molecular-scale structure, consisting of channels of varying size and geometry which connect to form a 3D network. To date, 229 different zeolite frameworks have been synthesized. Despite their extensive use however, little is known about the actual growth of these materials. In this work, the growth mechanism for several zeolite structures was investigated with **atomic force microscopy (AFM)**. This special microscopy technique uses a sharp tip, which is mounted at the free end of a cantilever, to scan the surface of the material under observation. In 'contact-mode' AFM, the tip is brought into contact with the sample and then raster scanned across the surface. Because of the topography of the surface, the tip is constantly moving. This movement can be translated into a high-resolution image showing the different structures on the crystal surface. Identification of these features and determination of their height allows to formulate a hypothesis about the dominating crystal growth mechanism. For a MER-type zeolite for instance, AFM images revealed a surface covered with spiral patterns, indicating growth took place via a 'spiral growth' mechanism. Insight in the mechanisms of zeolite formation and the synthesis conditions which govern their occurrence, will enable the tailor-made preparation of zeolites with specific characteristics, expanding their applicability even further and propelling industries to the next level. Another set of experiments carried out in this work, was aimed at increasing the available surface area of zeolite particles by subjecting them to a mechanical treatment. This effect can for instance be achieved by breaking them and reducing the average particle size with respect to an untreated sample. An increased surface area is important when zeolites are used as catalysts, as the accessibility of the catalytically active sites which are located within the material, is facilitated. The mechanical treatments employed in this work were ball milling and manual treatment with a pestle. Both procedures succeeded in decreasing the dimensions of zeolite particles, without significantly damaging their crystal structure.